MULTICHANNEL AND PHASE BASED MAGNETIC RESONANCE ELECTRICAL PROPERTIES TOMOGRAPHY

A DISSERTATION SUBMITTED TO
THE GRADUATE SCHOOL OF ENGINEERING AND SCIENCE
OF BILKENT UNIVERSITY
IN PARTIAL FULFILLMENT OF THE REQUIREMENTS FOR
THE DEGREE OF
DOCTOR OF PHILOSOPHY
IN
ELECTRICAL AND ELECTRONICS ENGINEERING

By
Necip Gürler
September 2016

MULTICHANNEL AND PHASE BASED MAGNETIC RESONANCE ELECTRICAL PROPERTIES TOMOGRAPHY

By Necip Gürler

September 2016

We certify that we have read this dissertation and that in our opinion it is fully adequate, in scope and in quality, as a dissertation for the degree of Doctor of Philosophy.

Yusuf Ziya İder(Advisor)

Hayrettin Köymen

Ergin Atalar

Nevzat Güneri Gençer

Özlem Birgül

Approved for the Graduate School of Engineering and Science:

Ezhan Karaşan
Director of the Graduate School

ABSTRACT

MULTICHANNEL AND PHASE BASED MAGNETIC RESONANCE ELECTRICAL PROPERTIES TOMOGRAPHY

Necip Gürler
Ph.D. in Electrical and Electronics Engineering
Advisor: Yusuf Ziya İder
September 2016

Imaging of electrical properties (EPs, i.e. conductivity and dielectric permittivity) of tissues give valuable information about the physiological and pathological conditions of tissues. Among the EP imaging modalities, magnetic resonance electrical properties tomography (MREPT) has the potential that it can be used both in clinical diagnosis and local specific absorption rate (SAR) calculation. However, there are several issues in the conventional MREPT methods such as boundary artifact, low convective field (LCF) artifact, transceive phase assumption (TPA), usability of only birdcage coil, which precludes the clinical applicability of these methods. This dissertation aims that MREPT can be used in the clinical applications in a fast and reliable way by solving these issues in the conventional MREPT methods. For this purpose two novel methods have been proposed. One is the receive sensitivity (B_1^-) based multichannel cr-MREPT method in which the multi-channel receive coil configuration has been employed to solve the LCF artifact issue in the conventional cr-MREPT method. In addition to this contribution, the method removes the limitation of using birdcage coil in the conventional MREPT methods by enabling the use of standard MRI coils. Since the governing equation is based on the receive sensitivities, a new approach based on two consecutive experiments has been proposed to map the complex B_1^- of each channel. It has been shown in both simulations and experiments that the LCF region differs from one channel to another and artifact-free EP reconstruction is possible by combining the appropriate channels in a logical manner. The drawback of this method is that it is using transceive phase assumption. The second method, in which this drawback and also the issues in the conventional MREPT methods aforementioned above have been solved, is the generalized phase based electrical conductivity imaging method. Starting from the Maxwell's equations and also including EP gradient terms in the formulation, a new equation for the phase-based EPT method has been developed. The governing partial differential

equation (PDE) is in the form of convection-reaction equation the coefficients of which are the derivatives of the measured MR transceive phase. Since only MR phase is used, the method is considerably fast (no B_1 mapping is required), and it is applicable for any coil configuration (no TPA is used). The superiority of the proposed method over the conventional phase based EPT method has been shown both in the simple phantom simulations and experiments and in the noisy human brain simulation and healthy volunteer experiments. Furthermore, initial clinical trials with two patients with neurovascular diseases in the subacute phase have been conducted. Each examination took about six minutes. It has been observed that the conductivity increases in the ischemic region when compared to other regions, whereas no conductivity change has been observed in the hematoma region. To standardize the method for the specific clinical applications such as differentiation of the ischemic stroke from the hemorrhagic stroke in the acute phase, further case studies need to be conducted in a systematic way.

Keywords: magnetic resonance electrical properties tomography (MREPT), convection reaction equation based MREPT (cr-MREPT), phase based EPT, electrical property imaging, conductivity imaging, multichannel electrical property imaging.

ÖZET

ÇOK KANALLI VE FAZ TEMELLİ MANYETİK REZONANS ELETRİKSEL ÖZELLİK TOMOGRAFİSİ

Necip Gürler
Elektrik ve Elektronik Mühendisliği, Doktora
Tez Danışmanı: Yusuf Ziya İder
Eylül 2016

Dokuların elektriksel özelliklerinin (EÖ, yani iletkenliğinin ve dielektrik geçirgenliğinin) görüntülenmesi dokuların fizyolojik ve patolojik durumu hakkında değerli bilgiler verir. EÖ görüntüleme yöntemleri arasından, manyetik rezonans elektriksel özellik tomografisinin (MREÖT) hem klinik tanıda hem de lokal özgül soğurma oranının (ÖSO) hesaplanmasında bir potansiyeli vardır. Fakat, klasik MREÖT yöntemlerinin, sınır artefaktı, düşük konvektif bölgesi (DKB) aretefaktı, toplam faz varsayımı (TFV), sadece kuş-kafesi sarımının kullanılabilirliği gibi bu yöntemlerin klinikte uygulanabilirliğini olanaksızlaştıran bazı sorunları bulunmaktadır. Bu tez klasik MREÖT yöntemlerindeki bu sorunları çözerek MREÖT tekniğinin hızlı ve güvenilir bir şekilde klinikte uygulanmasını hedeflemektedir. Bu amaçla, iki yeni yöntem önerilmiştir. İlki, klasik kr-MREÖT yöntemindeki DKB artefaktı sorununu çözmek için içerisinde çok kanallı almaç sarımlarının kullanıldığı almaç hassasiyetine (B_1^-) dayalı çok kanallı kr-MREÖT yöntemidir. Bu katkıya ek olarak bu yöntem standart MRG sarımlarının kullanılmasına olanak sağlayarak klasik MREÖT yöntemlerindeki kuşkafesi sarımı kullanılmasının kısıtını kaldırmaktadır. Yöntemin ana denklemi almaç hassasiyetine dayalı olduğundan her kanalın kompleks B_1^- bilgilisini haritalamak için arka arkaya uygulan iki deneye dayalı yeni bir yaklaşım önerilmiştir. Hem benzetim hem de deneysel çalışmalarda DKB bölgesinin bir kanaldan diğer kanala değiştiği ve uygun kanalların mantıklı bir şekilde birleştirilerek artefaktan arınmış EÖ geriçatımlarının mümkün olduğu gösterilmiştir. Bu yöntemin dezavantajı toplam faz varsayımını kullanıyor olmasıdır. Bu dezavantajın ve yukarıda bahsedilen klasik MREÖT yöntemlerindeki sorunların da çözüldüğü ikinci önerilen yöntem faza dayalı genelleştirilmiş elektriksel iletkenlik görüntüleme metodudur. Maxwell'in denklemlerinden başlayarak ve EÖ gradyanlarını da formulasyona dahil ederek klasik faza dayalı EÖT yöntemi için yeni bir denklem geliştirilmiştir. Bu ana kısmi diferansiyel denklemi, katsayılarının ölçülen

MR fazının türevlerinden oluştuğu, konveksiyon reaksiyon denklemi formundadır. Sadece MR fazı kullanıldığından yöntem oldukça hızlıdır (herhangi bir B_1 haritalamaya ihtiyaç duymaz) ve herhangi bir sarım yapısı için uygulanabilir (toplam faz varsayımını kullanmaz). Önerilen yöntemin klasik faza dayalı EÖT yönteminden üstünlüğü hem basit fantom simülasyonu ve deneyleri ile hem de gürültü eklenmiş insan beyni simulasyonları ve sağlıklı insan deneyleri ile gösterilmiştir. Buna ek olarak, akutkronik arası fazda nörovasküler hastası iki hasta ile ilk klinik denemeler gerçekleştirilmiştir. Her bir çekim ortalama altı dakika sürmüştür. İskemik bölgede diğer bölgelere göre iletkenliğin arttığı gözlemlenmiş ve hematom bölgesinde ise iletkenlikte herhangi bir değişiklik gözlenmemiştir. Yöntemin, iskemik inmenin hemorajik inmeden akut fazda ayrılması gibi bu tip spesifik klinik uygulamalarda standartlaşabilmesi için, daha fazla vaka çalışmasının sistematik bir şekilde yürütülmesi gerekmektedir.

Anahtar sözcükler: manyetik rezonans elektriksel özellik tomografisi (MREÖT), konveksiyon reaksiyon denklemine dayalı MREÖT (kr-MREÖT), faza dayalı EÖT, elektriksel özellik görüntüleme, iletkenlik görüntüleme, çok kanallı elektriksel özellik görüntüleme.

Acknowledgement

First and foremost, I would like to express my deep and sincere gratitude to my advisor, Prof. Yusuf Ziya İder, for his invaluable guidance, his endless determination, and his patience. It has been six years, and he has been always supportive to me since the first day I began working on my MSc study. I remember the day I had an interview with him for the MSc application, now I am a PhD candidate. I always admire his wide knowledge and his logical way of thinking which have been of great value for me. Beyond his role as an academic advisor, he has been a very good friend. It has been a great pleasure to work with him for the past six years.

I would like to thank my jury members, Prof. Hayrettin Köymen and Prof. Nevzat Güneri Gençer, for their valuable comments which increased the scientific quality of my dissertation. I would also like to thank Prof. Ergin Atalar and Asst. Prof. Özlem Birgül for accepting to be a member of my jury, reading and commenting on this dissertation.

I would like to thank Assoc. Prof. Hava Dönmez Keklikoğlu for her valuable help during the case study experiments.

I wish to thank Volkan Açıkel, Taner Demir, Cemre Arıyürek, Koray Ertan and Erhan Erköseoğlu for their help during the experiments in National Magnetic Resonance Research Center (UMRAM).

I want to acknowledge The Scientific and Technological Research Council of Turkey (TÜBİTAK) for providing financial support during my PhD studies.

I want to thank Mürüvet Parlakay for her help on the administrative works.

I also want to thank Ergün Hırlakoğlu, Onur Bostancı, and Ufuk Tufan for their friendship and for their technical support in the laboratories.

Very special thanks goes to my office mate Ömer Faruk Oran for being a very good friend to me, for sleepless nights at EE213 and UMRAM, and for all the fun we have had in the last six years. I would like to extend my thanks to new members of EMTP and BCI Group: Gökhan, Gülşah, Toygun and Yiğit.

Last but not least, I wish to express my deepest to my parents who have grown me up and supported me throughout my life. Also, I would like to thank my sister, Gizem, for her lovely support. Of course, I am indebted to my dear wife Ayça Atasoy Gürler for her unconditional love, invaluable support, motivation and understanding.

Contents

1 INTRODUCTION **1**

1.1 Electrical Properties (EPs) 2

1.2 Electrical Property Imaging 3

1.3 Purpose and Scope of the Dissertation 6

1.4 Organization of the Dissertation 8

2 THEORETICAL BACKGROUND: A LITERATURE SURVEY **10**

2.1 Magnetic Resonance Electrical Properties Tomography (MREPT) 11

2.1.1 Formulation of MREPT 11

2.1.2 Limitations 12

2.2 Magnitude and Phase based EPT 15

2.3 Convection-Reaction Equation based MREPT (cr-MREPT) . . . 17

2.4 Proposed Methods 20

3 B_1^- BASED MULTICHANNEL cr-MREPT **22**

3.1 Theory 23

3.1.1 Derivation of the Central Equation 23

3.1.2 Finding the Complex B_1^- 25

3.2 Methods 26

3.2.1 Solution of the Central Equation 26

3.2.2 Simulation Methods 28

3.2.3 Experimental Methods 29

3.3 Results 30

3.3.1 Simulation Results 30

3.3.2 Experimental Results 32

3.4 Discussion 38

4 GENERALIZED PHASE BASED ELECTRICAL CONDUCTIVITY IMAGING 41

4.1 Theory 42
4.2 Methods 45
4.2.1 Solution of the Central Equation 45
4.2.2 Simulation Methods 47
4.2.3 Experimental Methods 49
4.3 Results 52
4.3.1 Simulation Results 52
4.3.2 Experimental Results 55
4.4 Theoretical Investigation of the Proposed Method 60
4.4.1 Assumptions 60
4.4.2 Boundary Condition and Diffusion Term 86
4.5 Clinical Applicability of the Proposed Method 90
4.6 E_z based SAR Estimation Procedure 94
4.7 Discussion 95

5 CONCLUSION 98

A Derivation of the Central Equation 112

List of Figures

2.1 Illustration of the boundary artifact issue. Results were obtained using the simulation phantom, which will be explained in the fourth chapter. (a) Actual conductivity (in S/m) (b) Reconstructed conductivity (in S/m) using conventional MREPT. 13

2.2 Illustration of the boundary artifact issue. Results were obtained using the brain model simulations, which will be explained in the fourth chapter. (a) Actual conductivity (in S/m) (b) Reconstructed conductivity (in S/m) using conventional MREPT. . . . 13

2.3 Illustration of the boundary artifact and LCF artifact issue. Results were obtained from the phantom experiment, which will be explained in the third chapter. (a) Reconstructed conductivity (in S/m) using conventional MREPT. (b) Magnitude of the convective field (inA/m^2) (c) Reconstructed conductivity (in S/m) using cr-MREPT. 19

3.1 (a) Simulation phantom and the surface coil model. (b) Actual conductivity at the central transverse slice (in S/m). 28

3.2 (a) B_1^- magnitude distributions (T) (b) B_1^- phase distributions (rad) of each channel. 29

3.3 (a) Magnitude of the convective fields (A/m^2) (b) Corresponding conductivity maps (S/m) of each channel 31

3.4 Reconstructed conductivity map using the combination of all four channel (S/m) 32

3.5 Results of the conventional cr-MREPT and MREPT methods. (a) The magnitude of the convective field (in A/m^2) (b) Reconstructed conductivity (in S/m) using B_1^+ based cr-MREPT. (c) Reconstructed conductivity (in S/m) using conventional MREPT. 33
3.6 Magnitude of the convective field of each channel 34
3.7 Reconstructed conductivity map of each channel (no combination) 35
3.8 Reconstructed conductivity map using the combination of 5th and 11th channel (S/m) 36
3.9 Results for the healthy volunteer study. (a) Selection of local regions, where the conductivity distributions are calculated, on the SSFP magnitude image (b-d) Corresponding reconstructed conductivity images using the proposed method (S/m) 37

4.1 Birdcage coil simulation models: (a) loaded with the simple phantom (b) loaded with the head model. Experimental phantom models: (c) with one anomaly (left), and with multiple anomalies (right). 47
4.2 (a) Birdcage coil model loaded with the human brain model (b) Conductivity distribution at a central slice of each orientation (S/m) (c) Relative dielectric permittivity distribution at a central slice of each orientation. 48
4.3 (a) Selection of the ROI indicated by the blue polygon (left), the actual conductivity map in the ROI (middle), illustration of the line where the conductivity profiles are plotted (right) (b) Reconstructed conductivity maps using the conventional phase based EPT method and the proposed method for different SNR values. (c) Conductivity profiles of the conventional method and the proposed method (along the dotted line given in (a)) for different diffusion coefficients under different SNR values. 53

4.4 Human head model simulations. (a) Selection of the ROI indicated by the blue polygon (left), the actual conductivity map in the ROI (right) (b) Reconstructed conductivity maps using the conventional phase based EPT method and the proposed method for different SNR values (c) Conductivity profiles of the conventional method and the proposed method along the lines which are shown above each profile plot (when the SNR=∞). 54

4.5 Magnitude, phase, and reconstructed conductivity images of the first experimental phantom for one of the channels in the ROI. (a) SSFP Magnitude image (b) SSFP Transceive phase (c) Conductivity map reconstructed using the conventional method (d) Conductivity map reconstructed using the proposed method. . . 56

4.6 Magnitude, phase, and reconstructed conductivity images of the second experimental phantom for one of the channels. (a) Selection of the ROI indicated by the blue polygon (b) SSFP Magnitude image (c) SSFP Transceive phase (d) Conductivity map using the conventional method (e) Conductivity map using the proposed method (c=0.01) (f) Conductivity map using the proposed method (c=0.05) (g) Conductivity profiles of the conventional and the proposed method given in (d)-(f). 58

4.7 Magnitude, phase, and reconstructed conductivity images of human brain for one of the channels at the ROI. (a) Selection of the ROI indicated by the blue polygon (b) SSFP Magnitude image (c) SSFP Transceive phase (d) Conductivity map reconstructed using the conventional method (e) Conductivity map reconstructed using the 3D formulation of the proposed method. 59

4.8 (a) Simulation model used for investigating the assumptions. (b) Wire-frame illustration of the model. (c) Actual conductivity distribution in S/m at the central axial slice, which is shown with red in (b). 61

4.9 Results of the valid model. (a) $\frac{\sigma^2}{(\omega\epsilon)^2}$, (b) $|\nabla B_1^+|$, (c) $|\nabla B_1^-|$, (d-f) imaginary part of each spatial component (x-, y-, and z-) of the B_z terms are divided by the imaginary part of the corresponding component in the phase terms. (g) Actual conductivity (in S/m) (h) Reconstructed conductivity distribution (in S/m) using conventional method (i) Reconstructed conductivity distribution (in S/m) using proposed method at the central axial slice. 62

4.10 Results of the first scenario ($3T$ case). (a) $\frac{\sigma^2}{(\omega\epsilon)^2}$, (b) $|\nabla B_1^+|$, (c) $|\nabla B_1^-|$, (d-f) imaginary part of each spatial component (x-, y-, and z-) of the B_z terms are divided by the imaginary part of the corresponding component in the phase terms. (g) Actual conductivity (in S/m) (h) Reconstructed conductivity distribution (in S/m) using conventional method (i) Reconstructed conductivity distribution (in S/m) using proposed method at the central axial slice. 64

4.11 Results of the first scenario ($7T$ case). (a) $\frac{\sigma^2}{(\omega\epsilon)^2}$, (b) $|\nabla B_1^+|$, (c) $|\nabla B_1^-|$, (d-f) imaginary part of each spatial component (x-, y-, and z-) of the B_z terms are divided by the imaginary part of the corresponding component in the phase terms. (g) Actual conductivity (in S/m) (h) Reconstructed conductivity distribution (in S/m) using conventional method (i) Reconstructed conductivity distribution (in S/m) using proposed method at the central axial slice. 65

4.12 Profile plots for the valid model and scenario 1. (a) Illustration of the line where the conductivity profiles are plotted. (b) Conductivity profiles (in S/m) for the proposed method. (c) Conductivity profiles (in S/m) for the conventional method. 66

4.13 Results of the second scenario ($1.5T$ case when $\epsilon_r = 40$).(a) $\frac{\sigma^2}{(\omega\epsilon)^2}$, (b) $|\nabla B_1^+|$, (c) $|\nabla B_1^-|$, (d-f) imaginary part of each spatial component (x-, y-, and z-) of the B_z terms are divided by the imaginary part of the corresponding component in the phase terms. (g) Actual conductivity (in S/m) (h) Reconstructed conductivity distribution (in S/m) using conventional method (i) Reconstructed conductivity distribution (in S/m) using proposed method at the central axial slice. 68

4.14 Results of the second scenario ($3T$ case when $\epsilon_r = 40$). (a) $\frac{\sigma^2}{(\omega\epsilon)^2}$, (b) $|\nabla B_1^+|$, (c) $|\nabla B_1^-|$, (d-f) imaginary part of each spatial component (x-, y-, and z-) of the B_z terms are divided by the imaginary part of the corresponding component in the phase terms. (g) Actual conductivity (in S/m) (h) Reconstructed conductivity distribution (in S/m) using conventional method (i) Reconstructed conductivity distribution (in S/m) using proposed method at the central axial slice. 69

4.15 Results of the second scenario ($7T$ case when $\epsilon_r = 40$). (a) $\frac{\sigma^2}{(\omega\epsilon)^2}$, (b) $|\nabla B_1^+|$, (c) $|\nabla B_1^-|$, (d-f) imaginary part of each spatial component (x-, y-, and z-) of the B_z terms are divided by the imaginary part of the corresponding component in the phase terms. (g) Actual conductivity (in S/m) (h) Reconstructed conductivity distribution (in S/m) using conventional method (i) Reconstructed conductivity distribution (in S/m) using proposed method at the central axial slice. 70

4.16 Results of the second scenario ($1.5T$ case when $\epsilon_r = 80$).(a) $\frac{\sigma^2}{(\omega\epsilon)^2}$, (b) $|\nabla B_1^+|$, (c) $|\nabla B_1^-|$, (d-f) imaginary part of each spatial component (x-, y-, and z-) of the B_z terms are divided by the imaginary part of the corresponding component in the phase terms. (g) Actual conductivity (in S/m) (h) Reconstructed conductivity distribution (in S/m) using conventional method (i) Reconstructed conductivity distribution (in S/m) using proposed method at the central axial slice. 72

4.17 Results of the second scenario ($3T$ case when $\epsilon_r = 80$). (a) $\frac{\sigma^2}{(\omega\epsilon)^2}$, (b) $|\nabla B_1^+|$, (c) $|\nabla B_1^-|$, (d-f) imaginary part of each spatial component (x-, y-, and z-) of the B_z terms are divided by the imaginary part of the corresponding component in the phase terms. (g) Actual conductivity (in S/m) (h) Reconstructed conductivity distribution (in S/m) using conventional method (i) Reconstructed conductivity distribution (in S/m) using proposed method at the central axial slice. 73

4.18 Profile plots for scenario 2. (a),(d) Illustration of the line where the conductivity profiles are plotted. (b),(e) Conductivity profiles (in S/m) for the proposed method. (c),(f) Conductivity profiles (in S/m) for the conventional method. 74

4.19 (a) Simulation phantom and the surface coil model used for the third scenario. (b) Conductivity distribution (in S/m) at the slice shown with red. (c) Distribution of $|B_1^+|$. (d) Distribution of $|B_1^-|$. 76

4.20 Results of the third scenario (when the birdcage coil is used). (a) $\frac{\sigma^2}{(\omega\epsilon)^2}$, (b) $|\nabla B_1^+|$, (c) $|\nabla B_1^-|$, (d-f) imaginary part of each spatial component (x-, y-, and z-) of the B_z terms are divided by the imaginary part of the corresponding component in the phase terms. (g) Actual conductivity (in S/m) (h) Reconstructed conductivity distribution (in S/m) using conventional method (i) Reconstructed conductivity distribution (in S/m) using proposed method at the central axial slice. 77

4.21 Results of the third scenario (when the surface coil is used). (a) $\frac{\sigma^2}{(\omega\epsilon)^2}$, (b) $|\nabla B_1^+|$, (c) $|\nabla B_1^-|$, (d-f) imaginary part of each spatial component (x-, y-, and z-) of the B_z terms are divided by the imaginary part of the corresponding component in the phase terms. (g) Actual conductivity (in S/m) (h) Reconstructed conductivity distribution (in S/m) using conventional method (i) Reconstructed conductivity distribution (in S/m) using proposed method at the central axial slice. 78

4.22 (a) x- component of the convection term ($\frac{\partial \phi^{tr}}{(} inrad/m)\partial x$) (b) y-component of the convection term ($\frac{\partial \phi^{tr}}{\partial y}$) (in rad/m) (c) z- component of the convection term ($\frac{\partial \phi^{tr}}{\partial z}$) (in rad/m). 79

4.23 (a) $|B_1^+|$ and (b) $|B_1^-|$ distributions for the rotated surface coil. The coil itself is also shown in the plots. 80

4.24 Results of the third scenario (when the surface coil is rotated). (a) $\frac{\sigma^2}{(\omega\epsilon)^2}$, (b) $|\nabla B_1^+|$, (c) $|\nabla B_1^-|$, (d-f) imaginary part of each spatial component (x-, y-, and z-) of the B_z terms are divided by the imaginary part of the corresponding component in the phase terms. (g) Actual conductivity (in S/m) (h) Reconstructed conductivity distribution (in S/m) using conventional method (i) Reconstructed conductivity distribution (in S/m) using proposed method at the central axial slice. 81

4.25 Convective fields for the rotated surface coil case. (a) x- component of the convection term ($\frac{\partial \phi^{tr}}{\partial x}$) (in rad/m) (b) y- component of the convection term ($\frac{\partial \phi^{tr}}{\partial y}$) (in rad/m) (c) z- component of the convection term ($\frac{\partial \phi^{tr}}{\partial z}$) (in rad/m). 82

4.26 Results of the fourth scenario ($1.5T$ case). (a) $\frac{\sigma^2}{(\omega\epsilon)^2}$, (b) $|\nabla B_1^+|$, (c) $|\nabla B_1^-|$, (d-f) imaginary part of each spatial component (x-, y-, and z-) of the B_z terms are divided by the imaginary part of the corresponding component in the phase terms. (g) Actual conductivity (in S/m) (h) Reconstructed conductivity distribution (in S/m) using conventional method (i) Reconstructed conductivity distribution (in S/m) using proposed method at the central axial slice. 83

4.27 Results of the fourth scenario ($3T$ case). (a) $\frac{\sigma^2}{(\omega\epsilon)^2}$, (b) $|\nabla B_1^+|$, (c) $|\nabla B_1^-|$, (d-f) imaginary part of each spatial component (x-, y-, and z-) of the B_z terms are divided by the imaginary part of the corresponding component in the phase terms. (g) Actual conductivity (in S/m) (h) Reconstructed conductivity distribution (in S/m) using conventional method (i) Reconstructed conductivity distribution (in S/m) using proposed method at the central axial slice. 84

4.28 Results of the fourth scenario ($7T$ case). (a) $\frac{\sigma^2}{(\omega\epsilon)^2}$, (b) $|\nabla B_1^+|$, (c) $|\nabla B_1^-|$, (d-f) imaginary part of each spatial component (x-, y-, and z-) of the B_z terms are divided by the imaginary part of the corresponding component in the phase terms. (g) Actual conductivity (in S/m) (h) Reconstructed conductivity distribution (in S/m) using conventional method (i) Reconstructed conductivity distribution (in S/m) using proposed method at the central axial slice. 85

4.29 Illustration of the oscillatory decay from the given boundary (initial) value to the final value under different diffusion coefficients (c is used for diffusion coefficient) and boundary conditions (BC is for the value of the conductivity assigned at the boundary). . . . 87

4.30 Reconstructed conductivity maps of simulated human brain for different diffusion coefficients. (a) 2D and 3D surface plots of the actual conductivity of an axial slice (b) 2D and 3D surface plots of reconstructed conductivity of the same slice for c=0 (c) Same as in (b) for c=0.05 (d) Magnitude of the x-component of the gradient of the transceive phase (e) Magnitude of the y-component of the gradient of the transceive phase (f) Magnitude of the Laplacian of the transceive phase 89

4.31 Images for the patient with hematoma. (a) CT image (b) T2W/FLAIR image (hematoma and surrounding edema are encircled) (c) Corresponding SSFP magnitude image (d) Corresponding conductivity image (hematoma and surrounding edema are encircled) 91

4.32 Images for the patient with ischemia in the left cerebellum. (a) Selected oblique slice (shown with red line) for parts b-c. (b) DWI image (infarction region is encircled) (c) ADC image (d) corresponding SSFP magnitude image (e) corresponding conductivity image (infarction region is encircled) 92

4.33 Images for the patient with ischemia in the occipital lobe (a) Selected oblique slice (shown with red line) for parts b-c. (b) DWI image (infarction region is encircled) (c) ADC image (d) corresponding SSFP magnitude image (e) corresponding conductivity image (infarction region is encircled) 93

List of Tables

4.1 EPs of the tissues of human brain model 48
4.2 Balanced SSFP Sequence parameters for all experiments 50
4.3 Total relative error of the conventional and the proposed method . 55

Chapter 1

INTRODUCTION

Magnetic Resonance Imaging (MRI) is one of the mostly used diagnostic techniques in medicine. It is a powerful imaging modality that does not use x-ray or any other damaging radiation, and it is well suited to image soft tissues in the human body in a noninvasive way. In order for MRI to be used as diagnostic purposes, there must be a contrast difference between MR signal of the malignant tissue and the healthy tissue. MRI has the flexibility that the signal received from the tissue can be manipulated in many ways (by adjusting imaging and tissue parameters), leading to numerous contrast mechanisms. The most basic ones are the spin density weighted, and relaxation based (T_1, T_2 or T_2^*) contrasts. There are also other clinically established contrast mechanisms, such as flow, diffusion, magnetization transfer, contrast enhancing agents, and magnetic susceptibility [1]. Each contrast mechanism exhibits different tissue related property, and results in a different contrast in the MR image. For example, magnetic susceptibility weighted imaging offers to visualize venous structure and iron in the brain, and therefore it gives important diagnostic information in neurovascular and neurodegenerative diseases. In this dissertation, different from the aforementioned contrast mechanisms used in MRI, a unique contrast, which is based on the electrical properties of tissues, will be investigated in every aspects including MR sequence, reconstruction, and clinical applications. In the following sections of this chapter, first, brief explanation about electrical properties and MR based

electrical property imaging will be presented. Then, purpose and scope of the dissertation will be stated with the motivations. Finally, a chapter-by-chapter organization of the dissertation will be given.

1.1 Electrical Properties (EPs)

Electrical properties (EPs), i.e. conductivity (σ) and dielectric permittivity (ϵ), of tissues have been of interest for over four decades [2–5]. The measurements of EPs have an importance when tissue interact with the electromagnetic energy, e.g. radiofrequency (RF) ablation [6], hyperthermia [7], or impedance pneumography [8]. Additionally, the knowledge of EPs also provides important contributions to biophysical and physiological sciences such as understanding the conductance and capacitance of a cell membrane [9, 10], diffusional motions of lipids and proteins in cell membranes [11], or investigating enzyme activation and molecular mobility [12].

From the MRI point of view, imaging EPs of tissues and using EP maps as a contrast have two major importances. One is that EP maps of tissues can be used for diagnostic purposes. For example, it has been shown that the EPs significantly change in the tumor region compared to healthy tissue [13–15]. Additionally, distinguishing the glioma grades from the EP maps has been studied recently [16]. Apart from brain tumor studies, there has been plenty of studies conducted on diagnostic use of EP maps in different cases, such as ischemic stroke [17], pelvic tumors [7], and breast cancer [18]. All studies have shown promising results for the use of EP maps in clinical diagnosis. The second importance of EPs in MRI is that the conductivity is the key parameter in calculating local specific absorption rate (SAR). In conventional MR scanners global SAR is calculated, which does not give any information about the local tissue heating. Especially in ultra high field MRI systems ($\geq 3T$), to employ multi-transmit RF coils, it is important to know electromagnetic field distribution as well as local SAR in the region of interest (ROI) for any driving configuration of RF coils prior to the examination [19, 20]. This procedure is generally performed by simulations in

which the same human model is used for all patients. The knowledge of EPs will provide subject-specific simulations resulting an appropriate estimation of local SAR for any multi-transmit configurations.

1.2 Electrical Property Imaging

Over the years many studies have been conducted to image EPs at different frequencies. For low-frequency applications (1 kHz to 1 MHz), for example, electrical impedance tomography (EIT) and magnetic induction tomography (MIT) have been proposed [21–26]. In EIT, sinusoidal currents are injected into tissue through conducting surface electrodes that are attached to body, and the resulting induced voltages are measured from the same (or different) surface electrodes. Similarly, in MIT, induced current is generated in the tissue using external transmitter coil, and generated magnetic field due to the induced current is measured from receiver coil. These current-voltage data sets obtained in both methods are then used to calculate impedance maps. The major disadvantage of these methods is that the spatial resolution of resulting images is very low compared to other imaging techniques. To improve spatial resolution, magnetic resonance electrical impedance tomography (MREIT) has been proposed [27–35]. Similar to EIT, current is injected into an object through surface electrodes in MREIT, but the difference is that magnetic field generated inside the object is measured using MRI not using boundary electrodes, which provides high spatial resolution especially in internal regions. From the clinical perspective, the major limitation of this method is the amount of injection current that may stimulate the muscle and nerve during the examination.

Different from the methods mentioned above, a method called magnetic resonance electrical properties tomography (MREPT) has been recently proposed to image EPs at Larmor frequency of an MRI system [36]. The concept of MREPT was first introduced by Haacke et al [37], and it was practically applied using high field MRI scanner by Wen et al [38]. In this method, the current is applied to an object using the transmitter RF coil and the generated RF magnetic field

in the object is measured using any B_1 mapping techniques [39–42]. From the measured magnetic field, EPs are calculated. This method has advantages over the MREIT that no electrode is attached to body, and it uses the facilities of standard MR system, therefore no other hardware is required.

The relation between the magnetic flux density, $\mathbf{B} = (B_x, B_y, B_z)$, and the complex permittivity, $\gamma = \sigma + i\omega\epsilon$, can be expressed by Helmholtz equation (using the $e^{i\omega t}$ convention) as

$$-\nabla^2\mathbf{B} = \frac{\nabla\gamma}{\gamma} \times (\nabla \times \mathbf{B}) - i\omega\mu\gamma\mathbf{B} \tag{1.1}$$

where $\mathbf{B}$ and γ are function of space, $\mathbf{r} = (x, y, z)$, ω is the Larmor frequency, and μ is the magnetic permeability.

If EPs are assumed to be constant in tissue compartments that is $\nabla\gamma = 0$, the gradient term, $\frac{\nabla\gamma}{\gamma} \times (\nabla \times \mathbf{B})$, in Eq. (1.1) will vanish. Writing the resulting equation in terms of transmit and receive sensitivity of the RF coil, i.e. B_1^+ and B_1^-, yields the central equation of conventional MREPT method [36] as

$$\gamma = \frac{\nabla^2 B_1^{\pm}}{i\omega\mu B_1^{\pm}} \tag{1.2}$$

There are several drawbacks of using Eq. (1.2) in calculating EPs. One such drawback is the "boundary artifact" issue. Since the gradient of EPs is assumed to be zero, the EPs of tissue transition regions cannot be reconstructed, and this results an artifact in the image. For complex structures, e.g. brain which has many tissue transition regions, this issue will be a headache because many boundary artifacts will occur near the tissue boundaries and this will lead to misinterpretation of the EP images. The second drawback is the transcieve phase assumption (TPA). To solve Eq. (1.2), both the magnitude and the phase of B_1^+ (or B_1^-) must be known. For finding the magnitude of B_1^+, any B_1 mapping technique can be used [39–42]. Finding the phase of B_1^+, however, is not straightforward since the measured (or transcieve) phase in MRI is the combination of B_1^+ (transmit) and B_1^- (receive) phases. Therefore, we cannot directly find the transmit phase. A

temporary solution to this problem is that when a quadrature coil, e.g. birdcage coil, is used for both transmit and receive operations, the transmit sensitivity can be approximated as the receive sensitivity ($B_1^+ \approx B_1^-$). From this approximation, the transmit phase can be found as half of the transcieve phase. Although this assumption seems to be fair for low field strengths, it starts to fail at higher field strengths ($\geq 3T$). Also, it limits the coil usage to specific coil type. For example, when we transmit from a birdcage coil and receive from a surface coil, this assumption does not hold, because the transmit sensitivity of the birdcage coil will not be equal to the receive sensitivity of the surface coil. Last but not least is the signal-to-noise (SNR) issue. Both B_1 mapping techniques and Laplacian operator in Eq. (1.2) enhance the noise in the MR signal. For this purpose, some filtering operations are applied to MR images to suppress the noise, which in turn reduces the spatial resolution of the EP images. Therefore, it is extremely crucial to obtain high SNR MR images to get high-quality EP contrast. To solve above drawbacks and challenges various approaches have been proposed so far:

For boundary artifact issue, Hafalir et al. proposed convection reaction equation based MREPT (cr-MREPT) method [43], in which MREPT formulation is re-derived by including the gradient terms in Eq. (1.1), and the resulting partial differential equation (PDE), which is in the form of convection reaction equation, was solved using the finite element method (FEM). Similarly, Liu et al. used the same approach for reformulation of MREPT but they utilized multi-channel transceiver RF coil to obtain multiple transmit and receive fields for solving the PDE [44]. While both approaches solve boundary artifact issue, they suffer from different problems. For example, cr-MREPT method has stabilization issue in regions where the convection term is low, and also cr-MREPT uses the transcieve phase assumption (TPA). The other method, gEPT, needs both complex B_1^+ and B_1^- sensitivities but B_1^- is always coupled with the proton density. To decouple the proton density from the receive sensitivity, they use the approach, which is based on the elliptical symmetry assumption of the object in the coil [45], which can easily be violated in practice. Another method was proposed by Balidemaj et al. to solve the boundary artifact issue [46]. It is an iterative approach, which is named as CSI-EPT (current source inversion EPT), and is based on the integral

equation of electromagnetic fields. The major limitation of this method is that it has no 3D implementation yet, and much effort is still needed for practical application.

To eliminate TPA, multi-channel transmit-receive coil configuration based studies have been proposed [45, 47–49]. In [47] (local Maxwell tomography (LMT)), a TPA free formulation was derived, and EPs were solved analytically using the transmit and receive sensitivities of each channel. However, since LMT is based on Eq. (1.2) it has boundary artifacts in the solutions. Additionally, in its formulation, constant magnetization is assumed in the whole object, which is used to decouple the receive sensitivity from the proton density in the formulations. In its generalized form [48], on the other hand, varying EPs and magnetization were taken into consideration but it still needs to be assessed in practice. In [49], a novel EPT method, which is based on the relative receive coil sensitivities was proposed. The major disadvantages of this method are the boundary artifact issue and the sensitivity to noise. The method is very sensitive to noise since the formulation includes the third derivatives. Different from these mentioned multi-channel coil approaches, more practical method, called phase-based EPT, was proposed to solve TPA issue [50–52]. In this study, phase-based conductivity and magnitude-based permittivity imaging concepts were introduced. In other words, it has been shown that the conductivity is mostly related with the phase component, and permittivity is related with magnitude component of the MR signal. Most of the patient studies conducted so far has been based on this phase-based conductivity imaging approach because it is considerably fast (no B_1^+ mapping is required) and TPA free. However, the major limitation of this method is the boundary artifact issue, which reduces reliability of this method, and precludes the clinical use.

1.3 Purpose and Scope of the Dissertation

With the motivations given in Section 1.1, we understand that EPs provide valuable information in both diagnostic and RF safety concepts, and there has been

high interest to image EPs, especially to conductivity imaging. Among the electrical property imaging methods, MREPT seems to be more prominent than other techniques, since there is no current injection in this method, and it does not require any other hardware except a standard MRI system of which it uses the high spatial resolution capability. As mentioned previously, MREPT takes advantage of inherent MRI capabilities such as generation of RF magnetic field to induce eddy currents in the tissue, and the measurement of the generated magnetic field in the ROI with a high spatial resolution, and in the meantime it may also provide subject-specific conductivity information to MRI systems, which can be used for safer examination. However, considering the drawbacks in the MREPT methods given in the previous section, there is still a need for reliable EP imaging method in the clinical applications, which has no artifact, which is practically applicable for any coil configuration (no TPA assumption) and fast to be used for clinical purpose, and which is robust against noise. Taking into consideration all of these demands, this dissertation introduces two novel methods in MR based tissue electrical property imaging.

The first method is called B_1^- based multichannel cr-MREPT [53, 54]. In this method, we are aiming to solve the low convective field (LCF) artifact issue in the cr-MREPT method [43], which was recently published by our group. As mentioned earlier, cr-MREPT method has advantages over conventional MREPT methods [51] in terms of being capable of reconstructing EPs in the transition regions, and being more robust against noise. However, the major limitation of cr-MREPT method is that EPs cannot be reconstructed in the regions where the convection term in the formulation is close or less than the noise. To solve this issue, this dissertation proposes a method which is based on the use of multichannel receive coil in which each channel will have different convection term, and therefore low convective field region will differ from one channel to another. Combining each receive channel data in a logical manner, artifact free EP reconstructions are achieved. Since the proposed method based on the receive sensitivities of each channel, B_1^- based new cr-MREPT formulation has been derived. Additionally, to decouple the receive sensitivities from proton density, a new approach, which

is based on the transcieve phase assumption (TPA), has been proposed. Numerical simulations, phantom experiments, and healthy volunteer studies have been conducted to validate the proposed method.

The second method is called generalized phase based electrical conductivity imaging [55, 56]. In this method, a new formulation for phase based EPT approach has been derived in the light of the cr-MREPT formulation to solve the boundary artifact issue in the conventional phase based EPT approach. Additionally, the proposed method solves the LCF artifact issue in the conventional cr-MREPT method by adding a stabilization term in the equation. With these advantages, and the inherent advantages of phase-based EPT approach (fast, practically applicable for any transmit coil configuration, TPA free), the proposed method meets all the demands stated in the beginning of this section, and paves the way for fast and reliable electrical conductivity imaging in the clinical applications. The numerical simulations, phantom experiments, and healthy volunteer studies have been conducted for the validation of the proposed method. Also, comprehensive study has been made to investigate the limitation of the phase based EPT approaches that are the conventional and the proposed method. Last but not least, initial clinical trials have been conducted using the proposed method for two patients with neurovascular diseases in the subacute phase, i.e. hemorrhagic and ischemic stroke [57].

1.4 Organization of the Dissertation

The dissertation consists of five chapters:

Chapter 2 presents the theoretical background of the conventional MREPT, cr-MREPT, and the phase (or magnitude) based EPT methods, which are the most established MREPT methods so far. Although some information about these methods were given in the previous sections, the derivations of the central equations and the limitations of these methods will be explained in detail in this chapter. At the end of this chapter, the motivation of the proposed methods

will be stated by explaining the issues in the conventional methods, which are necessary to be solved in order for the clinical applications of the MREPT.

Chapter 3 presents the one of the proposed methods of this dissertation, which is named as B_1^- based multichannel cr-MREPT. It explains the reconstruction of EPs using multi-channel receive coils in order to solve LCF artifact issue in the conventional cr-MREPT method. Additionally, it presents a new approach finding B_1^- of each channel using transcieve phase assumption (TPA). Starting with the theoretical formulation of the proposed method, this chapter explains the methodology and presents the results of the proposed method, and finally concludes with the discussion section.

Chapter 4 presents the other proposed method of this dissertation, which is called generalized phase based electrical conductivity imaging. It explains the new phase based MREPT approach, which solves all the demands stated in Chapter 2, and shows the clinical applicability of this method. Similar to the Chapter 3, starting with the theoretical formulation, this chapter explains the methodology and presents the simulation, experiment, and healthy volunteer results of the proposed method. Additionally, rigorous analysis on the assumptions, which are made by the conventional and the proposed phase based EPT approaches, is presented in this chapter. Furthermore, EPs of two patients with neurovascular diseases have been studied using the proposed method, and this chapter presents the results of these studies. Finally it concludes with the discussion section.

Although each chapter presents its conclusion in its own Discussion section, Chapter 5 re-summarizes the contributions of this dissertation with the publications made by the author. This chapter concludes by stating the possible future directions.

Chapter 2

THEORETICAL BACKGROUND: A LITERATURE SURVEY

This chapter presents the theoretical background of the most established MREPT methods. In the first section of this chapter, the theory of the conventional MREPT method will be presented [36]. The idea will be explained with the electromagnetic derivations, and the limitations of the method will be stated. In the second section, phase and magnitude based MREPT approaches will be explained [50]. In the third section, the same concepts will be explained for the cr-MREPT method [43], which was proposed to solve the boundary artifact issue in the conventional method. In the end, the current state of the MREPT will be summarized with the drawbacks and challenges of these studies, the needs are clearly stated in order for the MREPT to be used in a standard clinical application, and the chapter concludes with the brief explanation of the proposed methods.

2.1 Magnetic Resonance Electrical Properties Tomography (MREPT)

As previously mentioned, MREPT aims to image electrical properties (EPs), i.e conductivity (σ) and dielectric permittivity (ϵ), of tissues at the Larmor frequency of an MRI system. In MREPT, induced currents are generated in the object during the RF excitation, and the secondary magnetic field due to these currents perturbs the applied RF magnetic field. This phenomena is undesirable for the conventional MR imaging because the inhomogeneity in the applied RF magnetic field makes the flip angle also inhomogeneous. However, MREPT makes use of this perturbation in the magnetic field to find the EPs. Therefore, the basic idea of the MREPT method is that the electrical properties can be calculated by measuring the perturbed magnetic field via MRI.

2.1.1 Formulation of MREPT

Starting with Maxwell's equations, taking the curl of Ampere's law (with Maxwell's addition), and substituting the electric field with magnetic field using Faraday's law, one can obtain Eq. 1.1 which is re-written below:

$$-\nabla^2\mathbf{B} = \frac{\nabla\gamma}{\gamma} \times (\nabla \times \mathbf{B}) - i\omega\mu\gamma\mathbf{B} \tag{2.1}$$

where $\mathbf{B}$ is the magnetic flux density, $\mathbf{B} = (B_x, B_y, B_z)$, γ is the complex permittivity, $\gamma = \sigma + i\omega\epsilon,\ \omega$ is the Larmor frequency, and μ is the magnetic permeability. Both $\mathbf{B}$ and γ are the function of space, $\mathbf{r} = (x, y, z)$, and the magnetic permeability will be taken as μ_0 throughout the dissertation.

If the electrical properties are assumed to be constant in tissue compartments, the gradient term ($\frac{\nabla\gamma}{\gamma} \times (\nabla \times \mathbf{B})$) in Eq. 2.1 vanishes, and writing the rest of the equation for γ gives

$$\gamma = \frac{\nabla^2 \mathbf{B}}{i\omega\mu_0 \mathbf{B}} \tag{2.2}$$

To solve Eq. (2.2), at least one spatial component (or linear combination of spatial components) of $\mathbf{B}$ must be known. In MRI, we can only measure B_1^+ which is the excitatory (or left-hand rotating) component of the magnetic field, and can be expressed as $B_1^+ = \frac{B_x + iB_y}{2}$. Similarly, B_1^-, right-hand rotating component of the magnetic field, can be expressed as $B_1^- = \frac{B_x - iB_y}{2}$ [58]. Alternatively, B_1^+ and B_1^- are sometimes called transmit and receive sensitivity of the RF coil, respectively. Using the linear combination of x- and y- components of Eq. 2.2, one can rewrite the equation in terms of measurable MR quantities as

$$\gamma = \frac{\nabla^2 B_1^{\pm}}{i\omega\mu_0 B_1^{\pm}} \tag{2.3}$$

Eq. 2.3 is the central equation of conventional MREPT methods [36–38, 50].

2.1.2 Limitations

As briefly explained in the Introduction chapter, there are several drawbacks and challenges of using Eq. 2.3. They are explained in detail as follows:

Boundary artifact issue: Since the gradient term in Eq. (2.1) is neglected, the conventional MREPT method is not able to reconstruct EPs in the tissue transition regions. Furthermore, an artifact, which is called boundary artifact, occurs at these regions. For better interpretation of this issue, electrical conductivity image, which was calculated using the conventional method in a simulation environment, is shown in Figure 2.1.

The conductivity map was obtained using the simulation phantom, which will be explained in the fourth chapter. As can be seen in Figure 2.1, the artifacts occur at the boundary of each compartment.

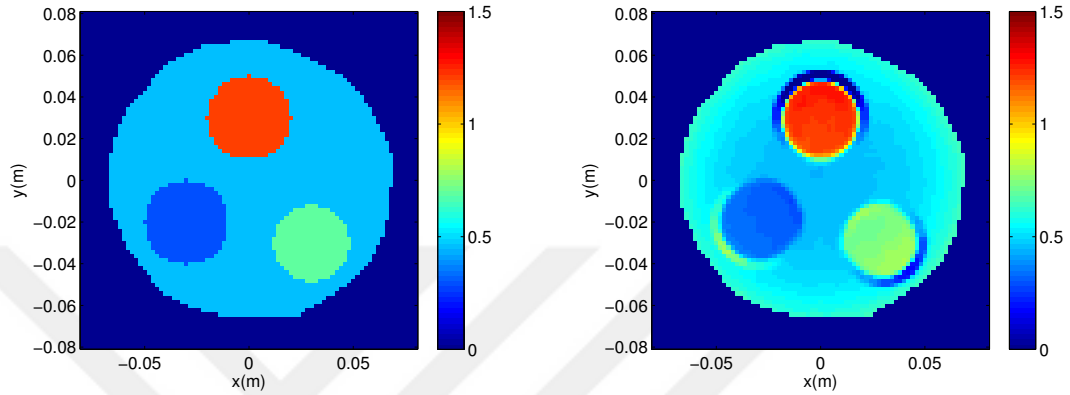

(a) (b)

Figure 2.1: Illustration of the boundary artifact issue. Results were obtained using the simulation phantom, which will be explained in the fourth chapter. (a) Actual conductivity (in S/m) (b) Reconstructed conductivity (in S/m) using conventional MREPT.

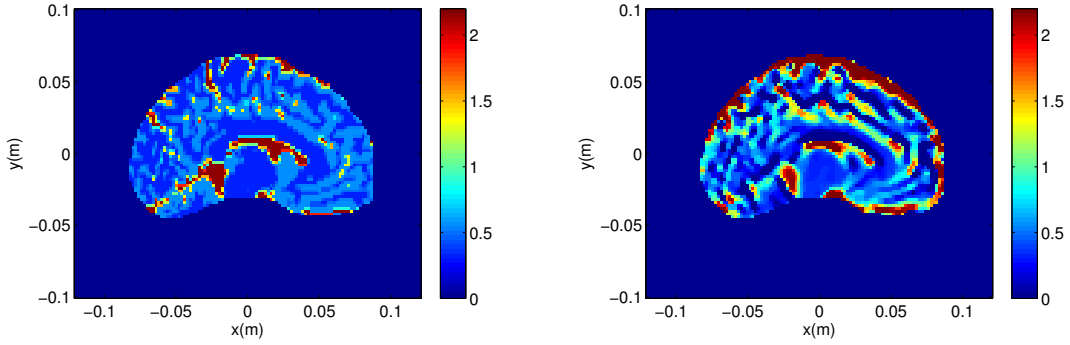

(a) (b)

Figure 2.2: Illustration of the boundary artifact issue. Results were obtained using the brain model simulations, which will be explained in the fourth chapter. (a) Actual conductivity (in S/m) (b) Reconstructed conductivity (in S/m) using conventional MREPT.

The boundary artifact seems to be not important for the phantom studies as shown in Figure 2.1 because the other regions (apart from the artifact) are well reconstructed. However, for the complex structures, e.g. brain, which has many tissue transitions, the boundary artifact issue significantly affects the EP images that can easily lead to misinterpretations in the clinical diagnosis. Figure 2.2 shows one such example, which was obtained using the brain simulation in the fourth chapter.

As shown in Figure 2.2, there are many boundary artifacts, which have negative value and appear as dark, in the conductivity image of the conventional MREPT method.

Transcieve phase assumption (TPA): To solve the central equation of MREPT (see Eq. 2.3), both the magnitude and the phase of the B_1^+ (or B_1^-) have to be known. The magnitude of B_1^+ can be found using any B_1 mapping technique [39–42]. Finding the phase of B_1^+, on the other hand, is not straightforward since the measured phase in MRI is the combination of both B_1^+ and B_1^- phases. Temporary solution to this problem is to use a quadrature birdcage coil for both transmit and receive operations, in which the transmit sensitivity can be approximated as the receive sensitivity ($B_1^+ \approx B_1^-$). This approximation also implies that $|B_1^+| \approx |B_1^-|$ and $\phi^+ \approx \phi^-$. Here, ϕ^+ and ϕ^- are the transmit and receive phases, respectively. Using this approximation the transmit phase can be approximated as half of the measured transcieve phase ($\phi^{tr} = \phi^+ + \phi^-$) that is $\phi^+ \approx \frac{\phi^{tr}}{2}$. This approximation (or assumption) is called transcieve phase assumption (TPA).

The validity of this assumption has been studied in [59], and it was found that TPA is not generally valid for elliptical objects, e.g. brain. Also, the validity of the assumption reduces at high field strengths. Therefore, TPA is another important limitation of the conventional MREPT methods, especially for the higher field strengths.

Signal-to-Noise ratio (SNR): Since MREPT uses Laplacian operator in the calculation of EPs, the method is very sensitive to noise. Additionally, B_1

mapping techniques also enhance the noise in the MR images, therefore Laplacian of noisy B_1 data will give more noisy EP images. To tackle with the noise, low-pass filter is generally applied which reduces the resolution of EP maps. Quantitative analysis of SNR in MREPT has been well documented in a recent paper published by Lee et. al. [60].

To tackle these limitations, several approaches, which was mentioned in Section 1.2, have been proposed. Among them, phase based EPT approach can reconstruct EPs without using TPA, and convection reaction based MREPT (cr-MREPT) approach solves the boundary artifact issue but they have other limitations. In the following two sections, these two methods will be explained in detail.

2.2 Magnitude and Phase based EPT

If we rewrite Eq. 2.3 in terms of magnitude and phase of the B_1 terms, using the definitions of $B_1^{\pm} = |B_1^{\pm}|e^{i\phi^{\pm}}$, we will obtain

$$\gamma = \frac{\nabla^2(|B_1^{\pm}|e^{i\phi^{\pm}})}{i\omega\mu_0(|B_1^{\pm}|e^{i\phi^{\pm}})} \tag{2.4}$$

Using the identity of $\nabla^2(ab) = a\nabla^2 b + 2\nabla a \cdot \nabla b + b\nabla^2 a$, the numerator in Eq. 2.4 can be written as $\nabla^2(|B_1^{\pm}|e^{i\phi^{\pm}}) = |B_1^{\pm}|\nabla^2 e^{i\phi^{\pm}} + 2\nabla|B_1^{\pm}| \cdot \nabla e^{i\phi^{\pm}} + e^{i\phi^{\pm}}\nabla^2|B_1^{\pm}|$. Each term in this equation can be expressed as follows:

$$|B_1^{\pm}|\nabla^2 e^{i\phi^{\pm}} = |B_1^{\pm}|e^{i\phi^{\pm}}(-\nabla\phi^{\pm} \cdot \nabla\phi^{\pm} + i\nabla^2\phi^{\pm}) \tag{2.5}$$

$$2\nabla|B_1^{\pm}| \cdot \nabla e^{i\phi^{\pm}} = ie^{i\phi^{\pm}}(2\nabla|B_1^{\pm}| \cdot \nabla\phi^{\pm}) \tag{2.6}$$

$$e^{i\phi^{\pm}}\nabla^2|B_1^{\pm}| = e^{i\phi^{\pm}}\nabla^2|B_1^{\pm}| \tag{2.7}$$

Substituting Eq. 2.5 - 2.7 into Eq. 2.4, the common term, $e^{i\phi^{\pm}}$, in the numerator and the denominator will cancel, and the final equation will be

$$\gamma = \frac{\nabla^2|B_1^{\pm}| - |B_1^{\pm}|(\nabla\phi^{\pm}\cdot\nabla\phi^{\pm}) + i(2\nabla|B_1^{\pm}|\cdot\nabla\phi^{\pm} + |B_1^{\pm}|\nabla^2\phi^{\pm})}{i\omega\mu_0|B_1^{\pm}|} \tag{2.8}$$

Eq. 2.8 includes both real and imaginary terms. Using the definition of $\gamma = \sigma + i\omega\epsilon$, and separating real and imaginary terms yields

$$\sigma = \frac{1}{\omega\mu_0}\left(\frac{2\nabla|B_1^{\pm}|\cdot\nabla\phi^{\pm}}{|B_1^{\pm}|} + \nabla^2\phi^{\pm}\right) \tag{2.9}$$

$$\epsilon = \frac{1}{\omega\mu_0^2|B_1^{\pm}|}\left(|B_1^{\pm}|(\nabla\phi^{\pm}\cdot\nabla\phi^{\pm}) - \nabla^2|B_1^{\pm}|\right) \tag{2.10}$$

Assuming $\nabla^2\phi^{\pm} >> \frac{2\nabla|B_1^{\pm}|\cdot\nabla\phi^{\pm}}{|B_1^{\pm}|}$ yields phase based EPT for conductivity imaging

$$\sigma \approx \frac{\nabla^2\phi^{\pm}}{\omega\mu_0} \tag{2.11}$$

Assuming $\nabla^2|B_1^{\pm}| >> |B_1^{\pm}|(\nabla\phi^{\pm}\cdot\nabla\phi^{\pm})$ yields magnitude based EPT for permittivity imaging

$$\epsilon \approx \frac{-\nabla^2|B_1^{\pm}|}{\omega\mu_0^2|B_1^{\pm}|} \tag{2.12}$$

Eq. 2.11 plays an important role for the clinical application of MREPT because the linearity of the expression enables the phase based electrical conductivity imaging using the measured transcieve phase, $\phi^{tr} = \phi^{+} + \phi^{-}$, as given in the following expressions:

$$\begin{aligned}\sigma &\approx \frac{\nabla^2\phi^{\pm}}{\omega\mu_0} \approx \frac{\nabla^2\phi^{+}}{\omega\mu_0} \approx \frac{\nabla^2\phi^{-}}{\omega\mu_0} \\ &\approx \frac{\nabla^2(\phi^{+}+\phi^{-})}{2\omega\mu_0} \\ &\approx \frac{\nabla^2\phi^{tr}}{2\omega\mu_0}\end{aligned} \tag{2.13}$$

Eq. 2.13 is the central equation of phase based EPT for conductivity imaging based on the measured transcieve phase in MRI, and therefore it does not use TPA to estimate the ϕ^{+}. With this improvement, phase based conductivity imaging can be employed for any coil configuration instead of using quadrature birdcage coil as long as $\nabla|B_1^{\pm}| = 0$ are fulfilled. Additionally, since the method only uses phase, it does not require B_1 mapping and it allows fast electrical conductivity imaging even in real time [61]. However there are some limitations of this method. Since the method is based on Eq. 2.3, the most important limitation is the boundary artifact issue. Additionally, the accuracy of Eq. 2.13 reduces when the $\omega\epsilon$ term gets larger than σ term [50,59]. This motivates the phase based electrical conductivity imaging at low field strength but the detailed investigation of this assumption will be given in the fourth chapter.

2.3 Convection-Reaction Equation based MREPT (cr-MREPT)

To solve the boundary artifact issue, Hafalir et al. proposed a new formulation for MREPT, called cr-MREPT, in which they include also the gradient term in Eq. 2.1 [43]. The final partial differential equation is in the form of convection reaction equation, and the coefficients of the equation are the first and the second derivatives of the complex B_1^{+}. Theoretical derivation of this method is the following:

Writing the x- and y- components of Eq. 2.1 will give

$$-\nabla^2 B_x = \frac{1}{\gamma}\left[\frac{\partial\gamma}{\partial y}\left(\frac{\partial B_y}{\partial x}-\frac{\partial B_x}{\partial y}\right)-\frac{\partial\gamma}{\partial z}\left(\frac{\partial B_x}{\partial z}-\frac{\partial B_z}{\partial x}\right)\right]-i\omega\mu_0\gamma B_x \tag{2.14}$$

$$-\nabla^2 B_y = \frac{1}{\gamma}\left[\frac{\partial\gamma}{\partial z}\left(\frac{\partial B_z}{\partial y}-\frac{\partial B_y}{\partial z}\right)-\frac{\partial\gamma}{\partial x}\left(\frac{\partial B_y}{\partial x}-\frac{\partial B_x}{\partial y}\right)\right]-i\omega\mu_0\gamma B_y \tag{2.15}$$

Multiplying y-component by i, and adding to x-component gives

$$\begin{aligned}-2\nabla^2 B_1^+ = \frac{1}{\gamma}\Bigg[&\frac{\partial\gamma}{\partial y}\left(\frac{\partial B_y}{\partial x}-\frac{\partial B_x}{\partial y}\right)- \\ &\frac{\partial\gamma}{\partial z}\left(2\frac{\partial B_1^+}{\partial z}-\frac{\partial B_z}{\partial x}-i\frac{\partial B_z}{\partial y}\right)-\frac{\partial\gamma}{\partial x}i\left(\frac{\partial B_y}{\partial x}-\frac{\partial B_x}{\partial y}\right)\Bigg]-i2\omega\mu_0\gamma B_1^+\end{aligned} \tag{2.16}$$

where $B_1^+ = \frac{B_x+iB_y}{2}$ was already defined. Using the definition of B_1^+ and Gauss's Law, $\nabla\cdot\mathbf{B}=0$, one can write the common term in Eq. 2.16 in terms of B_1^+ as

$$\left(\frac{\partial B_y}{\partial x}-\frac{\partial B_x}{\partial y}\right) = -2i\left(\frac{\partial B_1^+}{\partial x}-i\frac{\partial B_1^+}{\partial y}+\frac{1}{2}\frac{\partial B_1^+}{\partial z}\right) \tag{2.17}$$

Substituting Eq. 2.17 into Eq. 2.16 gives

$$\begin{aligned}-\nabla^2 B_1^+ = -\frac{1}{\gamma}\Bigg[&\frac{\partial\gamma}{\partial x}\left(\frac{\partial B_1^+}{\partial x}-i\frac{\partial B_1^+}{\partial y}+\frac{1}{2}\frac{\partial B_z}{\partial z}\right)+ \\ &\frac{\partial\gamma}{\partial y}\left(i\frac{\partial B_1^+}{\partial x}+\frac{\partial B_1^+}{\partial y}+i\frac{1}{2}\frac{\partial B_z}{\partial z}\right)+ \\ &\frac{\partial\gamma}{\partial z}\left(-\frac{1}{2}\frac{\partial B_z}{\partial x}-i\frac{1}{2}\frac{\partial B_z}{\partial y}+\frac{\partial B_1^+}{\partial z}\right)\Bigg]-i\omega\mu_0\gamma B_1^+\end{aligned} \tag{2.18}$$

Using the definition of $\frac{1}{\gamma}\left(\frac{\partial\gamma}{\partial x}\right) = \frac{\partial\ln(\gamma)}{\partial x}$, and writing this for all components yields B_1^+ based cr-MREPT algorithm in the logarithm form:

$$\boldsymbol{\beta}^+\cdot\nabla\ln(\gamma)-\nabla^2 B_1^+ + i\omega\mu_0\gamma B_1^+ = 0 \tag{2.19}$$

where

$$\gamma=\sigma+i\omega\epsilon, \qquad \nabla ln(\gamma)=\begin{bmatrix} \frac{\partial ln(\gamma)}{\partial x} \\ \frac{\partial ln(\gamma)}{\partial y} \\ \frac{\partial ln(\gamma)}{\partial z} \end{bmatrix}, \quad \boldsymbol{\beta}^{+}=\begin{bmatrix} \beta_x^{+} \\ \beta_y^{+} \\ \beta_z^{+} \end{bmatrix}=\begin{bmatrix} \frac{\partial B_1^{+}}{\partial x}-i\frac{\partial B_1^{+}}{\partial y}+\frac{1}{2}\frac{\partial B_z}{\partial z} \\ i\frac{\partial B_1^{+}}{\partial x}+\frac{\partial B_1^{+}}{\partial y}+i\frac{1}{2}\frac{\partial B_z}{\partial z} \\ -\frac{1}{2}\frac{\partial B_z}{\partial x}-i\frac{1}{2}\frac{\partial B_z}{\partial y}+\frac{\partial B_1^{+}}{\partial z} \end{bmatrix}$$

Eq. 2.19, which is in the form of convection-reaction equation, is the central equation of B_1^+ based cr-MREPT algorithm [43]. Since the gradient of the EPs are also included in the formulation, cr-MREPT is able to reconstruct tissue transition regions. Therefore it has no boundary artifact in the reconstructed EP maps, which is the superiority of the cr-MREPT method over the conventional MREPT method.

The coefficients of the partial differential equation (PDE) are the first derivatives and Laplacian of complex B_1^+. Therefore, to solve Eq. 2.19, both the magnitude and the phase of the B_1^+ have to be known. This is one of the limitations of this method because in order to find the phase of B_1^+ the method uses TPA, which was explained in Section 2.1.2.

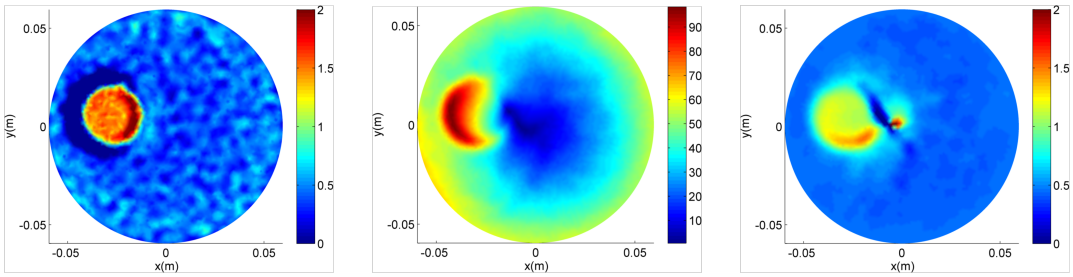

(a) (b) (c)

Figure 2.3: Illustration of the boundary artifact and LCF artifact issue. Results were obtained from the phantom experiment, which will be explained in the third chapter. (a) Reconstructed conductivity (in S/m) using conventional MREPT. (b) Magnitude of the convective field (inA/m^2) (c) Reconstructed conductivity (in S/m) using cr-MREPT.

The other limitation of cr-MREPT method is the low convective field (LCF) artifact. In Eq. 2.19, $(\boldsymbol{\beta}^{+} \cdot \nabla \ln(\gamma))$ is the convection term and $\boldsymbol{\beta}^{+}$ is the convective field. If the magnitude of the convective field is close to zero, high variations in the solution of γ are allowed at that region because $\boldsymbol{\beta}^{+}$ term multiplies the

first derivatives of γ. These bipolar variations appears as an artifact in the image, which is called as "spot-like artifact" or "LCF artifact", and it can be seen in Figure 2.3 given above

As can be seen in Figure 2.3 (c), cr-MREPT can reconstruct boundaries of an object but it has a LCF artifact in the region where the convective field is low (see 2.3 (b)).

2.4 Proposed Methods

By considering the above drawbacks and challenges, the needs in order for the MREPT to be used in standard clinical applications can be summarized as follows:

- ability of fast reconstruction
- applicability for any coil configuration
- artifact (boundary artifact and LCF artifact) free reconstruction
- transcieve phase assumption (TPA) free formulation

To address these needs in MREPT, two novel approaches have been proposed in this dissertation.

One of them is "B_1^- based multichannel cr-MREPT" algorithm, which aims to solve the LCF artifact issue in the conventional cr-MREPT method by using multichannel receive coil system. With this improvement, artifact-free reconstruction will be possible for MREPT, but the method is still based on TPA. This approach will be discussed in the next chapter.

The other approach is called "Generalized Phase based Conductivity Imaging", which aims to fulfill all the needs given above. For this purpose, a new formulation for phase based conductivity imaging method (given in Section 2.2) was made by

including the derivative of EPs, which solves the boundary artifact issue. This derivation was done in the light of the cr-MREPT method, and therefore the final PDE is in the form of convection-reaction-diffusion equation, in which the coefficients are solely based on the transcieve phase. With these improvements, fast, practically applicable, artifact and TPA free reconstruction will be possible for conductivity imaging. This approach will be discussed in the fourth chapter.

Chapter 3

B_1^- BASED MULTICHANNEL cr-MREPT

In this chapter, receive sensitivity, B_1^-, based multichannel cr-MREPT approach has been presented [53, 54]. This method is one of the main contributions of this dissertation. The purpose of the proposed method is to solve LCF artifact issue in the conventional B_1^+ based cr-MREPT method, and is to provide artifact-free EP images. As mentioned in the previous chapter, LCF artifact occurs in the regions where the magnitude of the convective field is close to or less than noise. To tackle this issue, in this method, multichannel receive coil configuration has been employed in which the location of the low convective field region differs from one channel to another. Combining each receive channel data in a logical manner, artifact free EP reconstructions in the ROI was obtained. Since B_1^- of each channel is used in the calculations, a new cr-MREPT formulation, which is based on the receive sensitivity of each channel, has been derived. The use of multi-channel receive coils also provides another contribution that the method is not limited to use of quadrature birdcage coils rather standard receive array coils, which are widely used in MRI, can be employed in the reconstruction of EPs. The method has been successfully applied in simulations, experimental phantom and healthy human brain experiments.

3.1 Theory

The derivation of B_1^+ based cr-MREPT approach was explained in Section 2.3. Using the similar steps, B_1^- based formulation was obtained.

3.1.1 Derivation of the Central Equation

Using the previously obtained x- and y- components of the Helmholtz equation (see Eq. 2.14 and Eq. 2.15), and multiplying y-component by i, and subtracting it from x-component gives

$$\begin{aligned}-2\nabla^2 B_1^- = \frac{1}{\gamma}\Bigg[&\frac{\partial\gamma}{\partial y}\left(\frac{\partial B_y}{\partial x}-\frac{\partial B_x}{\partial y}\right)- \\ &\frac{\partial\gamma}{\partial z}\left(2\frac{\partial B_1^-}{\partial z}-\frac{\partial B_z}{\partial x}+i\frac{\partial B_z}{\partial y}\right)+\frac{\partial\gamma}{\partial x}i\left(\frac{\partial B_y}{\partial x}-\frac{\partial B_x}{\partial y}\right)\Bigg]-i2\omega\mu_0\gamma B_1^-\end{aligned} \tag{3.1}$$

where $B_1^- = \frac{B_x - iB_y}{2}$. Using this definition of B_1^- and Gauss's Law, $\nabla\cdot\mathbf{B}=0$, the common term in Eq. 3.1, $\left(\frac{\partial B_y}{\partial x}-\frac{\partial B_x}{\partial y}\right)$, can be written in terms of B_1^- as

$$\left(\frac{\partial B_y}{\partial x}-\frac{\partial B_x}{\partial y}\right) = 2i\left(\frac{\partial B_1^-}{\partial x}+i\frac{\partial B_1^-}{\partial y}+\frac{1}{2}\frac{\partial B_1^-}{\partial z}\right) \tag{3.2}$$

Substituting Eq. 3.2 into Eq. 3.1 gives

$$\begin{aligned}-\nabla^2 B_1^- = -\frac{1}{\gamma}\Bigg[&\frac{\partial\gamma}{\partial x}\left(\frac{\partial B_1^-}{\partial x}+i\frac{\partial B_1^-}{\partial y}+\frac{1}{2}\frac{\partial B_z}{\partial z}\right)+ \\ &\frac{\partial\gamma}{\partial y}\left(-i\frac{\partial B_1^-}{\partial x}+\frac{\partial B_1^-}{\partial y}-i\frac{1}{2}\frac{\partial B_z}{\partial z}\right)+ \\ &\frac{\partial\gamma}{\partial z}\left(-\frac{1}{2}\frac{\partial B_z}{\partial x}+i\frac{1}{2}\frac{\partial B_z}{\partial y}+\frac{\partial B_1^-}{\partial z}\right)\Bigg]-i\omega\mu_0\gamma B_1^-\end{aligned} \tag{3.3}$$

Using the definition of derivative of logarithmic functions, $\frac{1}{\gamma}\left(\frac{\partial\gamma}{\partial x}\right) = \frac{\partial \ln(\gamma)}{\partial x}$, and writing this for all components yields B_1^- based cr-MREPT algorithm in the logarithm form:

$$\boldsymbol{\beta}^{-} \cdot \nabla \ln(\gamma) - \nabla^2 B_1^{-} + i\omega\mu_0\gamma B_1^{-} = 0 \tag{3.4}$$

where

$$\gamma = \sigma + i\omega\epsilon, \quad \nabla ln(\gamma) = \begin{bmatrix} \frac{\partial ln(\gamma)}{\partial x} \\ \frac{\partial ln(\gamma)}{\partial y} \\ \frac{\partial ln(\gamma)}{\partial z} \end{bmatrix}, \quad \boldsymbol{\beta}^{-} = \begin{bmatrix} \beta_x^{-} \\ \beta_y^{-} \\ \beta_z^{-} \end{bmatrix} = \begin{bmatrix} \frac{\partial B_1^{-}}{\partial x} + i\frac{\partial B_1^{-}}{\partial y} + \frac{1}{2}\frac{\partial B_z}{\partial z} \\ -i\frac{\partial B_1^{-}}{\partial x} + \frac{\partial B_1^{-}}{\partial y} - i\frac{1}{2}\frac{\partial B_z}{\partial z} \\ -\frac{1}{2}\frac{\partial B_z}{\partial x} + i\frac{1}{2}\frac{\partial B_z}{\partial y} + \frac{\partial B_1^{-}}{\partial z} \end{bmatrix}$$

Defining $u = \frac{1}{\gamma}$, Eq. 3.4 can be rewritten in the following form (instead of logarithm form)

$$\boldsymbol{\beta}^{-} \cdot \nabla u + \nabla^2 B_1^{-} u - i\omega\mu_0 B_1^{-} = 0 \tag{3.5}$$

Eq. 3.5 is the central equation of B_1^{-} based cr-MREPT algorithm, and the equation is in the form of well known convection-reaction-diffusion equation with null diffusion term. If the B_z can be measured in MRI, Eq. 3.5 can be solved for u in 3D but we cannot measure the z- component of the magnetic field. On the other hand, B_z terms can be neglected in the center of the birdcage coil where the magnetic field generated due to the end-ring current is very low compared to the transverse field. For the slice of interest, if $\frac{\partial u}{\partial z}$ is negligible, the 2D form of this method, which is given below, is used to reconstruct EPs.

$$\boldsymbol{F}^{-} \cdot \nabla u + \nabla^2 B_1^{-} u - i\omega\mu_0 B_1^{-} = 0 \tag{3.6}$$

where

$$u = \frac{1}{\gamma}, \quad \nabla u = \begin{bmatrix} \frac{\partial (u)}{\partial x} \\ \frac{\partial (u)}{\partial y} \end{bmatrix}, \quad \boldsymbol{F}^{-} = \begin{bmatrix} F_x^{-} \\ F_y^{-} \end{bmatrix} = \begin{bmatrix} \frac{\partial B_1^{-}}{\partial x} + i\frac{\partial B_1^{-}}{\partial y} \\ -i\frac{\partial B_1^{-}}{\partial x} + \frac{\partial B_1^{-}}{\partial y} \end{bmatrix}$$

Throughout this chapter, Eq. 3.6 will be used to solve EPs.

3.1.2 Finding the Complex B_1^-

To solve Eq. 3.6 for u, both the magnitude and the phase of the B_1^- have to be known. However, calculation of B_1^- is not straightforward since B_1^- is generally coupled with the proton density, M_0, in MRI. For this purpose, in addition to B_1^- based EP reconstruction algorithm, a TPA based new approach have been proposed to estimate B_1^-. This is another contribution of this dissertation to the literature. This approach was based on two consecutive examinations. In the first experiment, quadrature body coil (QBC) is used for both transmission and reception. In the second experiment, the same QBC is used for transmit, and any phased array (or surface coil) is used to receive, and we are interested in finding the B_1^- of each receive channel.

1st Experiment: For the first experiment, the signal equation for QBC can be written as [58]

$$|S_{QBC}|e^{i\phi_{QBC}} = V_1 M_0 \sin(V_2\alpha|B_1^+|)e^{i\phi^+}|B_1^-|e^{i\phi^-} \tag{3.7}$$

where, $|S_{QBC}|$ is the MR magnitude image, ϕ_{QBC} is the measured transcieve MR phase, $\phi_{QBC} = \phi^+ + \phi^-$, V_1 and V_2 are the system dependent constants, and α is the flip angle. For the simplicity, we define $|M^+| = V_1 M_0 \sin(V_2\alpha|B_1^+|)$.

Since QBC is used for transmit and receive, we can make use of the transcieve phase assumption (TPA) in which $B_1^+ \approx B_1^-$ (see Section 2.1.2). Using this approximation and Eq. 3.7, $|M^+|$ and ϕ^+ can be estimated as

$$\begin{aligned} |\hat{M}^+| &\approx \frac{|S_{QBC}|}{|B_1^+|} \\ \hat{\phi}^+ &\approx \frac{\phi_{QBC}}{2} \end{aligned} \tag{3.8}$$

In Eq. 3.8, $|B_1^+|$ can be found using any B_1 mapping technique [39–42], and

the other terms, $|S_{QBC}|$ and ϕ_{QBC}, which are MR magnitude and phase signals, are measurable quantities in MRI.

2nd Experiment: For the second experiment, the signal equation for phased array receive coil (or any surface coil) can be written as

$$|S_{PA,k}|e^{i\phi_{PA,k}} = |M^+|e^{i\phi^+}|B_{1,k}^-|e^{i\phi_k^-} \tag{3.9}$$

where, $|S_{PA,k}|$ and $\phi_{PA,k}$ are the MR magnitude and the transcieve phase images of the k^{th} channel of the phased array coil, respectively.

As can be seen in Eq. 3.9, estimated values in the first experiment, which are $|M^+|$ and ϕ^+, enters the signal equation of the second experiment because the transmit coil is the same. Therefore, magnitude and phase of the B_1^- for the k^{th} channel, which are $|B_{1,k}^-|$ and ϕ_k^- in Eq. 3.9, can be calculated as

$$\begin{aligned} |B_{1,k}^-| &\approx \frac{|S_{PA,k}|}{|\hat{M}^+|} \\ \phi_k^- &\approx \phi_{PA,k} - \hat{\phi}^+ \end{aligned} \tag{3.10}$$

After estimating complex $B_{1,k}^-$ maps for all channel, the coefficients of the Eq. 3.6, which are the first and the second derivatives of $B_{1,k}^-$, can be calculated. The solution of Eq. 3.6 will be given in the next section.

3.2 Methods

3.2.1 Solution of the Central Equation

To reconstruct σ and ϵ, Eq. 3.6 is solved for u. Prior to the reconstruction, the user first chooses a region of interest (ROI) from the MR magnitude image

(or simulated data) in which triangular mesh is generated, and the data are interpolated to the triangular mesh nodes.

The first and the second derivatives of B_1^- at the mesh nodes are calculated using the method proposed by Fernandez et al [62], which is the implementation of Savitzky-Golay filtering on a triangular mesh [63]. The idea of this method is the following: B_1^- at each node is approximated as the second order polynomial, and the coefficients of the polynomial are found for each node from the set of equations, which are written using the neighboring nodes. Then, the first and the second derivatives can be determined using the calculated coefficients.

After finding the first and the second derivatives of B_1^-, Eq. 3.6 is discretized using triangular mesh based finite difference method and transformed into a matrix equation which is in the form of $\mathbf{A}_{N_t \times N_p} \mathbf{u}_{N_p \times 1} = \mathbf{b}_{N_t \times 1}$. Here, N_t is the number of triangles, and N_p is the number of nodes in the ROI. As can be understood, each row represents the equation written for each triangle. Applying the Dirichlet boundary condition, u is solved in the least square sense. This is the same solution strategy which was proposed in the conventional cr-MREPT method [43], therefore more detailed explanation can be found in that study.

Different from the conventional cr-MREPT method, there will be many $\mathbf{A}$ matrices as the number of channel in the proposed method. The purpose is to use an appropriate channel data in which the LCF region is above the specified threshold value so that the LCF artifact does not occur. This threshold value is taken as the standard deviation of the noise in the convective field images. Alternatively, in some cases, the use of more than one channel at the same time can be required for larger ROI. In that cases, $\mathbf{A}$ matrices of the corresponding channels can be concatenated, and u is solved again in a least square sense. For those cases, the equations written for the triangles, which are in the region of low convective field, can be discarded from the matrix equation.

3.2.2 Simulation Methods

For the simulations, electromagnetic fields were generated using COMSOL Multiphysics (COMSOL AB, Sweden), finite element method (FEM) based software package. Figure 3.1 (a) shows the simulation phantom, which consists of three compartments (each compartment has the conductivity value of $\sigma = 1.2$ S/m and $\epsilon_r = 77$), and a background region ($\sigma = 0.45$ S/m and $\epsilon_r = 77$) (see Figure 3.1 (b)), and the surface coil which was used to generate electromagnetic fields. We have obtained four different B_1^- distributions by rotating the surface coil with 90 degree in each simulation. Therefore, it can be thought as a four-channel coil system. Figure 3.2 shows the magnitude and the phase of B_1^- distributions which were obtained using these four channels. In the simulations, B_1^- distributions were simply calculated using the definition of $B_1^- = \frac{B_x - iB_y}{2}$.

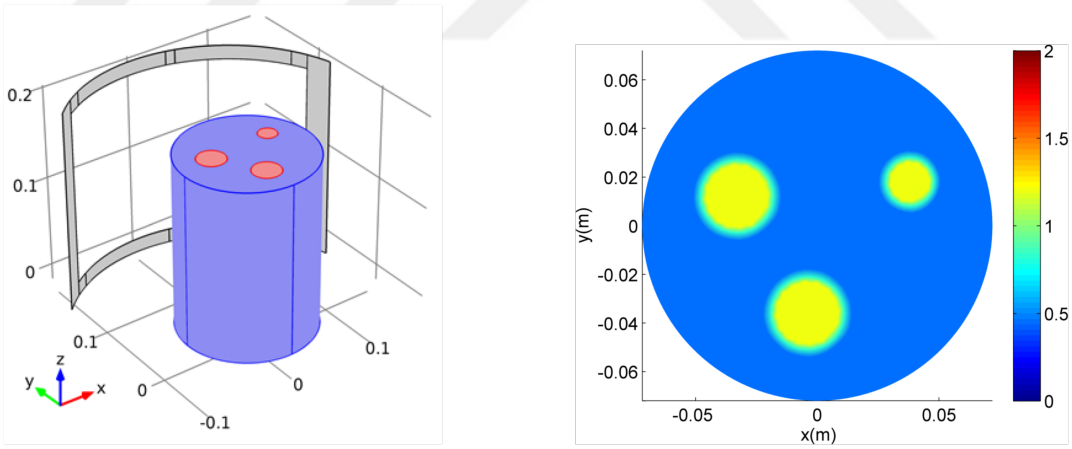

(a) (b)

Figure 3.1: (a) Simulation phantom and the surface coil model. (b) Actual conductivity at the central transverse slice (in S/m).

Coil positions of each simulation can be deduced from the receive sensitivity profiles which are given in Figure 3.2 (a). For example, the sensitivity profile of the coil position, which is given in Figure 3.1 (a), corresponds to the left bottom plot in Figure 3.2 (a).

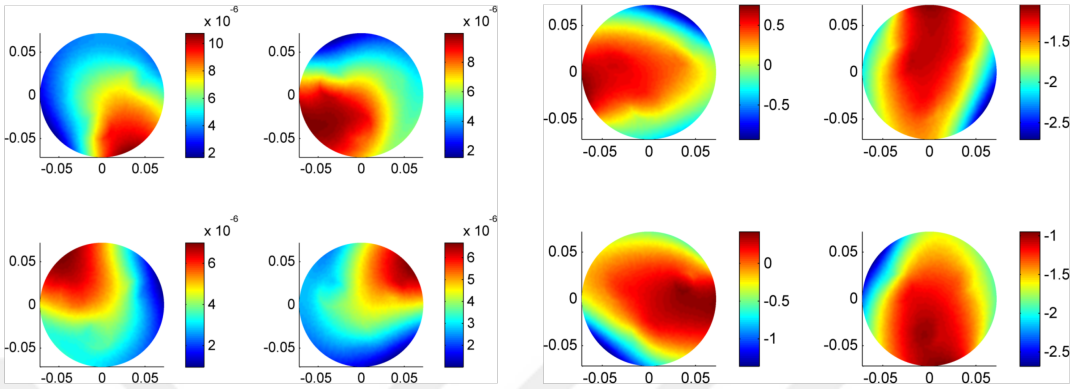

(a) (b)

Figure 3.2: (a) B_1^- magnitude distributions (T) (b) B_1^- phase distributions (rad) of each channel.

3.2.3 Experimental Methods

Phantom Setup

An experimental phantom, which consists of one anomaly and a background region, was set up. The background was prepared using an agar-saline solution (20 gr/l Agar, 2 gr/l NaCl, 0.4 gr/l $CuSO_4$), and the anomaly region, which has higher conductivity, was filled with saline solution (8 gr/l NaCl, 0.4 gr/l $CuSO_4$) after the background region was solidified. The conductivity values of the background and the anomaly regions are expected to be 0.5 S/m and 1.4 S/m, respectively. Relative dielectric permittivities of both regions are expected to be 80, which is same as the salt-free water.

In Vivo Human Experiment

A healthy male volunteer (age 30 years) has been studied with the approval of Institutional Review Board of Bilkent University. Electrical conductivity maps in the selected regions of brain were reconstructed using the B_1^- based cr-MREPT method.

Sequence Protocols and Reconstruction

Both phantom and human experiments were conducted on a 3T MR Scanner (Siemens, Erlangen, Germany) installed in UMRAM (National Magnetic Resonance Research Center) at Bilkent University. Standard quadrature body coil (QBC) and 12 channel receive-only phased array (PA) head coil were used in the experiments.

For the phantom experiment, $|B_1^+|$ map was calculated using actual flip angle (AFI) method (Tx: QBC, Rx: PA, FA=60, TR1/TR2=50/250 ms, FOV=200 mm, 1.56x1.56x4 mm, NEX=20, total scan time 13min). For complex B_1^- estimations two balanced steady state free precession (SSFP) sequences with the same sequence parameters (FA=60, TE/TR= 2.09/4.18 ms, FOV=200 mm, 1.56x1.56x5 mm, NEX=32, total scan time 40 sec) were applied. In the first experiment, QBC was used for both transmit and receive operations to estimate $|M^+|$ and ϕ^+ using TPA. In the second experiment, QBC was used only for transmit, and PA coil was used for receive operation to calculate the B_1^- of each channel of the PA coil, as explained in Section 3.1.2.

For the volunteer experiments, sequence parameters for AFI are the following: (FA=60, TR1/TR2=40/200 ms, FOV=250 mm, 1x1x4 mm, NEX=20, total scan time 20 min). For the balanced SSFP sequences the sequence parameters are as follows: (FA=50, TE/TR=2.3/4.6ms, FOV=250mm, 1x1x5 mm, NEX=32, total scan time 1 min).

3.3 Results

3.3.1 Simulation Results

Figure 3.3 shows the magnitude of the convective field and the corresponding conductivity results of each channel. In fact, the convective field has two components, which are F_x^- and F_y^-. As can be seen in Eq. 3.6, $F_x^- = iF_y^-$ that implies magnitudes of these terms are equal. Therefore, Figure 3.3 shows the magnitude of one component for each channel.

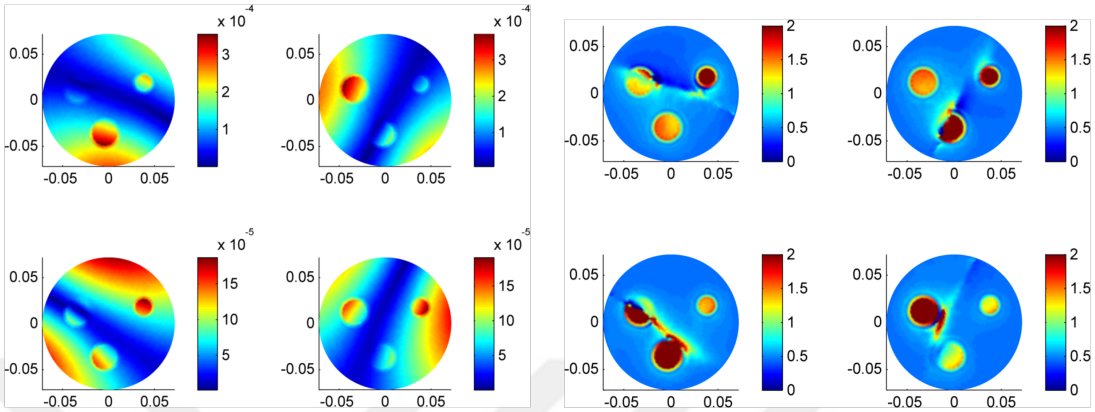

(a) (b)

Figure 3.3: (a) Magnitude of the convective fields (A/m^2) (b) Corresponding conductivity maps (S/m) of each channel

As shown in Figure 3.3 (a), different convective field distributions were obtained for different coil positions. It can also be seen that the low convective field (LCF) region differs from one channel to another, which is the desired situation and also the idea of the proposed method. Figure 3.3 (b) shows the corresponding conductivity distribution of each channel. The line shaped LCF artifacts, which occurs in the corresponding low convective field regions, can be clearly seen in the conductivity results. To combine all channel data, the method, which was explained in Section 3.2.1, was used. For each channel, we have totally four different matrix equations, and each matrix equation is written as shown in below Eq. 3.11.

$$\begin{bmatrix} \mathbf{A_1} \\ \mathbf{A_2} \\ \mathbf{A_3} \\ \mathbf{A_4} \end{bmatrix}_{4N_t \times N_p} \mathbf{u}_{N_p \times 1} = \begin{bmatrix} \mathbf{b_1} \\ \mathbf{b_2} \\ \mathbf{b_3} \\ \mathbf{b_4} \end{bmatrix}_{4N_t \times 1} \tag{3.11}$$

Solving Eq. 3.11 for u in a least square sense gives the combined reconstructed conductivity result which is shown in Figure 3.4.

This is a promising result that validates the applicability of the proposed

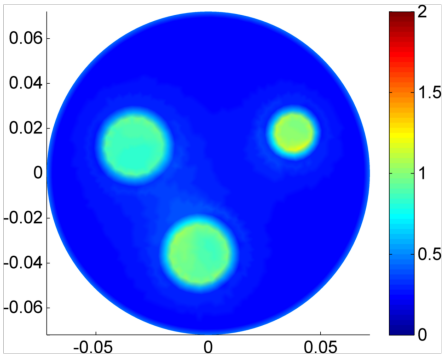

Figure 3.4: Reconstructed conductivity map using the combination of all four channel (S/m)

method in the ideal case (noise free and B_1^- distributions are exactly known). In practice, we cannot exactly find the B_1^- distributions of each channel, and also there will be noise. The performance of the proposed method under these conditions will be given in the next section.

3.3.2 Experimental Results

As explained in the Methods (Section 3.2), $|B_1^+|$ was calculated using AFI method, and two-experiments approach was used for complex B_1^- estimation. For the comparison purposes, the results of the conventional cr-MREPT and MREPT methods are shown in Figure 3.5. These two methods were performed using the first experiment and the calculated $|B_1^+|$.

Figure 3.5 (a) shows the magnitude of the convective field. The LCF region is close to the middle of the experimental phantom. Reconstructed conductivity distributions using the conventional cr-MREPT method and the MREPT method are shown in Figure 3.5 (b) and (c), respectively. The boundary artifact in the conventional MREPT method can be clearly seen in Figure 3.5 (c). The boundary artifact is removed in the conventional cr-MREPT method but it has LCF artifact in the low convective field region (see Figure 3.5 (b)). Both artifacts significantly affect the reconstructed conductivity maps.

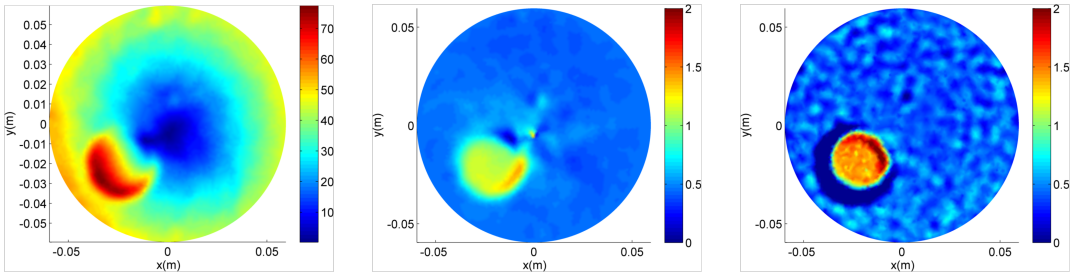

(a) (b) (c)

Figure 3.5: Results of the conventional cr-MREPT and MREPT methods. (a) The magnitude of the convective field (in A/m^2) (b) Reconstructed conductivity (in S/m) using B_1^+ based cr-MREPT. (c) Reconstructed conductivity (in S/m) using conventional MREPT.

Using the calculated $|B_1^+|$ and two experiments, proposed method first estimates the B_1^- distributions of each channel. Using these estimated complex B_1^- distributions, the coefficients of the central equation (Eq. 3.6) are calculated. Then, matrix equation is formed using these coefficients to solve the EPs. The magnitude of the convective fields and the corresponding conductivity results for all twelve channels are illustrated in the following Figure 3.6 and 3.7.

As can be seen, each channel has different convective field distribution, and the LCF artifact occurs in the conductivity results of all channels. Figure 3.6 (a),(b),(g),(h) and the corresponding conductivity results (Figure 3.7 (a),(b),(g),(h)) are very similar to the results of the simulation phantom. The only difference is that due to the noise in the experiments LCF region becomes wider which results in a large line shaped LCF artifact in the conductivity maps. The importance of the proposed method arises at this point. Combining the fifth and the eleventh channel (see Figure 3.7 (e) and (k)), the conductivity map, which is shown in Figure 3.8, is obtained.

When we compare the results of the proposed method with the results of the conventional cr-MREPT and the MREPT methods, we see that both artifacts, boundary and LCF artifacts, were significantly reduced in the proposed method. The other important result is that the application of the conventional cr-MREPT and MREPT methods were restricted to the specific coil type. By the proposed

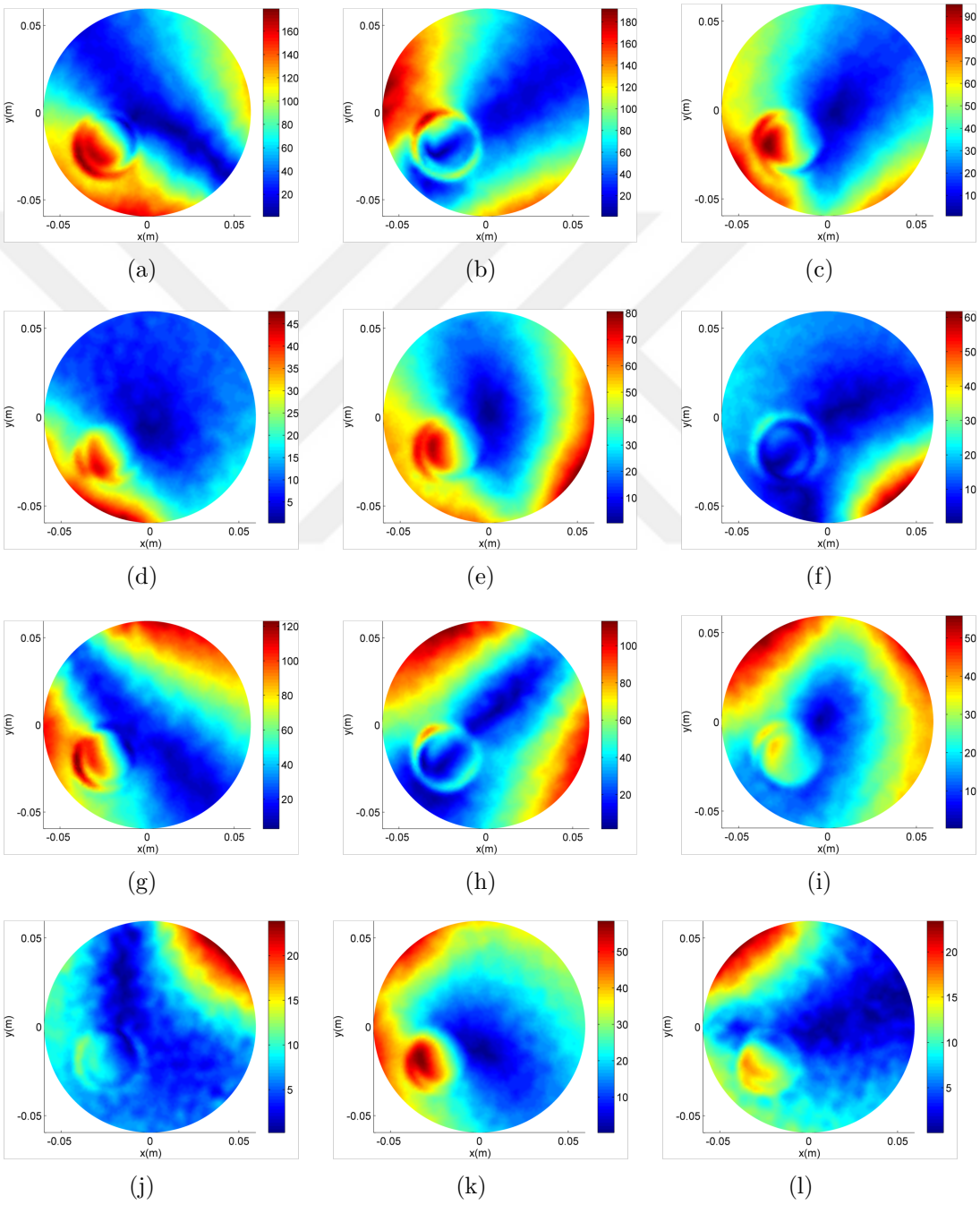

Figure 3.6: Magnitude of the convective field of each channel

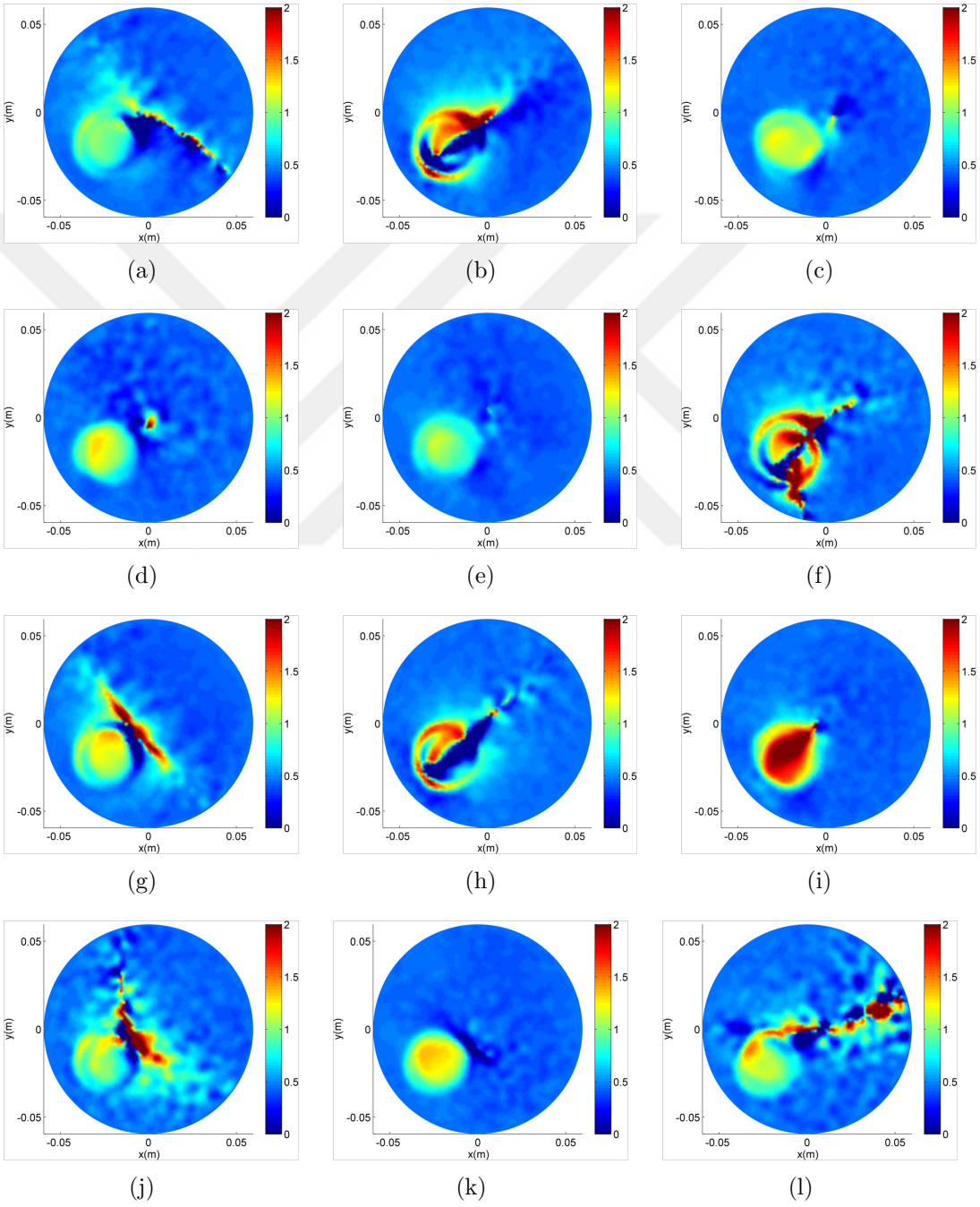

Figure 3.7: Reconstructed conductivity map of each channel (no combination)

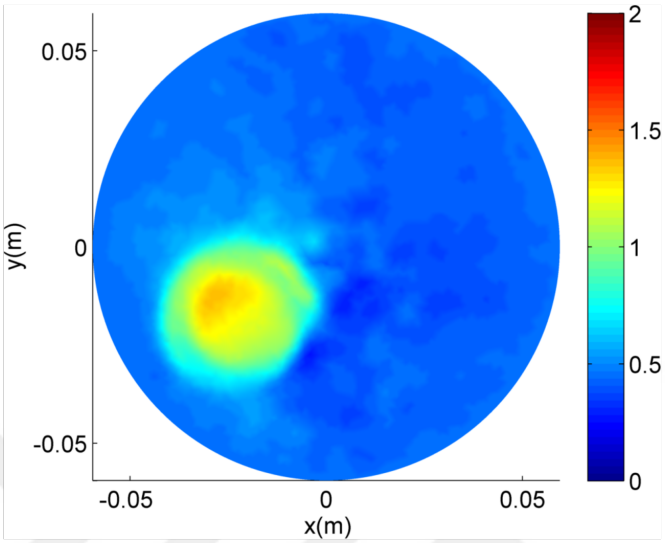

Figure 3.8: Reconstructed conductivity map using the combination of 5th and 11th channel (S/m)

method, this restriction also was removed and any standard coil configuration can be employed with a cost of one more experiment. On the other hand, the choice of combined channels in this experiment were made manually by visualizing the results of all channel but it can also be made automatically which will be discussed in the next section.

For the volunteer experiment, three different regions in the volunteer brain were selected (see Figure 3.9 (a)). The conductivity maps of these sections are shown in Figure 3.9 (b)-(d).

The calculated conductivity maps are consistent with the anatomical structure of the brain (see Figure 3.9 (a)), and the conductivity values are within the expected range when compared to the literature values [2–4]. EPs at the boundaries of selected regions were taken as $\sigma = 0.6$ S/m and $\epsilon_r = 77$. It was found that the exact value, which was assigned to the boundary, was not critical except for a narrow band near the boundary. Additionally, the selection of ROI also motivates the reconstruction of the conductivity distribution in a desired local region using the proposed method.

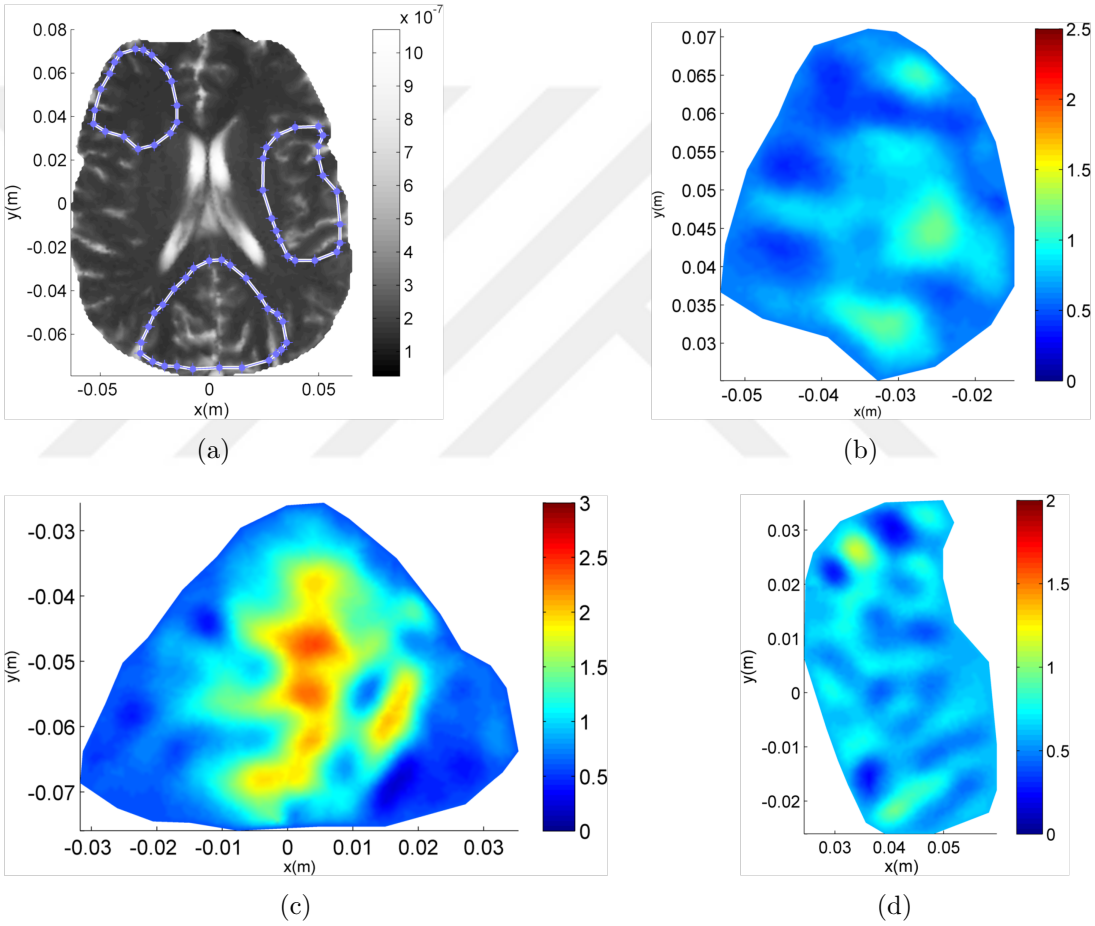

Figure 3.9: Results for the healthy volunteer study. (a) Selection of local regions, where the conductivity distributions are calculated, on the SSFP magnitude image (b-d) Corresponding reconstructed conductivity images using the proposed method (S/m)

3.4 Discussion

In this study, we have proposed B_1^- based multi-channel cr-MREPT approach to solve two important issues in the conventional MREPT methods. One is the well known LCF artifact issue in the cr-MREPT method. Since the conventional cr-MREPT method has the ability to reconstruct EPs at the boundaries of the tissue regions, it is important to solve its own artifact, i.e. LCF artifact, which occurs at the low convective field region. To solve this issue, the multi-channel receive coil configuration has been employed. The aim of this study is to reconstruct EPs using the receive sensitivity (B_1^-) of each channel instead of using the transmit sensitivity (B_1^+) as in the case of conventional methods. The reason is that the LCF region is expected to be different in each channel. If at least two channels have different LCF regions in the ROI, the artifact free EPs can be obtained using the combination of these channels. For this purpose, B_1^- based cr-MREPT formula has been derived, and the method has been validated in the simulations and experiments.

The second issue in the conventional MREPT methods is the limitation of using quadrature birdcage coil for both transmit and receive operations. The proposed method removes this limitation and enables the use of multi-channel receive systems in MREPT which are more widely used than the birdcage coil in practice for SNR and parallel imaging purposes. Furthermore, the necessity of finding B_1^- of each channel in the proposed method provides another contribution to the literature. Since the transcieve phase assumption (TPA) has already been made in the conventional methods, this study presents the estimation of B_1^- of each channel without making any approximation except the TPA. Instead, one more experiment has to be conducted for this purpose, which adds an extra one minute in the case of 2D human volunteer study.

In the combination of receive channel data the following algorithm has been used: First, LCF region is defined. For this purpose, we have taken a threshold value that is the standard deviation of the noise in the convective field images. If a region in the magnitude of the convective fields is below the threshold value, this

region is defined as the LCF region. If the LCF region of one channel is out of the ROI, and also if that region is the sensitive region of the coil than using only this channel will be enough for artifact free reconstruction. However, if this is not the case, at least two channel has been chosen from the data set in which the locations of the LCF regions of the selected channels do not coincide. In both cases, the selections have been made manually by looking at the magnitude of the convective fields and the receive sensitivity of each channel. In some cases, especially in more noisy experiments, LCF regions can coincide in any combination of the channels. In this case, again at least two channels are chosen manually, and the algorithm forms the matrix equation for the triangles which has higher convective field than the other channel in the LCF region. The triangles which have lower convective fields are discarded from the matrix equation. Therefore, after the selection of channels the rest has been performed automatically.

In the case of coinciding LCF regions in any combination of the channels, the performance of the proposed method decreases. The occurrence of this situation is possible when the noise in the experiment is high that results in a large LCF region. In such cases, to change the position of the LCF region, instead of using multi-channel receive coil, multi-channel transmit coils can also be used in which each transmit coil can be driven separately. This will provide more degrees of freedom when compared to the receive channels, and LCF region can be shifted by driving the each transmit channel with an optimum magnitude and phase. This can be thought as an RF shimming problem in which one more constraint, LCF region, can be added to the optimization process. Alternatively, for specific body parts, e.g. brain, multi-channel cr-MREPT coils can be designed in which the LCF regions of each channel do not coincide.

The other issues of the proposed method are the TPA and the duration of the examinations. As the conventional methods, the proposed method also relies on TPA, which starts to fail for elliptical objects, e.g. brain, and also at high field strengths [59]. Another issue is the duration of the experiments which includes B_1 mapping sequence and two SSFP sequences. These examinations take totally about 22 minutes for the case of 2D volunteer brain scan. The most of the time is spent on B_1 mapping sequence. In practice 3D scans of full brain will be the

case and for this situation fast B_1 mapping techniques [41, 64] have to be used instead of AFI.

In the next chapter, a different approach, which aims to solve all the drawbacks and challenges of the conventional methods and the B_1^- based cr-MREPT method, will be presented.

Chapter 4

GENERALIZED PHASE BASED ELECTRICAL CONDUCTIVITY IMAGING

In this chapter, generalized phase based electrical conductivity imaging method has been presented [55, 56]. This is the second main contribution of this dissertation. The aim of this study is to solve all the drawbacks and challenges in the MREPT methods that have already been mentioned in the previous chapters. Therefore, the purpose can be summarized as follows: To develop a fast and artifact free electrical conductivity imaging method, which is practically applicable for any coil configuration, and which do not use transcieve phase assumption (TPA). Starting from the Maxwell's equations and including the gradients of EPs into the equation a new electrical conductivity imaging method, which is solely based on the measurable MR transcieve phase, was proposed. The governing partial differential equation is in the form of convection reaction equation and it has been solved using 3D finite difference scheme which is implemented on the Cartesian grid. The method has been validated using numerical simulations, phantom and in vivo human experiments. Additionally, to explore the clinical applicability of the proposed method, two patients with neurovascular diseases, i.e. hemorrhagic and ischemic stroke, have been studied.

4.1 Theory

The central equation of B_1^+ and B_1^- based cr-MREPT approaches can be rewritten using the Eq. 2.19 and Eq. 3.4 as follows:

$$\boldsymbol{\beta}^{\pm} \cdot \nabla \ln(\gamma) - \nabla^2 B_1^{\pm} + i\omega\mu_0\gamma B_1^{\pm} = 0 \tag{4.1}$$

where

$$\gamma = \sigma + i\omega\epsilon, \quad \nabla ln(\gamma) = \begin{bmatrix} \frac{\partial ln(\gamma)}{\partial x} \\ \frac{\partial ln(\gamma)}{\partial y} \\ \frac{\partial ln(\gamma)}{\partial z} \end{bmatrix}, \quad \boldsymbol{\beta}^{\pm} = \begin{bmatrix} \beta_x^{\pm} \\ \beta_y^{\pm} \\ \beta_z^{\pm} \end{bmatrix} = \begin{bmatrix} \frac{\partial B_1^{\pm}}{\partial x} \mp i\frac{\partial B_1^{\pm}}{\partial y} + \frac{1}{2}\frac{\partial B_z}{\partial z} \\ \pm i\frac{\partial B_1^{\pm}}{\partial x} + \frac{\partial B_1^{\pm}}{\partial y} \pm i\frac{1}{2}\frac{\partial B_z}{\partial z} \\ -\frac{1}{2}\frac{\partial B_z}{\partial x} \mp i\frac{1}{2}\frac{\partial B_z}{\partial y} + \frac{\partial B_1^{\pm}}{\partial z} \end{bmatrix}$$

To obtain phase based formula, we first write the complex magnetic fields in Eq. 4.1 in terms of magnitude and phase components. Therefore, using the definition of $B_1^{\pm} = |B_1^{\pm}|e^{i\phi^{\pm}}$ and assuming $\nabla|B_1^{\pm}| = 0$, each term in Eq. 4.1 can be expressed as:

$$\beta_x^+ = \left|B_1^+\right| e^{i\phi^+} \left(i\frac{\partial}{\partial x}\phi^+ + \frac{\partial}{\partial y}\phi^+ \right) + \frac{1}{2}\frac{\partial B_z}{\partial z} \tag{4.2}$$

$$\beta_y^+ = \left|B_1^+\right| e^{i\phi^+} \left(-\frac{\partial}{\partial x}\phi^+ + i\frac{\partial}{\partial y}\phi^+ \right) + i\frac{1}{2}\frac{\partial B_z}{\partial z} \tag{4.3}$$

$$\beta_z^+ = \left|B_1^+\right| e^{i\phi^+} \left(i\frac{\partial}{\partial z}\phi^+ \right) - \frac{1}{2}\frac{\partial B_z}{\partial x} - i\frac{1}{2}\frac{\partial B_z}{\partial y} \tag{4.4}$$

$$\nabla^2 B_1^+ = \left|B_1^+\right| e^{i\phi^+} \left(-\left(\frac{\partial}{\partial x}\phi^+ \frac{\partial}{\partial x}\phi^+ + \frac{\partial}{\partial y}\phi^+ \frac{\partial}{\partial y}\phi^+ + \frac{\partial}{\partial z}\phi^+ \frac{\partial}{\partial z}\phi^+ \right) + i\nabla^2\phi^+ \right) \tag{4.5}$$

$$\beta_x^- = \left|B_1^-\right| e^{i\phi^-} \left(i\frac{\partial}{\partial x}\phi^- - \frac{\partial}{\partial y}\phi^- \right) + \frac{1}{2}\frac{\partial B_z}{\partial z} \tag{4.6}$$

$$\beta_y^- = \left|B_1^-\right| e^{i\phi^-} \left(\frac{\partial}{\partial x}\phi^- + i\frac{\partial}{\partial y}\phi^- \right) - i\frac{1}{2}\frac{\partial B_z}{\partial z} \tag{4.7}$$

$$\beta_z^- = \left|B_1^-\right| e^{i\phi^-} \left(i\frac{\partial}{\partial z}\phi^- \right) - \frac{1}{2}\frac{\partial B_z}{\partial x} + i\frac{1}{2}\frac{\partial B_z}{\partial y} \tag{4.8}$$

$$\nabla^2 B_1^- = \left|B_1^-\right| e^{i\phi^-} \left(-\left(\frac{\partial}{\partial x}\phi^- \frac{\partial}{\partial x}\phi^- + \frac{\partial}{\partial y}\phi^- \frac{\partial}{\partial y}\phi^- + \frac{\partial}{\partial z}\phi^- \frac{\partial}{\partial z}\phi^- \right) + i\nabla^2\phi^- \right) \tag{4.9}$$

where ϕ^+ and ϕ^- are transmit and receive phases, respectively. If we substitute Eqs. 4.2 - 4.9 into Eq. 4.1, common terms ($B_1^{\pm} = |B_1^{\pm}|e^{i\phi^{\pm}}$) will cancel, and the final equation can be written as

$$\mathbf{\Omega}^{\pm}\cdot\nabla \ln(\gamma) + \left(\left(\left(\frac{\partial}{\partial x}\phi^{\pm}\right)^2 + \left(\frac{\partial}{\partial y}\phi^{\pm}\right)^2 + \left(\frac{\partial}{\partial z}\phi^{\pm}\right)^2\right) - i\nabla^2\phi^{\pm}\right) + i\omega\mu_0\gamma = 0 \tag{4.10}$$

where

$$\mathbf{\Omega}^{\pm} = \begin{bmatrix} \Omega_x^{\pm} \\ \Omega_y^{\pm} \\ \Omega_z^{\pm} \end{bmatrix} = \begin{bmatrix} i\frac{\partial}{\partial x}\phi^{\pm} \pm \frac{\partial}{\partial y}\phi^{\pm} \\ \mp\frac{\partial}{\partial x}\phi^{\pm} + i\frac{\partial}{\partial y}\phi^{\pm} \\ i\frac{\partial}{\partial z}\phi^{\pm} \end{bmatrix} + \frac{1}{B_1^{\pm}}\begin{bmatrix} \frac{1}{2}\frac{\partial B_z}{\partial z} \\ \pm i\frac{1}{2}\frac{\partial B_z}{\partial z} \\ -\frac{1}{2}\frac{\partial B_z}{\partial x} \mp i\frac{1}{2}\frac{\partial B_z}{\partial y} \end{bmatrix}$$

Eq. 4.10 is the transmit (or receive) phase based EPT formula. There are several issues with using Eq. 4.10. First, since B_z cannot be measured via MRI, B_z related terms in Eq. 4.10 cannot be found. Instead, the following assumption can be made in the ROI: The first derivatives of B_z with respect to each spatial component (x, y, and z) are negligible when compared to $B_1^{\pm}$. This also implies that the second term (or B_z term) of $\mathbf{\Omega}^{\pm}$, $\left(\frac{1}{B_1^{\pm}}\begin{bmatrix} \frac{1}{2}\frac{\partial B_z}{\partial z} \\ \pm i\frac{1}{2}\frac{\partial B_z}{\partial z} \\ -\frac{1}{2}\frac{\partial B_z}{\partial x} \mp i\frac{1}{2}\frac{\partial B_z}{\partial y} \end{bmatrix}\right)$, will be small compared to first term (or phase term) of $\mathbf{\Omega}^{\pm}$, $\left(\begin{bmatrix} i\frac{\partial \phi^{\pm}}{\partial x} \pm \frac{\partial \phi^{\pm}}{\partial y} \\ \mp\frac{\partial \phi^{\pm}}{\partial x} + i\frac{\partial \phi^{\pm}}{\partial y} \\ +i\frac{\partial \phi^{\pm}}{\partial z} \end{bmatrix}\right)$, and therefore B_z term may be neglected. Second, to find EPs in Eq. 4.10, at least one of the transmit and receive phases must be known but in MRI we can only measure the transcieve phase ($\phi^{tr} = \phi^+ + \phi^-$). To write the equation in terms of ϕ^{tr}, we sum the transmit and receive phase based formulas (Eq.4.10), and obtain

$$\begin{bmatrix} \left(i\frac{\partial}{\partial x}\phi^{tr} + \frac{\partial}{\partial y}\left(\phi^+ - \phi^-\right)\right) \\ \left(\frac{\partial}{\partial x}\left(-\phi^+ + \phi^-\right) + i\frac{\partial}{\partial y}\phi^{tr}\right) \\ i\frac{\partial}{\partial z}\phi^{tr} \end{bmatrix} \cdot \begin{bmatrix} \frac{\partial ln(\gamma)}{\partial x} \\ \frac{\partial ln(\gamma)}{\partial y} \\ \frac{\partial ln(\gamma)}{\partial z} \end{bmatrix} + \left(k_{real} - i\nabla^2\phi^{tr}\right) + i2\omega\mu_0\gamma = 0 \tag{4.11}$$

where

$$k_{real} = \left(\frac{\partial}{\partial x}\phi^{tr}\right)^2 + \left(\frac{\partial}{\partial y}\phi^{tr}\right)^2 + \left(\frac{\partial}{\partial z}\phi^{tr}\right)^2 - 2\left(\frac{\partial}{\partial x}\phi^{-}\frac{\partial}{\partial x}\phi^{+} + \frac{\partial}{\partial y}\phi^{-}\frac{\partial}{\partial y}\phi^{+} + \frac{\partial}{\partial z}\phi^{-}\frac{\partial}{\partial z}\phi^{+}\right)$$

In Eq. 4.11, the conductivity (σ) is related with the imaginary terms which also includes the measurable transcieve phase, ϕ^{tr}. Writing only imaginary terms and assuming $\sigma^2 >> (\omega\epsilon)^2$ yields the central equation of this study (please refer to the Appendix for the complete derivation)

$$\left(\nabla\phi^{tr} \cdot \nabla\rho\right) + \nabla^2\phi^{tr}\rho - 2\omega\mu_0 = 0 \tag{4.12}$$

where $\rho = 1/\sigma$ (resistivity).

Equation 4.12 is the governing equation of the generalized phase based electrical conductivity imaging approach. In the next section, the diffusion term will be added to this equation for the purpose of stabilization. Similar to the cr-MREPT approaches Equation 4.12 is also in the form of convection-reaction equation but the coefficients are solely based on the measurable MR transcieve phase. Therefore, no B_1 mapping is required and it is valid for any transmit and receive coil combination (TPA-free). Since the equation includes the gradient of EPs, it also provides boundary-artifact free reconstruction. Additionally, if $\nabla\rho$ is assumed to be zero, Eq. 4.12 reduces to the conventional phase based EPT approach [50], which was explained in section 2.2. To obtain Eq. 4.12, following assumptions have been made: (i) $\sigma^2 >> (\omega\epsilon)^2$. (ii) $|\nabla B_1^+| = 0$ and $|\nabla B_1^-| = 0$. and (iii) B_z terms are neglected. Although the same assumptions were made by the conventional phase based EPT method, rigorous analysis has been given to investigate the effect of these assumption on the reconstructed conductivity images of the proposed method in Section 4.4.

4.2 Methods

4.2.1 Solution of the Central Equation

Eq. 4.12 is solved for ρ using 3D finite difference method. This is also another advantage of the method when compared to cr-MREPT methods because since the measured transcieve phase on Cartesian grid, we do not have to generate a grid (or any mesh elements) for the ROI. Therefore, we can directly represent the partial derivatives in Eq. 4.12 using the central finite difference approximations. For $(N \times M \times L)$ image matrix, the finite difference formulation of Eq. 4.12 at a grid point $(x_i,\, y_j,\, z_k)$ can be expressed as

$$\begin{aligned}&\left(\left(\frac{\rho_{i+1,j,k}-\rho_{i-1,j,k}}{2\Delta y}\right)\cdot\frac{\partial\phi^{tr}}{\partial y}\right)+\left(\left(\frac{\rho_{i,j+1,k}-\rho_{i,j-1,k}}{2\Delta x}\right)\cdot\frac{\partial\phi^{tr}}{\partial x}\right)+\\&\left(\left(\frac{\rho_{i,j,k+1}-\rho_{i,j,k-1}}{2\Delta z}\right)\cdot\frac{\partial\phi^{tr}}{\partial z}\right)+\rho_{i,j,k}\left(\frac{\partial^2\phi^{tr}}{\partial x^2}+\frac{\partial^2\phi^{tr}}{\partial y^2}+\frac{\partial^2\phi^{tr}}{\partial z^2}\right)=2\omega\mu_0\end{aligned} \tag{4.13}$$

where $i = 1, 2 \cdots N$, $j = 1, 2 \cdots M$, $k = 1, 2 \cdots L$, and Δx, Δy, and Δz are the spatial resolutions in each spatial direction, respectively. In Eq. 4.13, the known quantities are the first and the second derivatives of ϕ^{tr} and the unknowns are the ρ values.

Prior to the reconstruction, the region of interest (ROI) is chosen and the finite difference formulation is made in the selected ROI. Assume that the selected region has T spatial grid points, in which B number of points are the boundary nodes, and $P = T - B$ number of points are the inner nodes. Eq. 4.13 is written for all these P number of nodes and is transformed into $Ax = b$ form as follows:

$$\begin{bmatrix} a_{11} & \cdots & a_{1B} & \cdots & a_{1T} \\ \vdots & \cdots & \vdots & \cdots & \vdots \\ a_{B1} & \cdots & a_{BB} & \cdots & a_{BT} \\ \vdots & \cdots & \vdots & \cdots & \vdots \\ a_{T1} & \cdots & a_{TB} & \cdots & a_{TT} \end{bmatrix} \begin{bmatrix} \rho_1 \\ \vdots \\ \rho_B \\ \vdots \\ \rho_T \end{bmatrix} = \begin{bmatrix} 2\omega\mu_0 \\ \vdots \\ 2\omega\mu_0 \\ \vdots \\ 2\omega\mu_0 \end{bmatrix} \tag{4.14}$$

where ρ_1, ρ_2, $\cdots$, ρ_B are the resistivity values on the boundary and ρ_{B+1}, ρ_{B+2}, $\cdots$, ρ_T are the inner unknown resistivity values. Applying Dirichlet boundary condition, columns and rows of A matrix, which corresponds to the boundary nodes, are eliminated from the matrix equation, and the resulting matrix, $A_{p\times p}$, is used to solve the ρ_{B+2}, $\cdots$, ρ_T values.

As previously mentioned, Eq. 4.12 is in the form of convection-reaction-diffusion equation with null diffusion term. $(\nabla\phi^{tr}\cdot\nabla\rho)$ is the convection term, $(\nabla^2\phi^{tr}\rho-2\omega\mu_0)$ is the reaction term, and there is no diffusion term. It has been shown in [65, 66] that if the convection term dominates the diffusion term, it is expected to have unwanted spurious oscillations near the interior and boundary layers in the solution of this type of equations. Since the Eq. 4.12 is purely convective, we also expect these oscillations in our solutions. To tackle with this issue, artificial diffusion term is added to the Eq. 4.12, which stabilizes the solution without blurring the internal layers significantly. This is one of the mostly used stabilization techniques in these type of problems [65, 66]. After adding the diffusion term, the governing equation of this study becomes

$$-c\nabla^2\rho+\left(\nabla\phi^{tr}\cdot\nabla\rho\right)+\nabla^2\phi^{tr}\rho-2\omega\mu_0=0 \tag{4.15}$$

where c is the constant diffusion term in our case. Similar to the convection and reaction terms, the diffusion term, $-c\nabla^2\rho$, is discretized using finite difference approximation as explained in the beginning of this section. Final matrix equation is solved using MATLAB. Adding a diffusion term significantly improves the condition number of system matrix A. For instance, for the reconstruction shown in Figure 4.6 the condition number of A is found to be 1833 and 154 for the case

of without and with using diffusion term, respectively.

As opposed to $B_1^{\pm}$ cr-MREPT methods, Eq. 4.15 is solved for ρ in 3D. Additionally, if desired it can be reduced to its 2D form when $\frac{\partial \rho}{\partial z}$ or $\frac{\partial \phi^{tr}}{\partial z}$ is negligible in the ROI.

4.2.2 Simulation Methods

Electromagnetic simulations were made using COMSOL Multiphysics 4.2a (COMSOL AB, Stockholm, Sweden), and MATLAB (THe Mathworks, Natick, USA) was used for the reconstruction of conductivity from the either simulated data or the experimental data.

In the simulations, quadrature RF high-pass birdcage coil was modeled and the coil was loaded with the simple phantom model and the human head model, which are shown in Figure 4.1 (a) and (b).

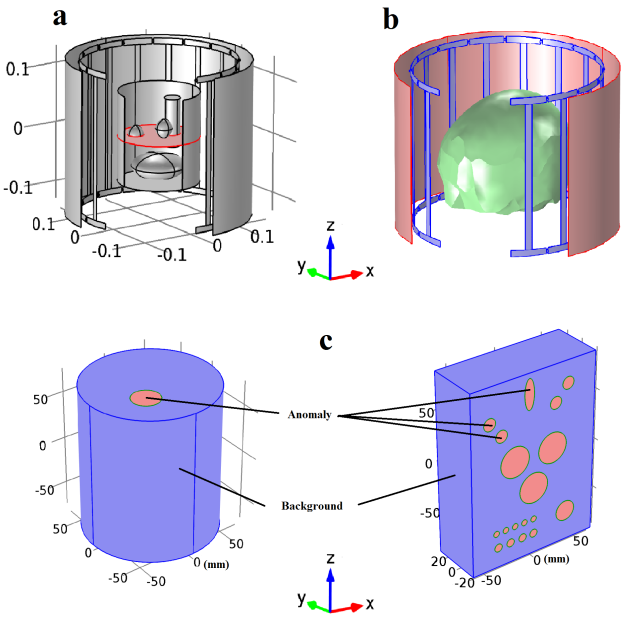

Figure 4.1: Birdcage coil simulation models: (a) loaded with the simple phantom (b) loaded with the head model. Experimental phantom models: (c) with one anomaly (left), and with multiple anomalies (right).

Human Brain Model

Human brain was simply modeled as consisting of five tissues that are scalp, skull, cerebrospinal fluid (CSF), white matter (WM), and grey matter (GM) [67]. For this purpose, we have first obtained volumetric segmented MRI images ($215 \times 180 \times 70,\ 1 \times 1 \times 2.5\ mm^3$) from [68,69]. This segmented data set consists of eleven different tissues but for the simplicity, we have merged and formed them as the aforementioned five tissues. Then, a mesh generation toolbox, which is called iso2mesh [70], was used to mesh the volumetric segmented MRI images so that we could export the meshed geometry to COMSOL Multiphysics where EM simulations were performed. Finally, electrical properties were assigned to these segmented images, and they were interpolated in COMSOL Multiphysics during the simulations. EPs for these brain tissues are given in Table 4.1, and also the EP distributions are illustrated in Figure 4.2.

Table 4.1: EPs of the tissues of human brain model

	128 MHz (3T)		**300 MHz (7T)**	
Tissue	σ (S/m)	ϵ_r	σ (S/m)	ϵ_r
CSF	2.14	84	2.22	73
WM	0.34	52	0.41	44
GM	0.59	73	0.69	60
Skull	0.12	21	0.14	18
Scalp	0.54	62	0.64	50

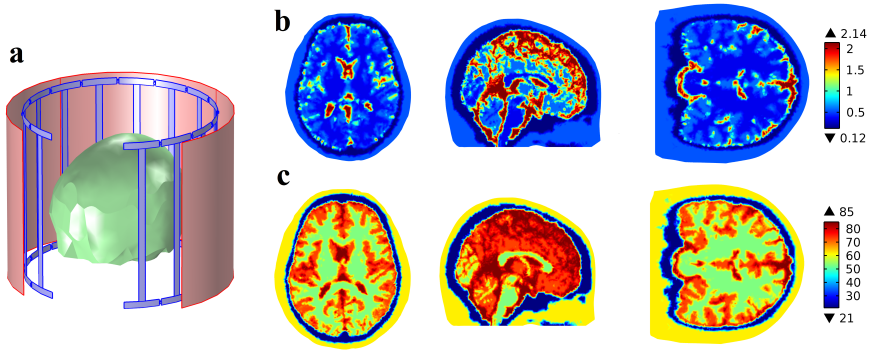

Figure 4.2: (a) Birdcage coil model loaded with the human brain model (b) Conductivity distribution at a central slice of each orientation (S/m) (c) Relative dielectric permittivity distribution at a central slice of each orientation.

The simulations were made at 128 MHz (3T) with a mesh size of $2 \times 2 \times$

$2 \times \ mm^3$. The conductivity maps were calculated using the transcieve phase, which was found by the summation of the transmit and receive phases of the birdcage coil. The results of the proposed method was compared with the results of the conventional phase based EPT method, which uses the formula, $\sigma = \frac{\nabla^2 \phi^{tr}}{2\omega\mu_0}$. The noise was also added to the simulated data. For this purpose, the noise distribution in MRI phase images is assumed to be zero-mean Gaussian with a standard deviation of $1/(\sqrt{2}\ SNR)$ [71, 72] (Here, SNR is the signal to noise ratio in MR magnitude images).

Total relative error in the reconstructed conductivity maps were calculated using L^2 norm as

$$E_\sigma = \sqrt{\frac{\sum_{k=1}^{p}(\sigma_{k,a} - \sigma_k)^2}{\sum_{k=1}^{p}(\sigma_{k,a})^2}} \tag{4.16}$$

where $\sigma_{k,a}$ and σ_k are the actual and the reconstructed conductivity values for the k^{th} node, respectively.

4.2.3 Experimental Methods

Phantom Setup

Two different experimental phantom setups were prepared. One of them has a background and an anomaly region, and we called this phantom as a simple phantom. The other one has multiple anomalies, and it was called as complex phantom. The geometry of these phantoms are illustrated in Figure 4.1 (c). The background regions were made using an agar-saline solution (20 g/L Agar, 2.5 g/L NaCl, 0.2 g/L $CuSO_4$), and the anomaly regions, which have higher conductivity than the background regions, were prepared using a saline solutions (8.8 g/L NaCl, 0.2 g/L $CuSO_4$). The conductivity values of the background and the anomaly regions are expected to be about 0.55 S/m and 1.5 S/m, respectively [73]. A conductivity meter (Hanna Instruments, HI 8733) was also used to measure the

conductivity of the saline solution, and it was found to be 1.53 S/m. The effect of Agar to the conductivity of the background region is assumed to be an additional conductivity of 0.1 S/m [74]. Relative permittivities of both background and the anomaly regions were expected to be 80, which is the same as salt-free water [73].

In vivo Human Experiment

We have also conducted an healthy male volunteer (age 23 years) study with the approval of Institutional Review Board of Bilkent University. Electrical conductivity maps at a sagital slice of the volunteer's brain were calculated using proposed and the conventional method.

Sequence Protocols and Reconstruction

Experiments were conducted on a 3T Magnetom Trio MR Scanner (Siemens, Erlangen, Germany) installed in UMRAM (National Magnetic Resonance Research Center) at Bilkent University. Standard quadrature body coil used for transmit and 12-channel receive only phased array head coil was used for receive operations. Balanced steady state free precession (SSFP) sequence was used to measure the transcieve phase. Detailed sequence parameters were given in Table 4.2 for all experiments.

Table 4.2: Balanced SSFP Sequence parameters for all experiments

Experiment	**Resolution (mm)**	**FOV (mm)**	**FA (deg)**	**TR/TE (ms)**	**NEX**	**Duration (min)**
Simple phantom	1.56 × 1.56 × 5	200 × 200 × 1	60	4.18/2.09	32	∼0.5
Complex phantom	1.56 × 1.56 × 1.56	200 × 200 × 16	40	4.9/2.45	32	∼8.5
Human brain study	1.7 × 1.7 × 1.7	220 × 220 × 190	45	4.42/2.21	10	∼9.5

The sequence, which is used to measure the transcieve phase for the proposed method, must not contain any unrelated phase contributions such as phase due to B_0 inhomogeneities, gradient-induced eddy currents, and motion. Balanced SSFP seems to be one of the most suitable sequences when considering these needs because it has negligible gradient-induced eddy currents and B_0 inhomogeneities. However, the additional phase due to the motion will contribute to the

SSFP phase which could be an issue in the reconstruction of electrical properties. Alternatively, ultrashort TE (UTE) sequence could also be used to measure transcieve phase since it has negligible B_0 inhomogeneities and gradient-induced eddy currents effects. If one uses gradient echo (GRE) sequence, on the other hand, additional scans are supposed to be conducted to remove the phases due to the B_0 inhomogeneities and gradient-induced eddy currents. Similarly, for the spin echo, to remove the gradient-induced eddy currents an additional scan is necessary. Therefore, we have chosen balanced SSFP sequence to measure the transcieve phase.

Prior to the reconstruction, Hamming window was applied to the k-space data to reduce Gibbs ringing artifact in SSFP magnitude and phase images. For noisy simulations and the experiments, the Gaussian filter with a kernel size of $5 \times 5 \times 5$ voxels and a standard deviation of 1.06 in each direction was applied to the transceive phase data. Additionally, median filter with a kernel size of $3 \times 3 \times 3$ voxels was applied to the conductivity maps of the conventional phase based EPT method to obtain smoother reconstruction results [75].

For the boundary condition, all boundary nodes were assigned the same value. This is 1.5 S/m for the simulations and volunteer experiment, and 0.5 S/m for the phantom experiments. For the diffusion coefficient, which is given in Eq. 4.15, different values (from 0.005 to 0.05) were used. The effect of using different diffusion coefficient and also using wrong boundary condition will be investigated in Section 4.4.2.

For the reconstructions, HP Z800 workstation with Intel Zeon X5675 3.07 GHz dual processors (12 cores) and with 64 GB RAM was used. The computation time of 2D reconstruction of the conductivity maps for the 128×128 image matrix was found to be 0.8 seconds. The computation time of 3D human experiment reconstructions was found to be 67 seconds for the $128 \times 128 \times 9$ image matrix.

4.3 Results

4.3.1 Simulation Results

Figure 4.3 shows the conductivity maps at a transverse slice of the simulation phantom (described in 4.1 (a)) obtained using both the conventional phase based EPT method and the proposed method for different SNR values. Selection of the ROI is shown in 4.3 (a). It can be seen that the conventional method reconstructs the conductivity successfully in the regions where the EPs have uniform distribution, but it has boundary artifact in the transition regions (shown with the red arrows in Figure 4.3 (b)). The artifact becomes wider in the noisy simulations since the Gaussian filter is applied. The proposed method, on the other hand, reconstructs the conductivity distribution accurately in the whole ROI including the transition regions (second row of Figure 2b). It has no boundary or LCF artifact in the reconstructed conductivity maps. The superiority of the proposed method over the conventional method can be better seen in the conductivity profiles, which are shown in 4.3 (c). The effect of using different diffusion coefficients is also more apparent in this figure. As can be seen, using smaller diffusion coefficient allows for the calculation of the conductivity more accurately but in a less stable manner. Therefore, there is a trade-off between the accurateness and the stabilization of the solutions, which needs to be taken into consideration in choosing diffusion coefficient.

Figure 4.4 shows the reconstructed conductivity maps for the human head simulation. The ROI is selected at a transverse slice, and the actual conductivity at the ROI is shown in Figure 4.4 (a). Similar to the phantom simulation, the conventional and the proposed methods were analyzed under different SNR values. Conductivity value at the boundary nodes was taken as 1.5 S/m, and diffusion constant, c, was taken as 0.005, for the solution of the proposed method. In the results of the conventional method, dark regions, which are shown with the red arrow in Figure 4.4 (b), are the boundary artifacts. These regions are successfully reconstructed in the proposed method. Figure 4.4 (c) shows the conductivity profiles of both methods for different lines in the ROI. For all lines, the conductivity

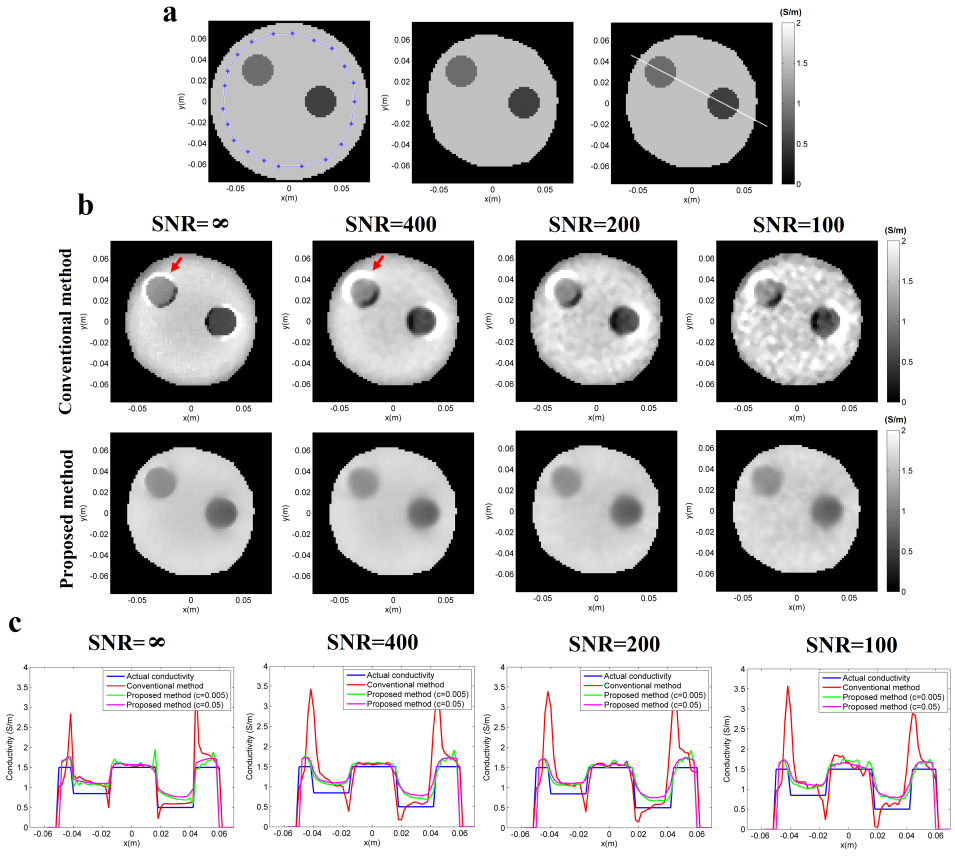

Figure 4.3: (a) Selection of the ROI indicated by the blue polygon (left), the actual conductivity map in the ROI (middle), illustration of the line where the conductivity profiles are plotted (right) (b) Reconstructed conductivity maps using the conventional phase based EPT method and the proposed method for different SNR values. (c) Conductivity profiles of the conventional method and the proposed method (along the dotted line given in (a)) for different diffusion coefficients under different SNR values.

profiles of the proposed method are well consistent with the actual conductivity maps.

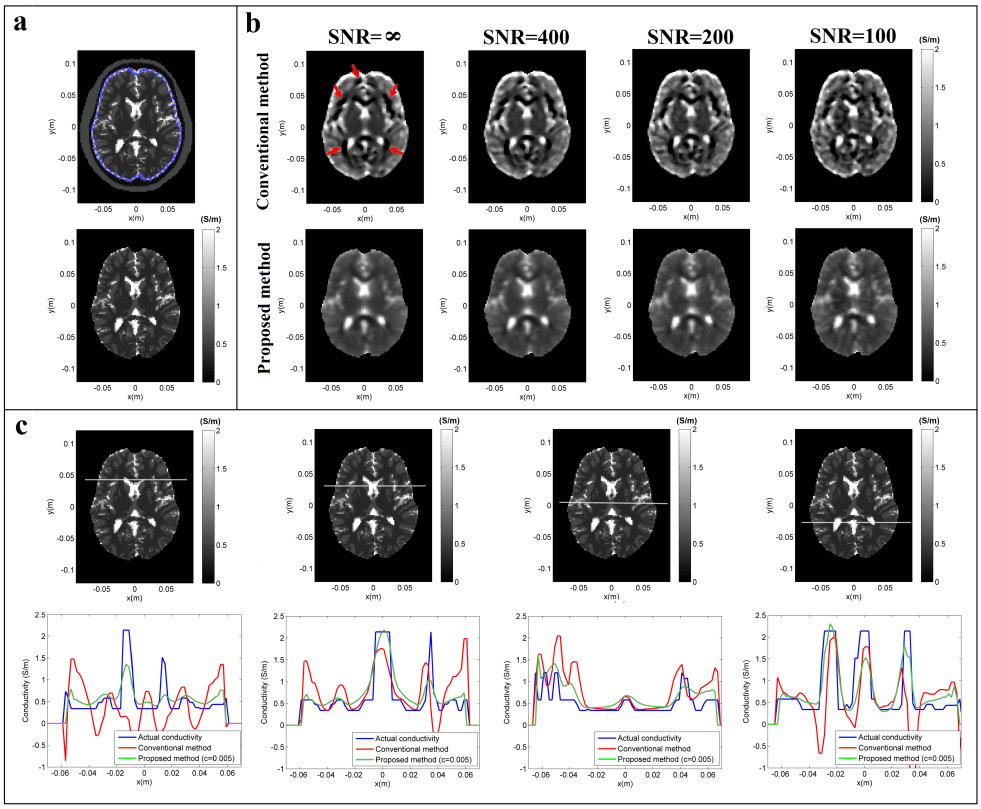

Figure 4.4: Human head model simulations. (a) Selection of the ROI indicated by the blue polygon (left), the actual conductivity map in the ROI (right) (b) Reconstructed conductivity maps using the conventional phase based EPT method and the proposed method for different SNR values (c) Conductivity profiles of the conventional method and the proposed method along the lines which are shown above each profile plot (when the SNR=∞).

Total relative errors in the reconstructed conductivity maps of both methods are given in Table 4.3. In both methods, errors in the human head simulations is higher than the errors in the phantom simulation. For the conventional method, the main reason is that the complexity of the structure. The more complex structures we have in the region of interest, the more boundary artifacts occur in the conventional method, which results a significant error in the reconstructed conductivity maps. In the proposed method, on the other hands, the main source of error is the violation of the assumptions made in the derivation of the governing

equation. These assumptions will be investigated in detail in Section 4.4. Moreover, the error in the proposed method is still acceptable when compared to the conventional method.

Table 4.3: Total relative error of the conventional and the proposed method

	SNR=∞		**SNR=400**		**SNR=200**		**SNR=100**	
Simulation	**CM**	**PM**	**CM**	**PM**	**CM**	**PM**	**CM**	**PM**
Phantom	8.92%	**2.18%**	9.77%	**2.23%**	10.1%	**2.31%**	10.5%	**2.47%**
Human head	73.71%	**16.36%**	74%	**16.4%**	74.69%	**16.65%**	76.78%	**17.47%**

4.3.2 Experimental Results

Figure 4.5 shows the results of the simple phantom, which has one anomaly (described in 4.1 c), for one of the channels in the selected ROI. SSFP magnitude and transceive phase images at the transverse slice are given in Figure 4.5 (a) and (b), respectively. SNR was calculated using two repeated acquisitions [76] and was found to be about 125 for the background, and 220 for the anomaly region. Prior to the reconstruction, the same Gaussian filter, used in the noisy simulations, was applied to the SSFP transceive phase images. For the proposed method, conductivity value at the boundary nodes was taken as 0.5 S/m, and diffusion constant, c, was taken as 0.05. The reconstructed conductivity maps of both methods are illustrated in Figure 4.5 (c) and (d). For the proposed method, the conductivity values in the anomaly region and the background region are found to be 1.93 $\pm$ 0.07 S/m and 0.6 $\pm$ 0.01 S/m, respectively. For the conventional method, the conductivity values are found to be 2.07 $\pm$ 0.07 S/m and 0.59 $\pm$ 0.09 S/m. Transition regions, where the boundary artifact occurs in the results of the conventional method, were successfully reconstructed in the proposed method.

Figure 4.6 shows the results of the complex phantom, which has multiple anomalies (described in 4.1 c), and which was scanned in 3D coronal orientation. SSFP magnitude image in the whole FOV is given in 4.6 (a). Here, banding artifacts, which can occur in SSFP sequences, are observed, and they are shown with the red arrows. Fixing this banding artifact issue is beyond the scope of this dissertation (interested readers are referred to [77]), therefore the ROI was selected as shown in 4.6 (a). SSFP magnitude and phase images in this ROI are

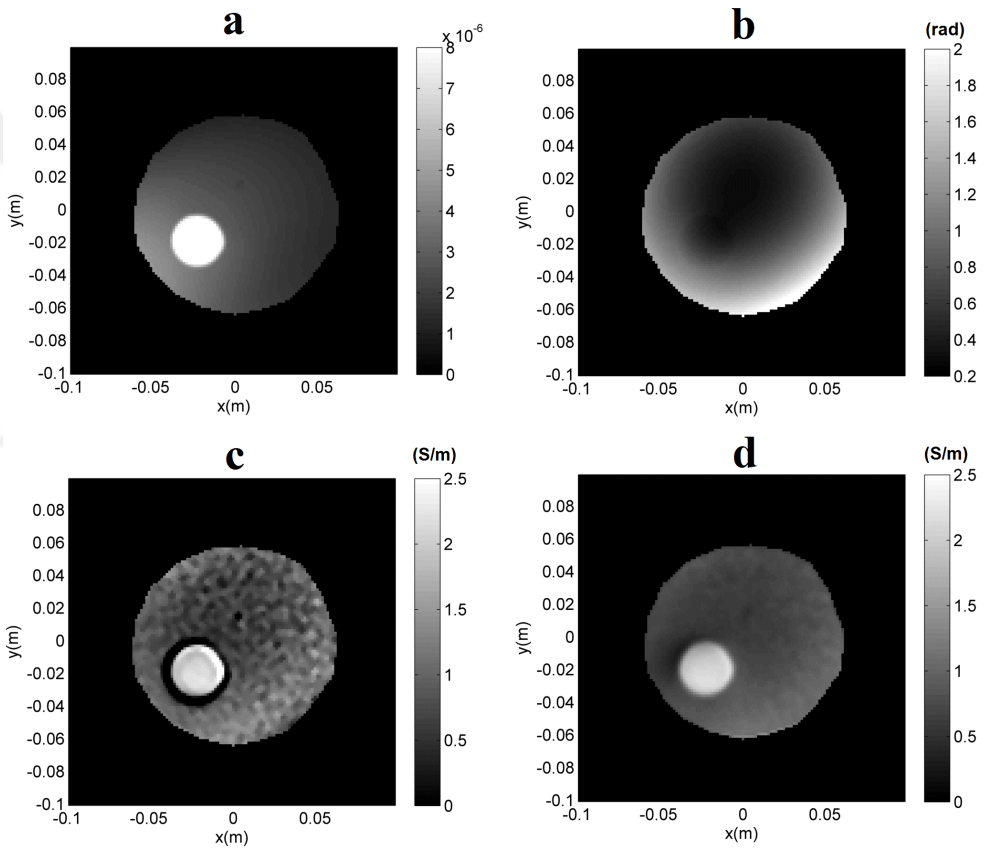

Figure 4.5: Magnitude, phase, and reconstructed conductivity images of the first experimental phantom for one of the channels in the ROI. (a) SSFP Magnitude image (b) SSFP Transceive phase (c) Conductivity map reconstructed using the conventional method (d) Conductivity map reconstructed using the proposed method.

illustrated in Figure 4.6 (b) and (c), respectively. As can be seen in 4.6 (b), sensitivity of this channel (or coil) drops while moving from lower right corner to upper left corner. For the more sensitive sides, SNR was calculated to be about 200 for the anomaly region and 100 for the background region. For the less sensitive sides, SNR was calculated to be about 90 for the anomaly region and 50 for the background region. The same Gaussian filter, boundary condition, and diffusion constant, which were used in the previous phantom experiment, were used. 4.6 (d) and (e) show the reconstructed conductivity maps of the conventional and the proposed methods. For the proposed method, the conductivity values in the anomaly region and the background region are found to be 1.48 ± 0.03 S/m and 0.68 ± 0.01 S/m, respectively. For the conventional method, the conductivity values are found to be 1.58 ± 0.07 S/m and 0.65 ± 0.06 S/m. These values are calculated in the high SNR regions. These results show that the proposed method is also capable of reconstructing the transition regions in a complex structured phantom which has small anomaly regions (with radii of less than 1 cm).

Figure 4.7 shows in vivo results at a sagittal slice of the volunteer brain. Multichannel combined SSFP magnitude image, and the selection of the ROI is given Figure 4.7 (a). SSFP magnitude and phase images for one of the channels in the selected ROI are depicted in Figure 4.7 (b) and (c). The high contrast regions in the magnitude image correspond to the CSF in the brain. SNR in the CSF regions was found to be 400, and for non-CSF regions it was found to be 90. Figure 4.7 (d) and (e) show the results of the conductivity maps of the conventional method and the proposed method (using 3D formulation), respectively. 3D region was selected by taking four slices above and below of that sagittal slice, and final matrix ($128 \times 128 \times 9$) was used to solve the conductivity. In the results of the conventional method, dark regions that have negative conductivity values are the boundary artifacts, and it is difficult to interpret this image for any clinical purposes. With the proposed method (c=0.05), on the other hand, boundary artifacts were eliminated and the contrast variations in the conductivity maps of the proposed method is very similar to the contrast variations seen in the magnitude image. The average conductivity values of the CSF regions in the red dotted circles (see Figure 4.7 (b) and (e)) are found to be 2.08 ± 0.3 S/m,

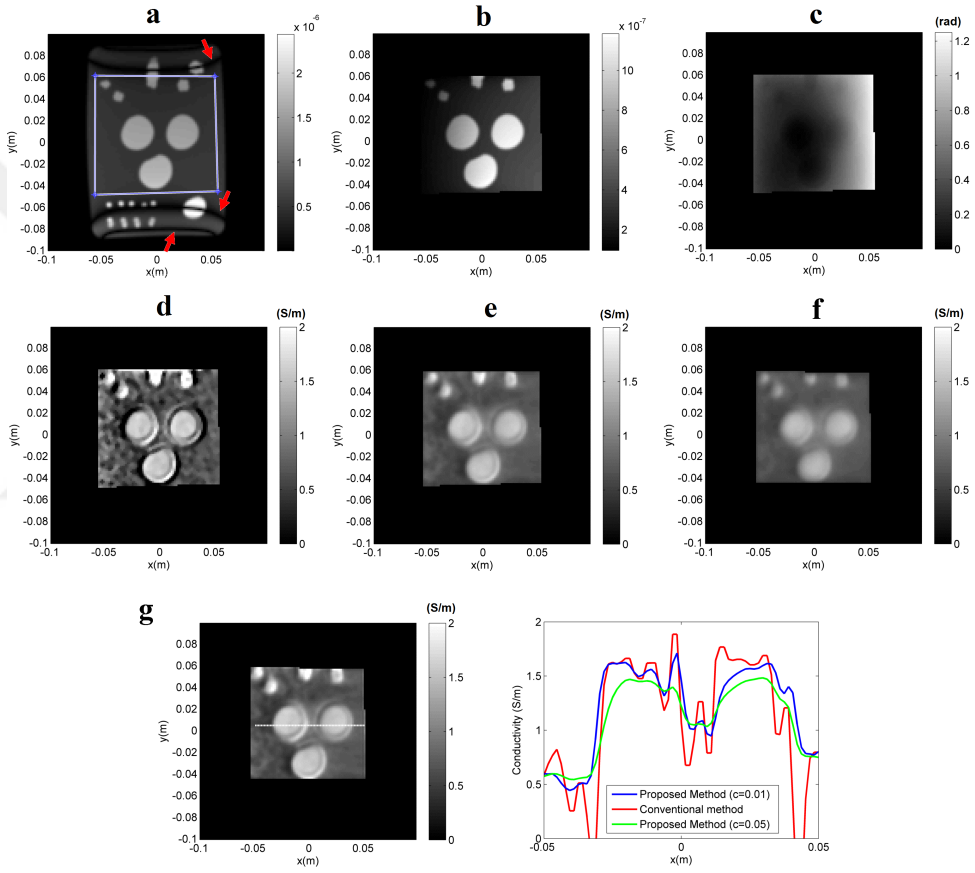

Figure 4.6: Magnitude, phase, and reconstructed conductivity images of the second experimental phantom for one of the channels. (a) Selection of the ROI indicated by the blue polygon (b) SSFP Magnitude image (c) SSFP Transceive phase (d) Conductivity map using the conventional method (e) Conductivity map using the proposed method (c=0.01) (f) Conductivity map using the proposed method (c=0.05) (g) Conductivity profiles of the conventional and the proposed method given in (d)-(f).

1.4 ± 0.09 S/m, and 1.66 ± 0.04 S/m, from upper to lower side. The average conductivity value of the grey matter (which mainly lies adjacent to the CSF regions in Figure 4.7 (d)) is found to be 0.76 ± 0.03 S/m, and for the white matter (calculated in the central region in Figure 4.7 (d)) the conductivity value is found to be 0.53 ± 0.06 S/m. For the low conductive regions, i.e. grey matter and the white matter, conductivity values are overestimated similar to the simulation results due to the violation of the assumptions but in overall, the results of the proposed method are well consistent with the literature values [2].

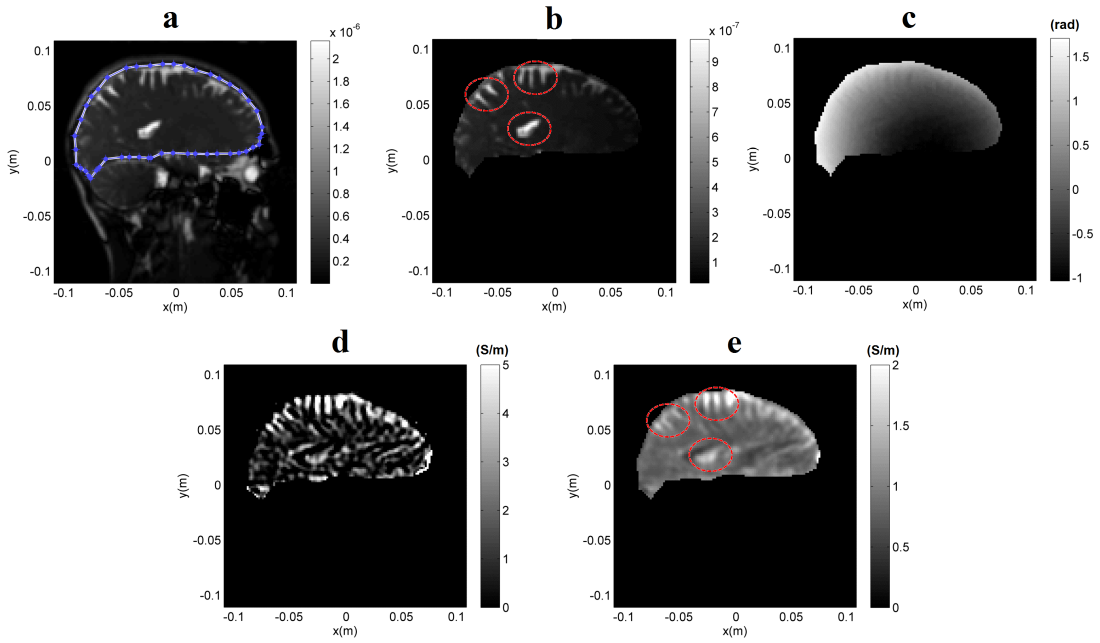

Figure 4.7: Magnitude, phase, and reconstructed conductivity images of human brain for one of the channels at the ROI. (a) Selection of the ROI indicated by the blue polygon (b) SSFP Magnitude image (c) SSFP Transceive phase (d) Conductivity map reconstructed using the conventional method (e) Conductivity map reconstructed using the 3D formulation of the proposed method.

4.4 Theoretical Investigation of the Proposed Method

In this section, assumptions which are made in the formulation of the proposed method, diffusion term which is used in the calculations, and the concept of boundary condition will be investigated in detail. For this purpose, various scenarios will be studied for different phantoms and human brain model in COMSOL Multiphysics, and we will observe the conditions under which the assumptions start to fail, and also the effects of violating an assumption on the reconstructed conductivity maps. In the simulations, parameters such as field strength, electrical properties, and coil type will be altered to break the assumptions, and the resulting conductivity images will be analyzed. Additionally, the effects of using different diffusion coefficients and using wrong boundary conditions on the reconstructed conductivity maps will be examined in the separate subsections.

4.4.1 Assumptions

As explained in the Section 4.1, following assumptions have been made in the formulation of the governing equation of the proposed method:

- $\sigma^2 >> (\omega\epsilon)^2$.
- $\nabla|B_1^{\pm}| = 0$.
- B_z term in Eq. 4.10 $\left(\frac{1}{B_1^{\pm}}\begin{bmatrix} \frac{1}{2}\frac{\partial B_z}{\partial z} \\ \pm i\frac{1}{2}\frac{\partial B_z}{\partial z} \\ -\frac{1}{2}\frac{\partial B_z}{\partial x} \mp i\frac{1}{2}\frac{\partial B_z}{\partial y} \end{bmatrix}\right)$, which includes the first derivatives of B_z divided by $B_1^{\pm}$, are assumed to be small compared to the phase term $\left(\begin{bmatrix} i\frac{\partial \phi^{\pm}}{\partial x} \pm \frac{\partial \phi^{\pm}}{\partial y} \\ \mp\frac{\partial \phi^{\pm}}{\partial x} + i\frac{\partial \phi^{\pm}}{\partial y} \\ +i\frac{\partial \phi^{\pm}}{\partial z} \end{bmatrix}\right)$ so that it could be neglected.

To investigate each assumption separately, we have first built a noise-free "valid simulation model" in which all of the above assumptions are satisfied. Then, by modifying some parameters in the simulations, we have examined the violation of the assumptions as well as the resulting conductivity images. For this purpose, a head birdcage coil was modeled at $1.5T$ [67] to be used for both transmit and receive operations. The motivation of using this type of coil is that the birdcage coil produces a uniform $B_1^{\pm}$ magnetic field in the ROI especially at lower field strengths. Additionally, B_z term in the above assumption will be small in this type of coil configuration especially at the axial central slice. Therefore, the second and the third assumptions were expected to be satisfied. Figure 4.8 shows this model, simulation phantom, and the actual conductivity map at the central axial slice.

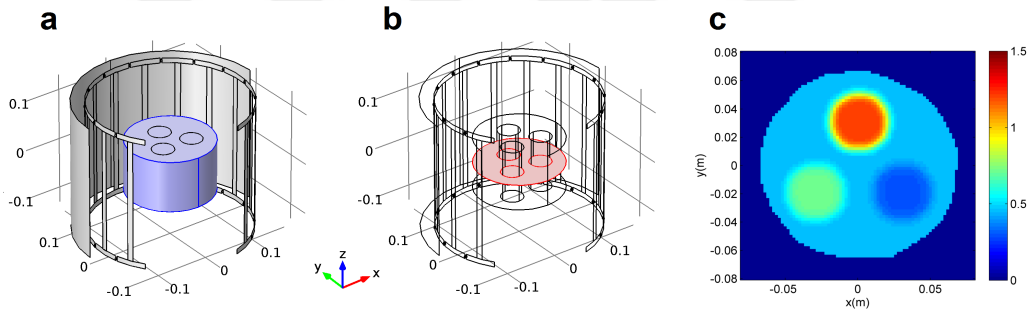

Figure 4.8: (a) Simulation model used for investigating the assumptions. (b) Wire-frame illustration of the model. (c) Actual conductivity distribution in S/m at the central axial slice, which is shown with red in (b).

In this model, the coil was loaded with a four-compartment phantom each of which compartment had different conductivity value (see Figure 4.8 (c)), but the relative dielectric permittivity was the same for all compartments and was taken as 1 (free-space). With this configuration, the first assumption was also satisfied. As shown in 4.8 (c) conductivity transition regions are not sharp rather are slowly varying. Figure 4.9 shows the status of each assumption, and the reconstructed conductivity maps under these conditions.

Figure 4.9 (a)-(f) show the assumption plots. For the first assumption, $\frac{\sigma^2}{(\omega\epsilon)^2}$ was plotted to check the validity of the assumption. For the second assumption, $|\nabla B_1^+|$ and $|\nabla B_1^-|$ were given separately, and for the third assumption,

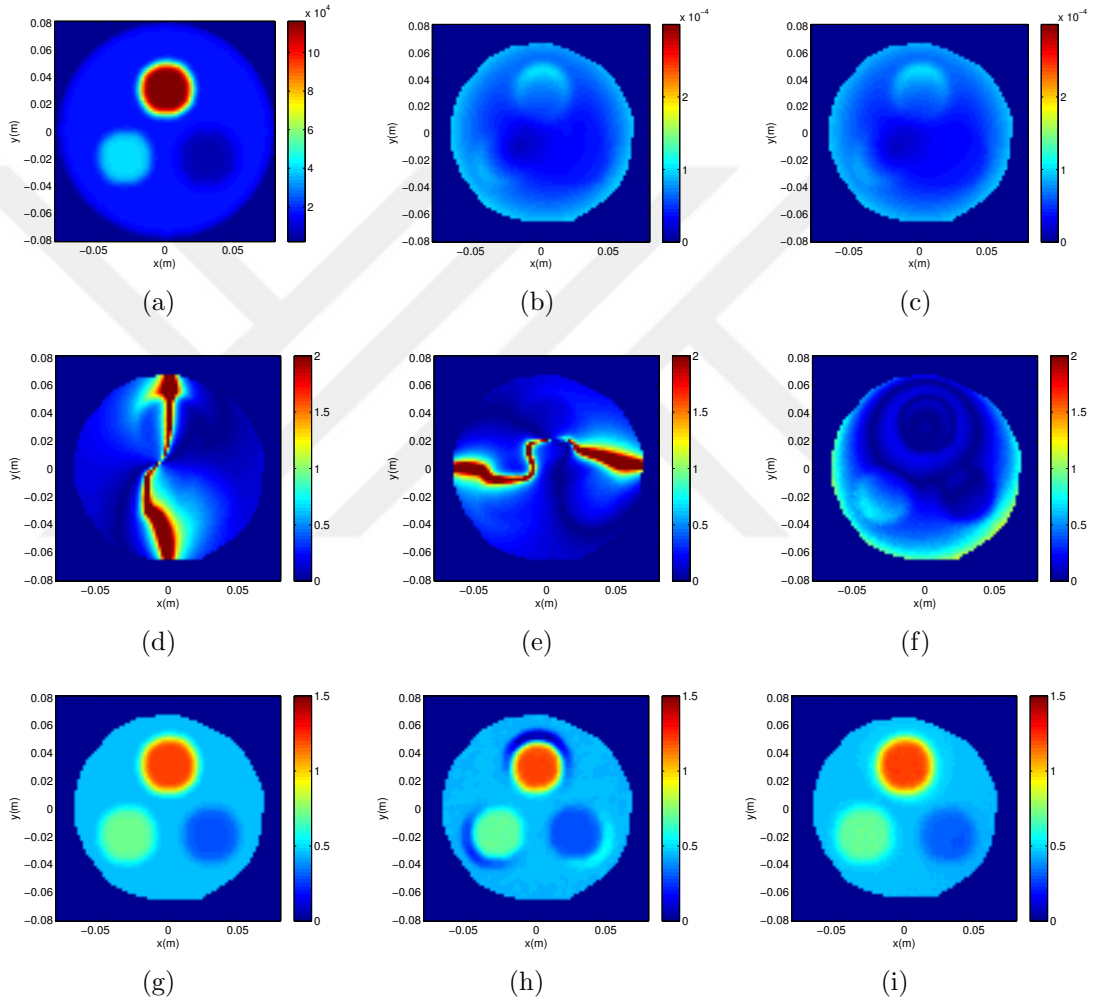

Figure 4.9: Results of the valid model. (a) $\frac{\sigma^2}{(\omega\epsilon)^2}$, (b) $|\nabla B_1^+|$, (c) $|\nabla B_1^-|$, (d-f) imaginary part of each spatial component (x-, y-, and z-) of the B_z terms are divided by the imaginary part of the corresponding component in the phase terms. (g) Actual conductivity (in S/m) (h) Reconstructed conductivity distribution (in S/m) using conventional method (i) Reconstructed conductivity distribution (in S/m) using proposed method at the central axial slice.

the ratio of the each spatial component of B_z term $\left(\frac{1}{B_1^+}\begin{bmatrix}\frac{1}{2}\frac{\partial B_z}{\partial z}\\ i\frac{1}{2}\frac{\partial B_z}{\partial z}\\ -\frac{1}{2}\frac{\partial B_z}{\partial x}-i\frac{1}{2}\frac{\partial B_z}{\partial y}\end{bmatrix}\right)$ to the corresponding phase term $\left(\begin{bmatrix}i\frac{\partial \phi^+}{\partial x}+\frac{\partial \phi^+}{\partial y}\\ -\frac{\partial \phi^+}{\partial x}+i\frac{\partial \phi^+}{\partial y}\\ +i\frac{\partial \phi^+}{\partial z}\end{bmatrix}\right)$ were shown separately. Figure 4.9 (h) and (i) present the conductivity maps which are reconstructed using the conventional and the proposed method, respectively. With these configurations, proposed method finds the conductivity distributions in the ROI with a total average error of 2%. This systematic error could be due to the diffusion used in the calculations, numerical errors, and filter operations. In any case, this error seems to be acceptable for the valid model, and different scenarios can be obtained by manipulating this model. (Boundary artifact issue of the conventional method will not be discussed in this section, since it has already been mentioned in the previous sections. Therefore, the focus will be on the effect of the assumptions on the reconstructed conductivity map.)

For the valid model, the value of the $\frac{\sigma^2}{(\omega\epsilon)^2}$ is found to be grater than 5000 for all compartments (see Figure 4.9 (a)), which implies that the first assumption holds. For the second assumption, $|\nabla B_1^{\pm}|$ was plotted, and for better visualization of this assumption, the maximum value of the colorbar was set to $3\times10^4\ T/m$. This value was taken from the most violated case of the second assumption (Scenario 2, 7T case) in this section. For the third assumption, on the other hand, since the ratio of two terms is plotted, the maximum value of the colorbar is set to 2, which implies that the regions above this value will be saturated, and the third assumption is violated at these regions. For example, x- and y- components of the B_z term in Figure 4.9 (d) and (e) are comparable with the corresponding components of the phase term in some parts (which are saturated in the plot), but their effects in the reconstructed conductivity maps seem to be minimal. The reason is that the violation of the third assumption is only effective in the transition regions. This can be seen in Eq. 4.10 in which the gradient of the electrical properties is multiplied with the summation of the phase term and the B_z term. In the following scenarios, different cases will be investigated by altering

the some parameters of this valid model.

Scenario 1: In this scenario, field strength was increased to $3T$ and $7T$, and the other conditions left unchanged. For this purpose, necessary capacitance value of the head birdcage coil was set to resonance the coil at the Larmor frequency of the desired field strength, and the electromagnetic analyses were performed. Results for the $3T$ and $7T$ cases are shown in Figure 4.10 and 4.11, respectively.

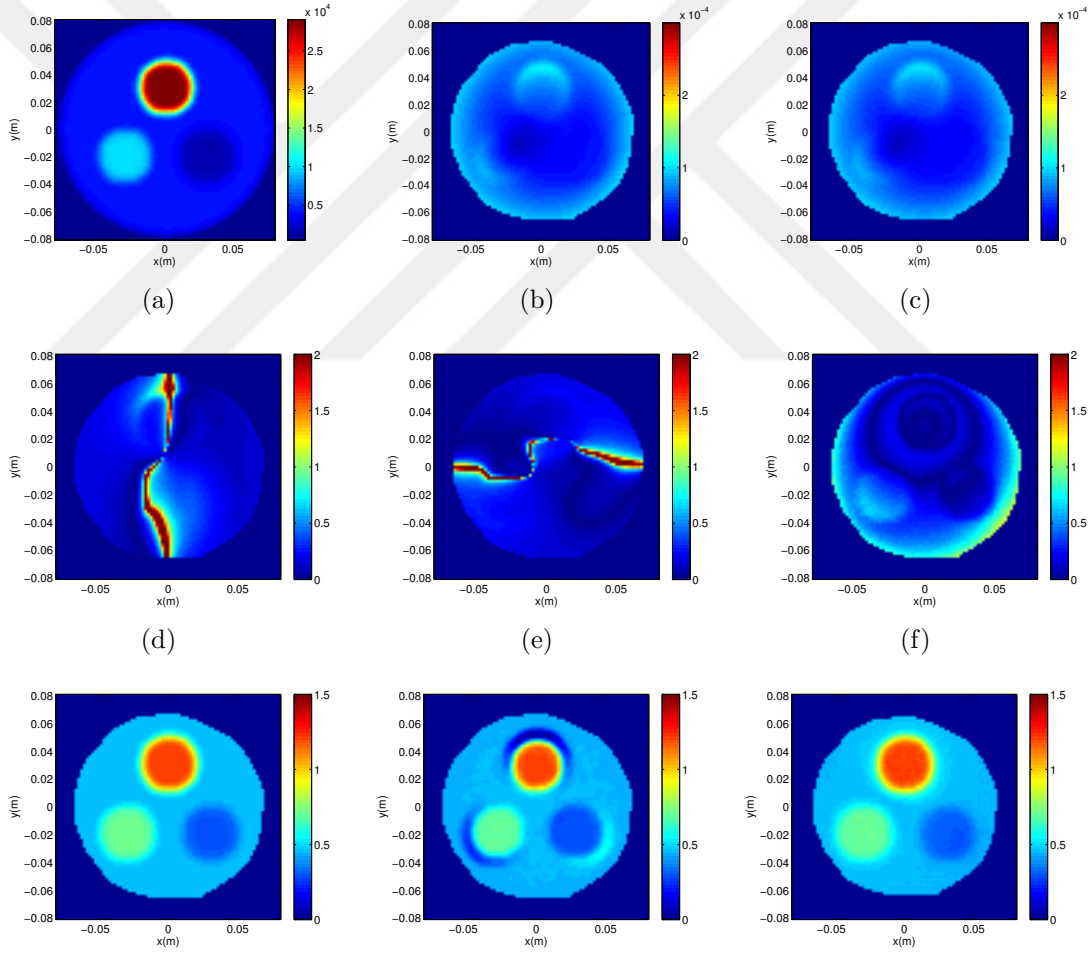

Figure 4.10: Results of the first scenario ($3T$ case). (a) $\frac{\sigma^2}{(\omega\epsilon)^2}$, (b) $|\nabla B_1^+|$, (c) $|\nabla B_1^-|$, (d-f) imaginary part of each spatial component (x-, y-, and z-) of the B_z terms are divided by the imaginary part of the corresponding component in the phase terms. (g) Actual conductivity (in S/m) (h) Reconstructed conductivity distribution (in S/m) using conventional method (i) Reconstructed conductivity distribution (in S/m) using proposed method at the central axial slice.

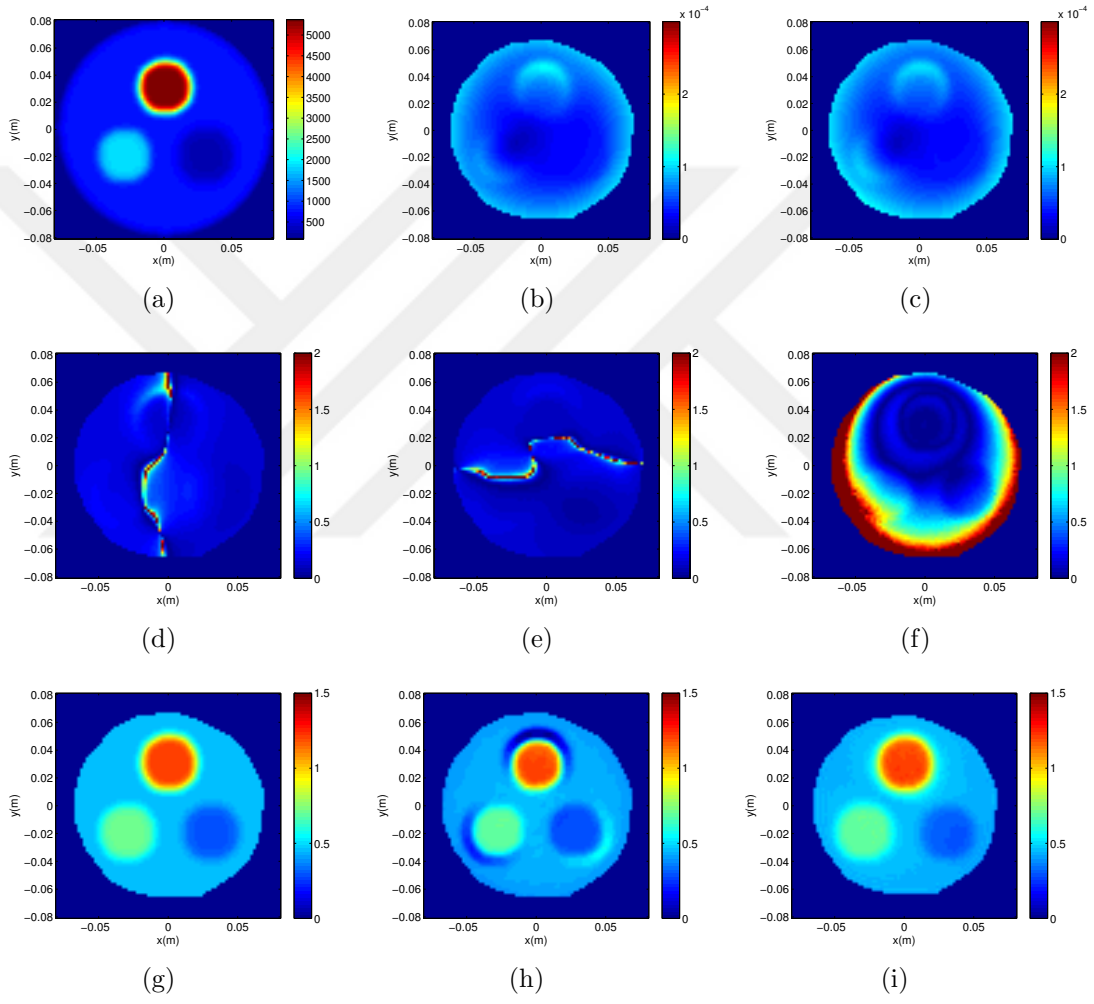

Figure 4.11: Results of the first scenario ($7T$ case). (a) $\frac{\sigma^2}{(\omega\epsilon)^2}$, (b) $|\nabla B_1^+|$, (c) $|\nabla B_1^-|$, (d-f) imaginary part of each spatial component (x-, y-, and z-) of the B_z terms are divided by the imaginary part of the corresponding component in the phase terms. (g) Actual conductivity (in S/m) (h) Reconstructed conductivity distribution (in S/m) using conventional method (i) Reconstructed conductivity distribution (in S/m) using proposed method at the central axial slice.

Since the relative dielectric permittivity is equivalent to the free-space permittivity, even if the field is increased to $3T$ and $7T$, there will be still no wavelength effect, and therefore $|\nabla B_1^{\pm}| = 0$ assumption still holds (see Figure 4.10 (b) and (c) for $3T$ case, and see Figure 4.11 (b) and (c) for $7T$ case). Similarly, the first assumption is also related with the dielectric permittivity, and the value of $\frac{\sigma^2}{(\omega\epsilon)^2}$ is found to be greater than 1500 for 3T case, and grater than 300 for 7T case for all compartments. Therefore the first assumption also holds (see Figure 4.10 (a) and Figure 4.11 (a)). The results of the third assumption, on the other hand, slightly change from the valid case to $7T$ case. In $7T$ case, for example, the saturated line shaped region in which the B_z assumption is not satisfied is smaller than that of the valid case. Furthermore, it can be seen in Figure 4.11 (f) that the z-component of the third assumption started to fail at $7T$ at the periphery of the phantom. This violation slightly decreases the conductivity distribution at that region. This can be seen in the profile plots given in Figure 4.12. Even for this case, conductivity distribution was reconstructed with a total average error of 3% using the proposed method.

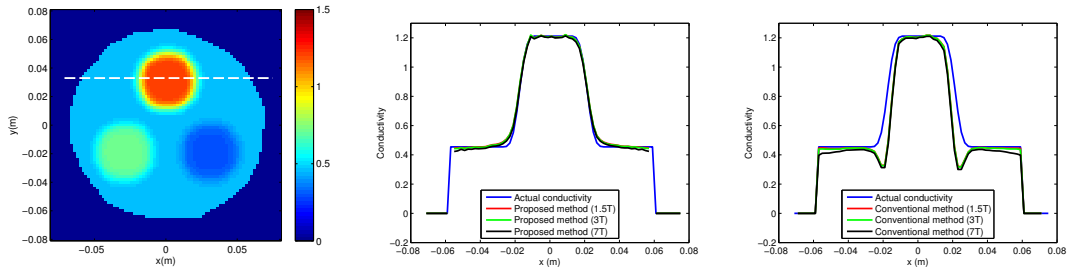

(a) (b) (c)

Figure 4.12: Profile plots for the valid model and scenario 1. (a) Illustration of the line where the conductivity profiles are plotted. (b) Conductivity profiles (in S/m) for the proposed method. (c) Conductivity profiles (in S/m) for the conventional method.

So far unrealistic cases have been examined in the simulation environment. In practice, relative permittivity varies between 10 and 80 in the human tissue at these frequencies. Therefore in the next scenario, this situation will be taken into consideration.

Scenario 2: In this scenario, relative dielectric permittivity of 40 and 80 were assigned to all compartments of the phantom, and the electromagnetic simulations were performed for all three field strengths. Therefore, six different cases were examined in this scenario. Following three figures, Figure 4.13 to Figure 4.15, show the results of the three field strengths ($1.5T$, $3T$, and $7T$), when the relative permittivity is taken as 40.

For the $1.5T$ case (see Figure 4.13), the second and the third assumptions are still satisfied, and for the first assumption, σ^2 starts to be comparable with the $(\omega\epsilon)^2$ in the background and the low conductive region. For example, the value of $\frac{\sigma^2}{(\omega\epsilon)^2}$ is found to be 4.4 and 7.9 in the low conductive and the background region, respectively. For this case, the conductivity distribution was reconstructed with a total average error of 2.6% using the proposed method.

In the $3T$ case (see Figure 4.14), the second assumption starts to be broken at the periphery of the phantom due to the wavelength effect. The first assumption, on the other hand, is now violated in the low conductive and the background region. The value of $\frac{\sigma^2}{(\omega\epsilon)^2}$ is found to be 1.97 and 1.11 in the low conductive and the background region, respectively. For the other two compartments of the phantom, σ^2 is at least six fold greater than the $(\omega\epsilon)^2$. These violations cause an increase in the conductivity value especially at the periphery of the phantom (see Figure 4.14 (h) and (i)). Using the proposed method, conductivity distribution was reconstructed with a total average error of 6.3% for this case.

The results of the $7T$ case can be observed in Figure 4.15. In this case, both the first and the second assumptions are violated almost everywhere in the phantom. For example, the value of $\frac{\sigma^2}{(\omega\epsilon)^2}$ is found to be 3.23, 1.10, 0.36, and 0.20 from high conductive to low conductive region, respectively. Additionally, the violation of the second assumption at the periphery of the phantom can be seen from the saturated plots given in Figure 4.15 (b) and (c). These violations affect the conductivity results of both the conventional and the proposed method significantly which are shown in Figure 4.15 (h) and (i). The increase in the conductivity results of the conventional method is much more than that of the proposed method. The total average error in the results of the proposed method

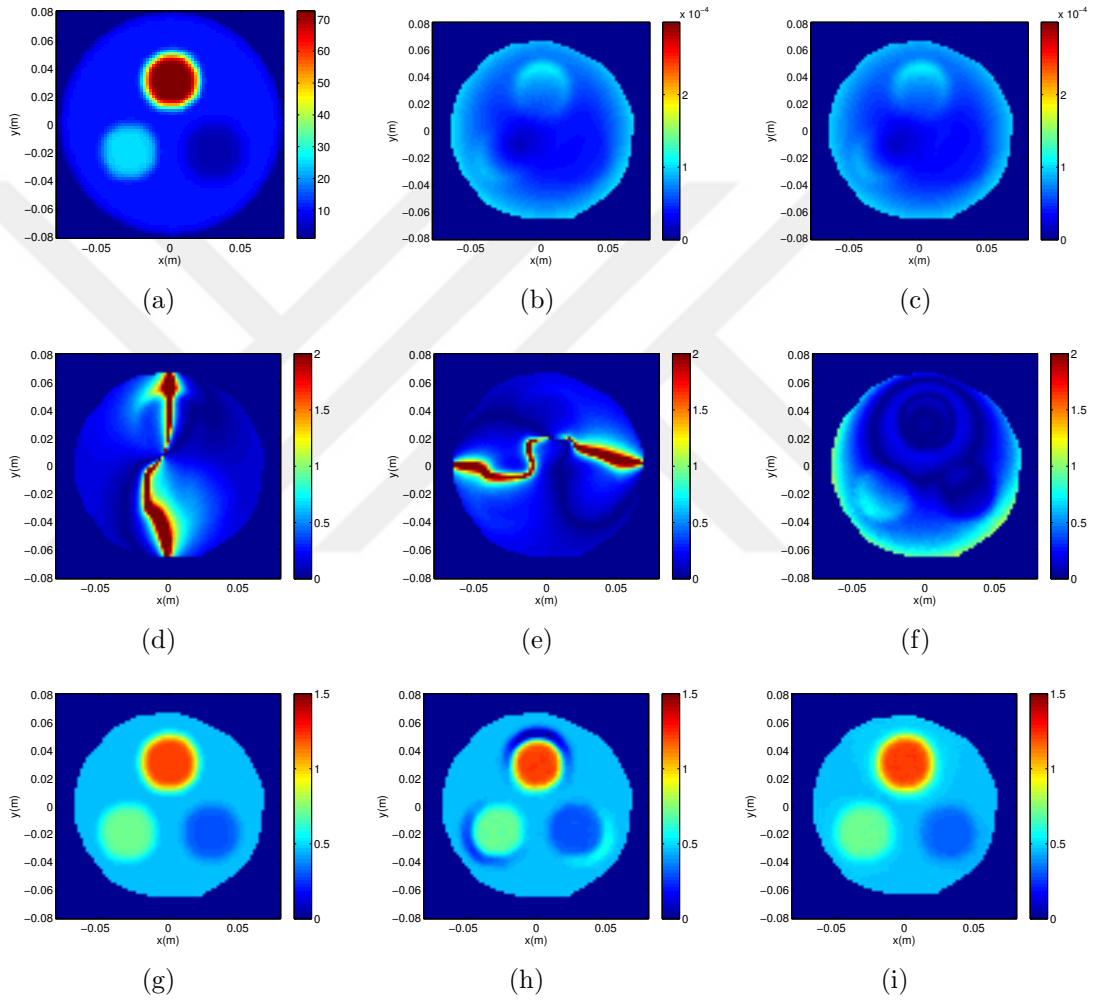

Figure 4.13: Results of the second scenario ($1.5T$ case when $\epsilon_r = 40$).(a) $\frac{\sigma^2}{(\omega\epsilon)^2}$, (b) $|\nabla B_1^+|$, (c) $|\nabla B_1^-|$, (d-f) imaginary part of each spatial component (x-, y-, and z-) of the B_z terms are divided by the imaginary part of the corresponding component in the phase terms. (g) Actual conductivity (in S/m) (h) Reconstructed conductivity distribution (in S/m) using conventional method (i) Reconstructed conductivity distribution (in S/m) using proposed method at the central axial slice.

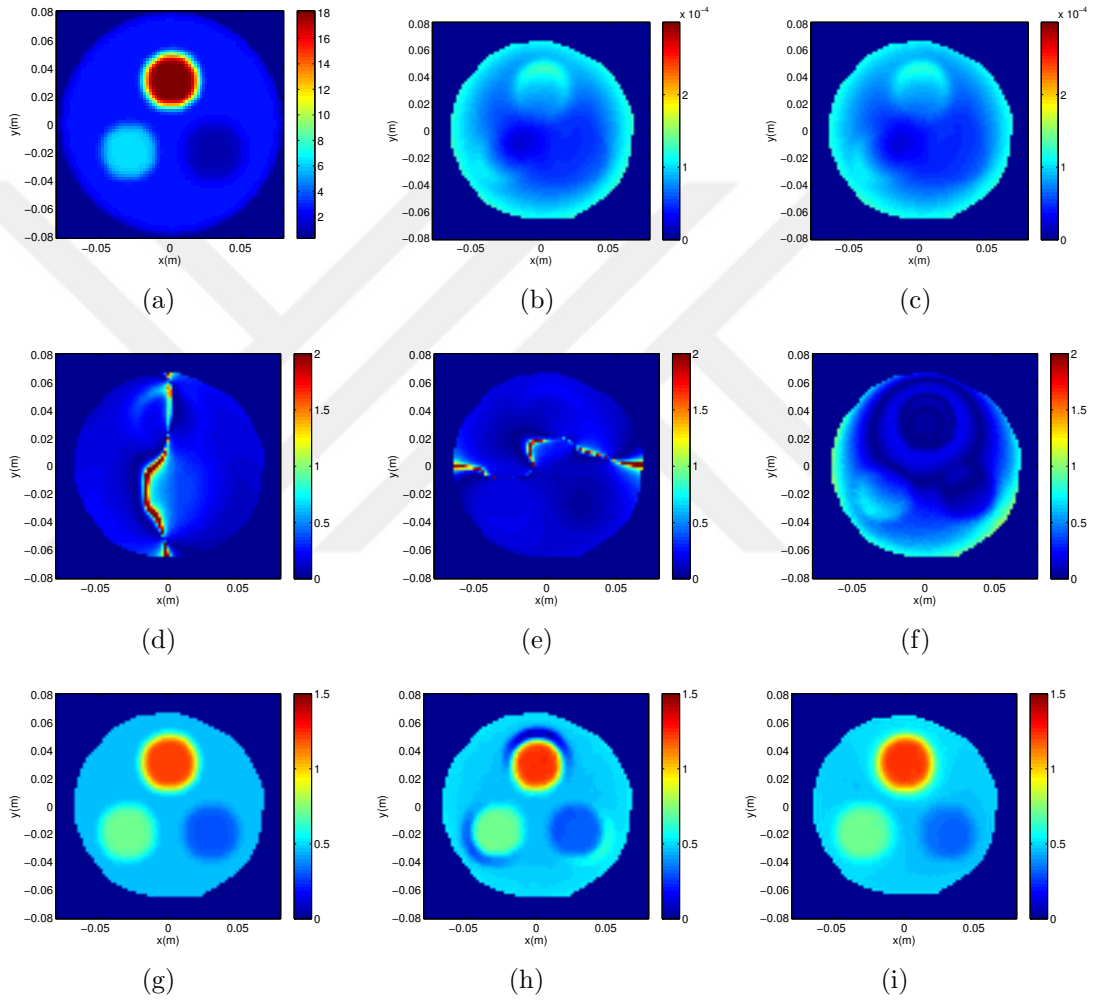

Figure 4.14: Results of the second scenario ($3T$ case when $\epsilon_r = 40$). (a) $\frac{\sigma^2}{(\omega\epsilon)^2}$, (b) $|\nabla B_1^+|$, (c) $|\nabla B_1^-|$, (d-f) imaginary part of each spatial component (x-, y-, and z-) of the B_z terms are divided by the imaginary part of the corresponding component in the phase terms. (g) Actual conductivity (in S/m) (h) Reconstructed conductivity distribution (in S/m) using conventional method (i) Reconstructed conductivity distribution (in S/m) using proposed method at the central axial slice.

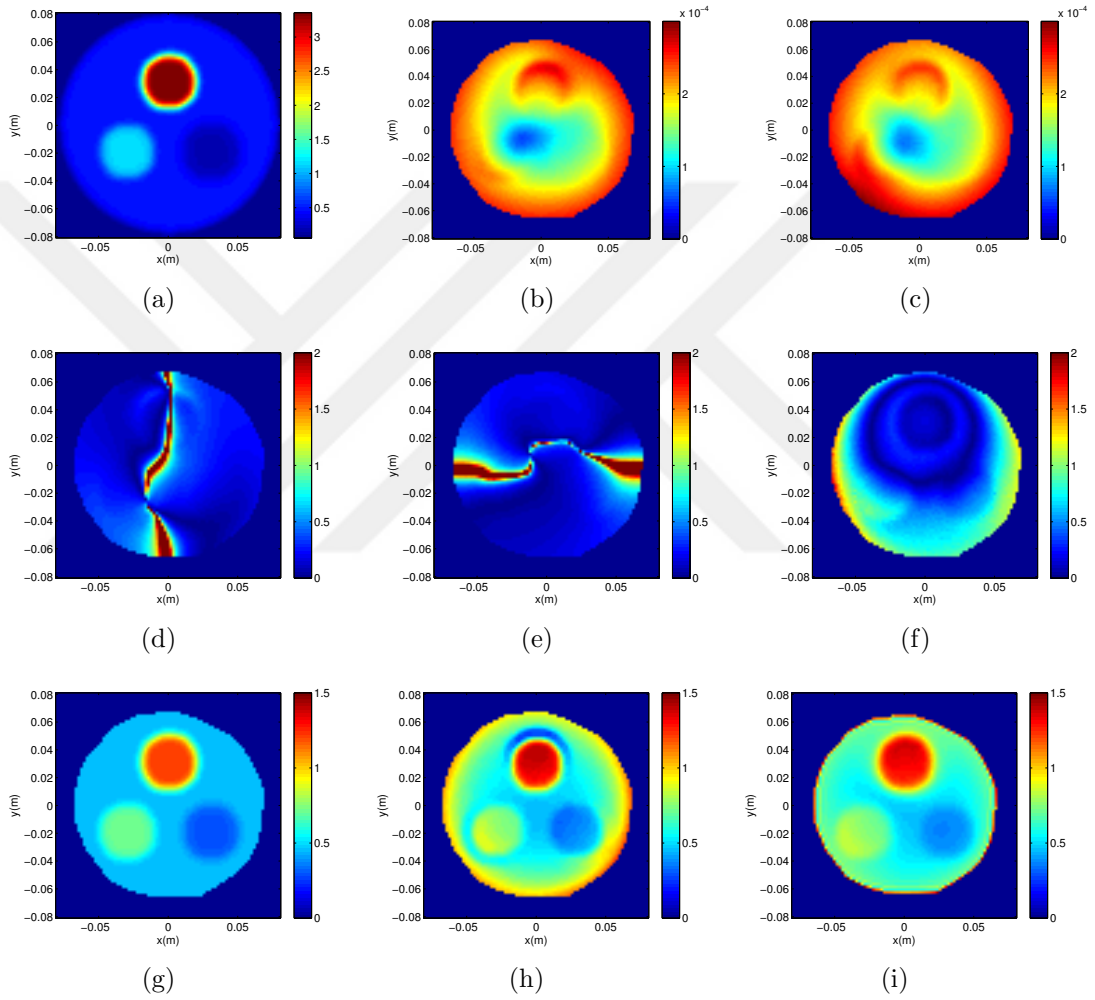

Figure 4.15: Results of the second scenario ($7T$ case when $\epsilon_r = 40$). (a) $\frac{\sigma^2}{(\omega\epsilon)^2}$, (b) $|\nabla B_1^+|$, (c) $|\nabla B_1^-|$, (d-f) imaginary part of each spatial component (x-, y-, and z-) of the B_z terms are divided by the imaginary part of the corresponding component in the phase terms. (g) Actual conductivity (in S/m) (h) Reconstructed conductivity distribution (in S/m) using conventional method (i) Reconstructed conductivity distribution (in S/m) using proposed method at the central axial slice.

is found to be 35% for this case.

From these results, it can be deduced that the effect of the violation of the second assumption ($|\nabla B_1^{\pm}| = 0$) on the conductivity results is more significant than that of the violation of the first assumption ($\sigma^2 >> (\omega\epsilon)^2$). In other words, if the first assumption is broken while the second assumption still holds, the conductivity results will be still acceptable. Validity of this argument can be better recognized in the following results. Figure 4.16 and Figure 4.17 show the results of two field strengths ($1.5T$ and $3T$), when the relative permittivity is taken as 80.

When $\epsilon_r = 80$, the first assumption is violated in the low conductive and the background region even in the $1.5T$ case (see Figure 4.16 (a)), and is violated everywhere in the $3T$ case (see Figure 4.17 (a)). The value of the $\frac{\sigma^2}{(\omega\epsilon)^2}$ is found to be 17.8, 6.0, 2.0, and 1.1 for $1.5T$ case; is found to be 4.4, 1.51, 0.5, and 0.3 for $3T$ case from high conductive to low conductive region, respectively. The second assumption, on the other hand, starts to break in $1.5T$ case, and it does not hold at the periphery of the phantom in the $3T$ case. These can be observed in Figure 4.16 (b)-(c) and Figure 4.17 (b)-(c). Despite these violations the total average error in the reconstructed conductivity map is found to be 4.7% for $1.5T$ case and 13% for $3T$ case. These results validate the argument mentioned in the previous paragraph that as long as the second assumption holds (or is slightly broken), breaking of the first assumption do not significantly affect the results, and the error in the conductivity images would be acceptable. For better visualization, conductivity profiles for all above cases in this scenario are given in Figure 4.18.

All the cases in this scenario were intended to understand the effects of violating the first and the second assumptions on the conductivity results of the proposed method. It can be concluded that the optimum region to employ the proposed method is the region where the magnetic field amplitudes ($|B_1^{\pm}|$) has uniform distribution. This condition is also necessary for standard MR imaging, and it is mostly satisfied at 1.5T and 3T MRI systems. For higher field strengths, e.g. $7T$, the use of birdcage coil will not be useful even for standard

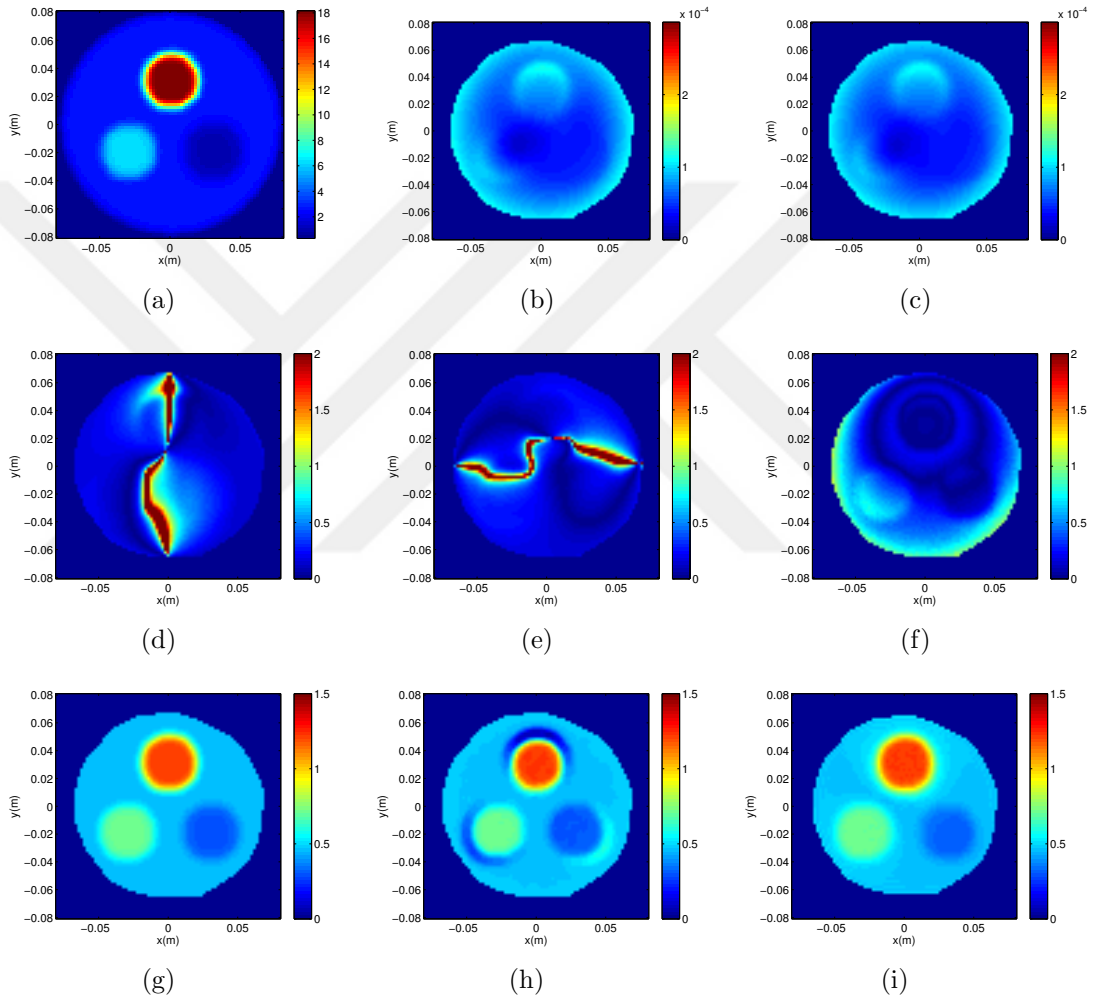

Figure 4.16: Results of the second scenario ($1.5T$ case when $\epsilon_r = 80$).(a) $\frac{\sigma^2}{(\omega\epsilon)^2}$, (b) $|\nabla B_1^+|$, (c) $|\nabla B_1^-|$, (d-f) imaginary part of each spatial component (x-, y-, and z-) of the B_z terms are divided by the imaginary part of the corresponding component in the phase terms. (g) Actual conductivity (in S/m) (h) Reconstructed conductivity distribution (in S/m) using conventional method (i) Reconstructed conductivity distribution (in S/m) using proposed method at the central axial slice.

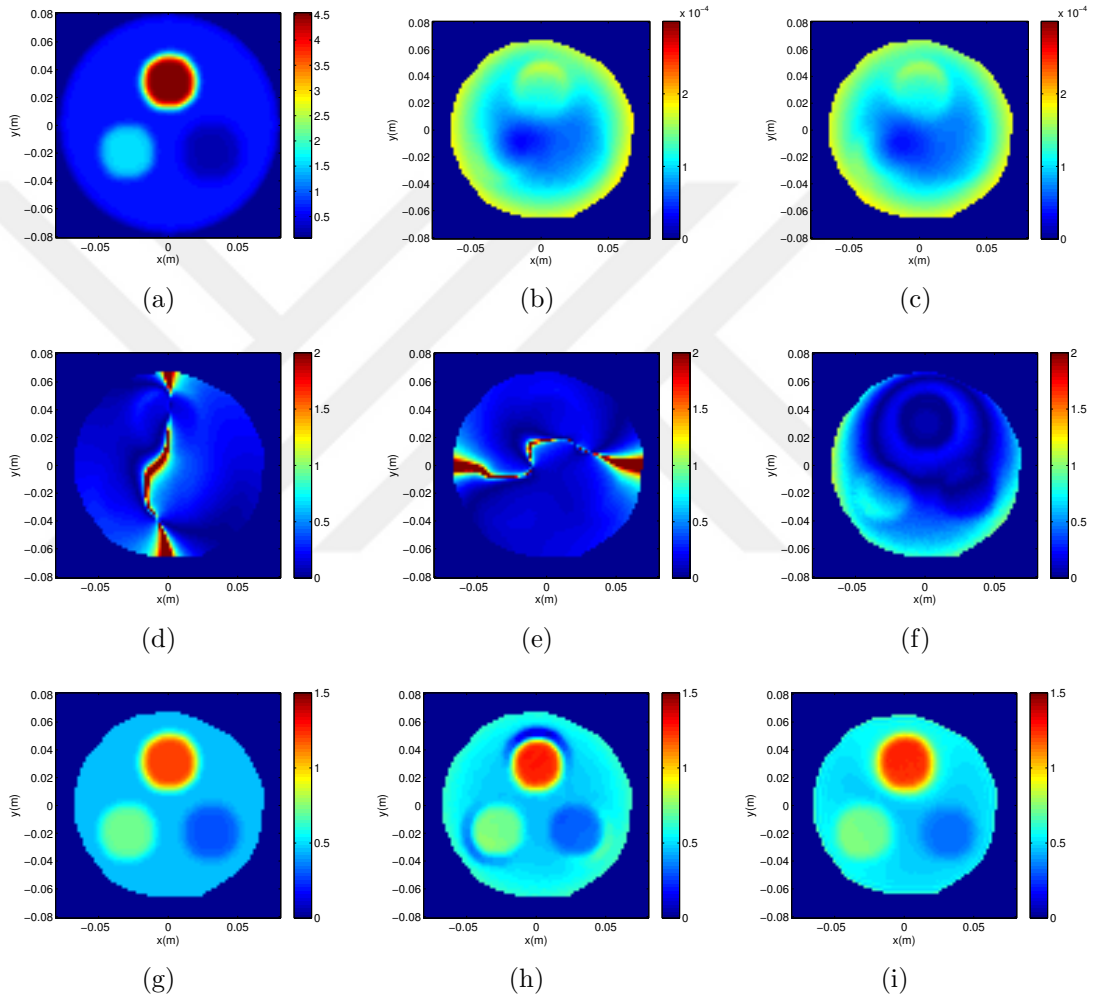

Figure 4.17: Results of the second scenario ($3T$ case when $\epsilon_r = 80$). (a) $\frac{\sigma^2}{(\omega\epsilon)^2}$, (b) $|\nabla B_1^+|$, (c) $|\nabla B_1^-|$, (d-f) imaginary part of each spatial component (x-, y-, and z-) of the B_z terms are divided by the imaginary part of the corresponding component in the phase terms. (g) Actual conductivity (in S/m) (h) Reconstructed conductivity distribution (in S/m) using conventional method (i) Reconstructed conductivity distribution (in S/m) using proposed method at the central axial slice.

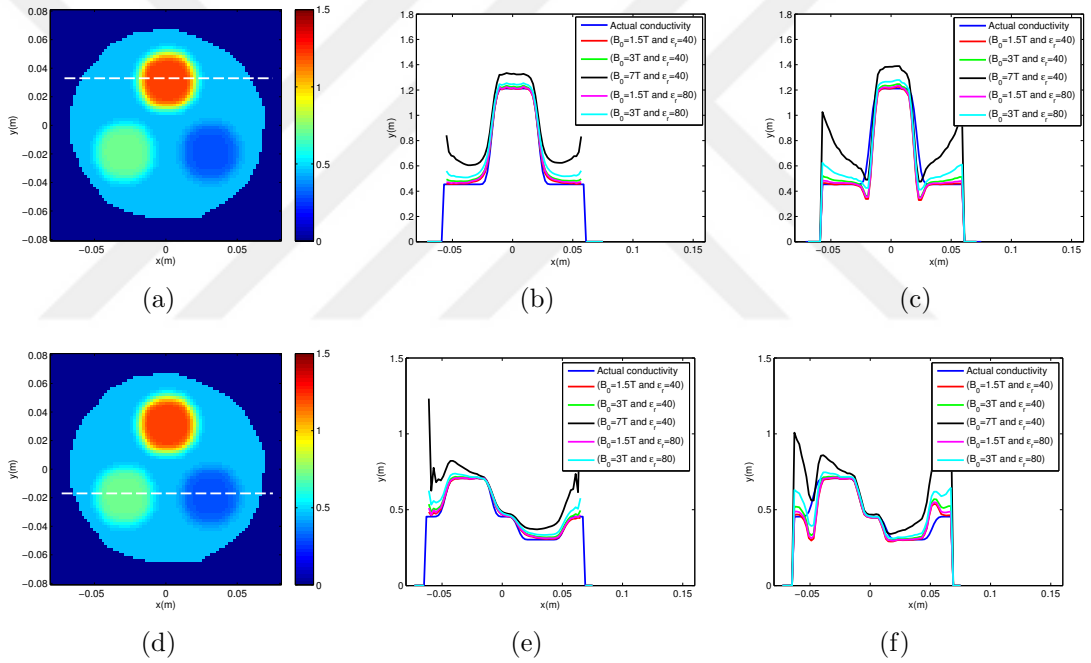

Figure 4.18: Profile plots for scenario 2. (a),(d) Illustration of the line where the conductivity profiles are plotted. (b),(e) Conductivity profiles (in S/m) for the proposed method. (c),(f) Conductivity profiles (in S/m) for the conventional method.

MR imaging, since the uniformity of the magnetic field will be deteriorated. Instead, multi-channel transmit coils are employed at this field strength, and using RF-shimming techniques, a uniform magnetic field is generated in the ROI (not the whole volume). Furthermore, Katscher et al. showed that the RF shimming improves the electrical conductivity results of the conventional phase based EPT method at 7T [78]. Similar approach can also be used for the proposed method at high field strengths. The third assumption, on the other hand, was satisfied in all cases, or even if it was not satisfied in some part of the phantom (see Figure 4.11 (f)) its effect was negligible on the conductivity images. Therefore, to better analyze the third assumption, a more complex phantom will be used in the next scenario.

Scenario 3: In this scenario, a more complex simulation phantom, which has z-variant compartments (the structure of the compartments is changing in the z-direction), was modeled so that the conductivity distribution is also varying in z- direction. In addition to using birdcage coil, a surface coil was also employed for both transmit and receive operations in this scenario. The complete model is shown in Figure 4.19.

In this scenario, all the electromagnetic analyses were performed at 3T, the relative permittivity value for all compartments was taken as 80, and the conductivity distribution for the desired slice is as shown in Figure 4.19 (b). Additionally, the conductivity transition between the compartments is sharper compared to previous scenarios. Before giving the results of this model, the same phantom was first put in the head birdcage coil for the comparison purposes. The results, when the head birdcage coil is used, are shown in Figure 4.20.

The results of the first and the second assumptions, which are shown in Figure 4.20 (a)-(c), are similar to the results in the 3T case (when $\epsilon_r = 80$) of the previous scenario. However, the result of the z-component of the third assumption is different from the other cases, and it is violated especially in the two compartment regions (see the saturated regions in Figure 4.20 (f)). The conductivity results of both method are given in Figure 4.20 (h) and (i). The overall increase in the conductivity results are again due to the violation of the second assumption,

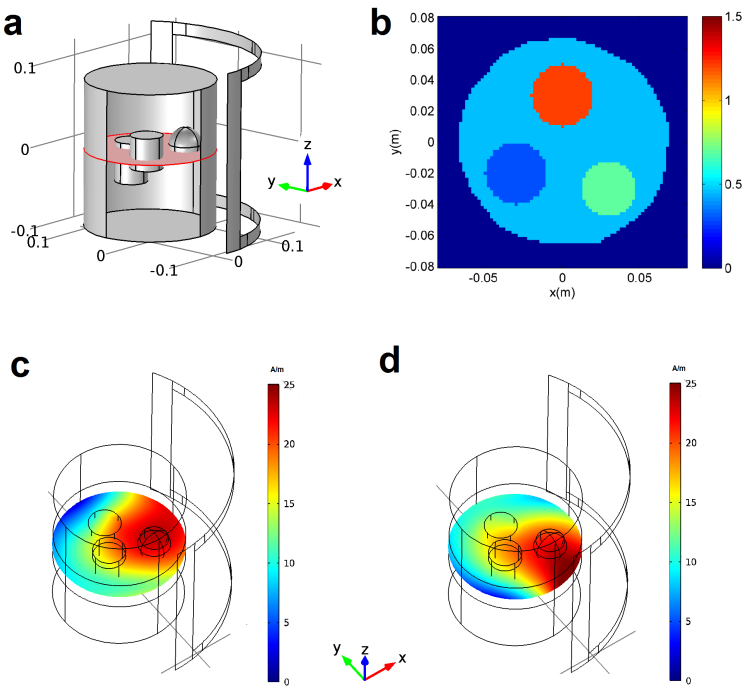

Figure 4.19: (a) Simulation phantom and the surface coil model used for the third scenario. (b) Conductivity distribution (in S/m) at the slice shown with red. (c) Distribution of $|B_1^+|$. (d) Distribution of $|B_1^-|$.

because the total average error in the conductivity result of the proposed method was found to be 12.8%, which is similar to the 3T case in the previous scenario. As mentioned previously, the violation of the third assumption has an effect only in the transition regions of the object, and for this case it appears to be negligible effect on the conductivity reconstruction around these regions. The use of diffusion term may also prevent the possible errors in the transition regions by preventing the high variations. The effect of use of diffusion term will be explained in detail in the next section.

For the second case, simulations were conducted using the surface coil model which is shown in Figure 4.19 (a). It is used for both transmit and receive operations. The distributions of the $|B_1^+|$ and $|B_1^-|$ of this coil are given in Figure 4.19 (c) and (d). As can be seen, the coil has a uniform distribution only in some part of the phantom, which is close to the coil. The results of the second case are illustrated in Figure 4.21.

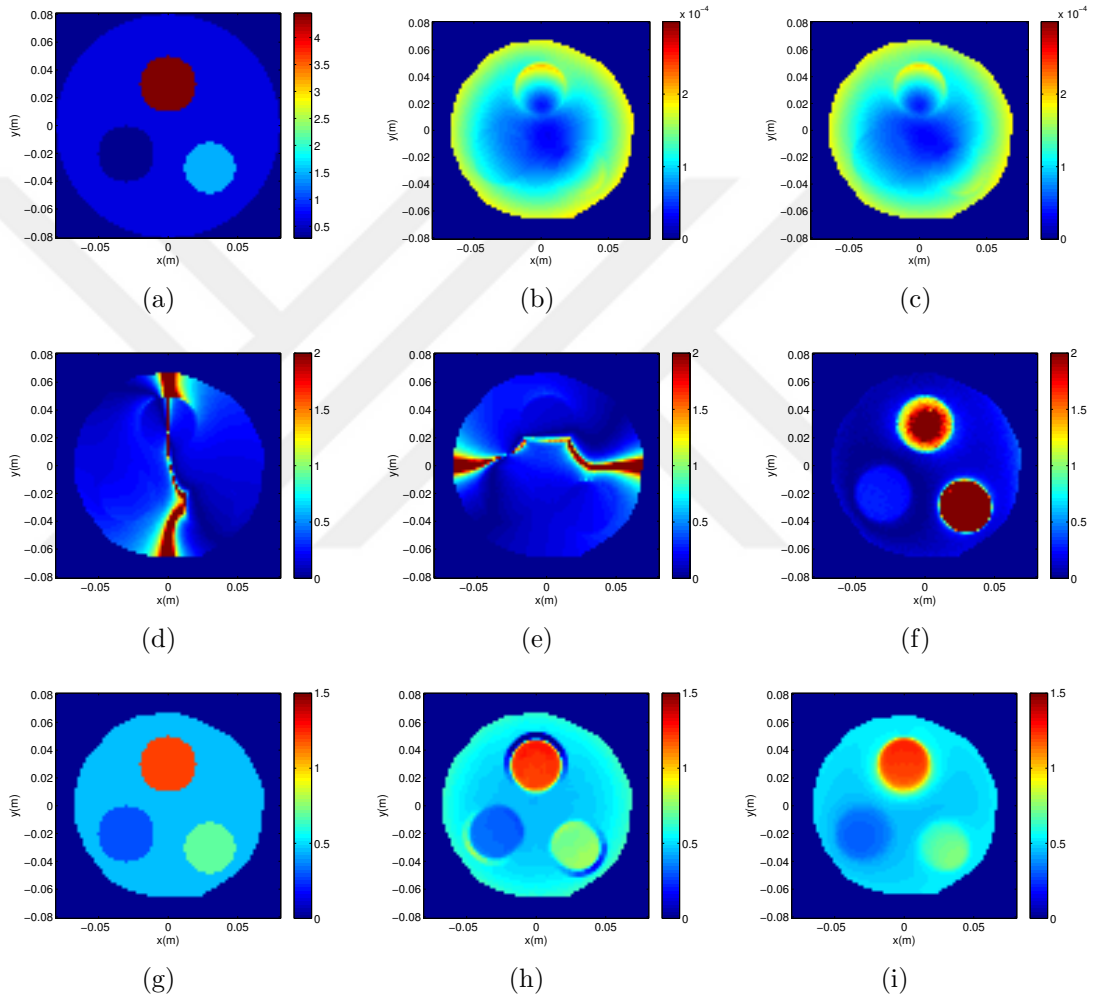

Figure 4.20: Results of the third scenario (when the birdcage coil is used). (a) $\frac{\sigma^2}{(\omega\epsilon)^2}$, (b) $|\nabla B_1^+|$, (c) $|\nabla B_1^-|$, (d-f) imaginary part of each spatial component (x-, y-, and z-) of the B_z terms are divided by the imaginary part of the corresponding component in the phase terms. (g) Actual conductivity (in S/m) (h) Reconstructed conductivity distribution (in S/m) using conventional method (i) Reconstructed conductivity distribution (in S/m) using proposed method at the central axial slice.

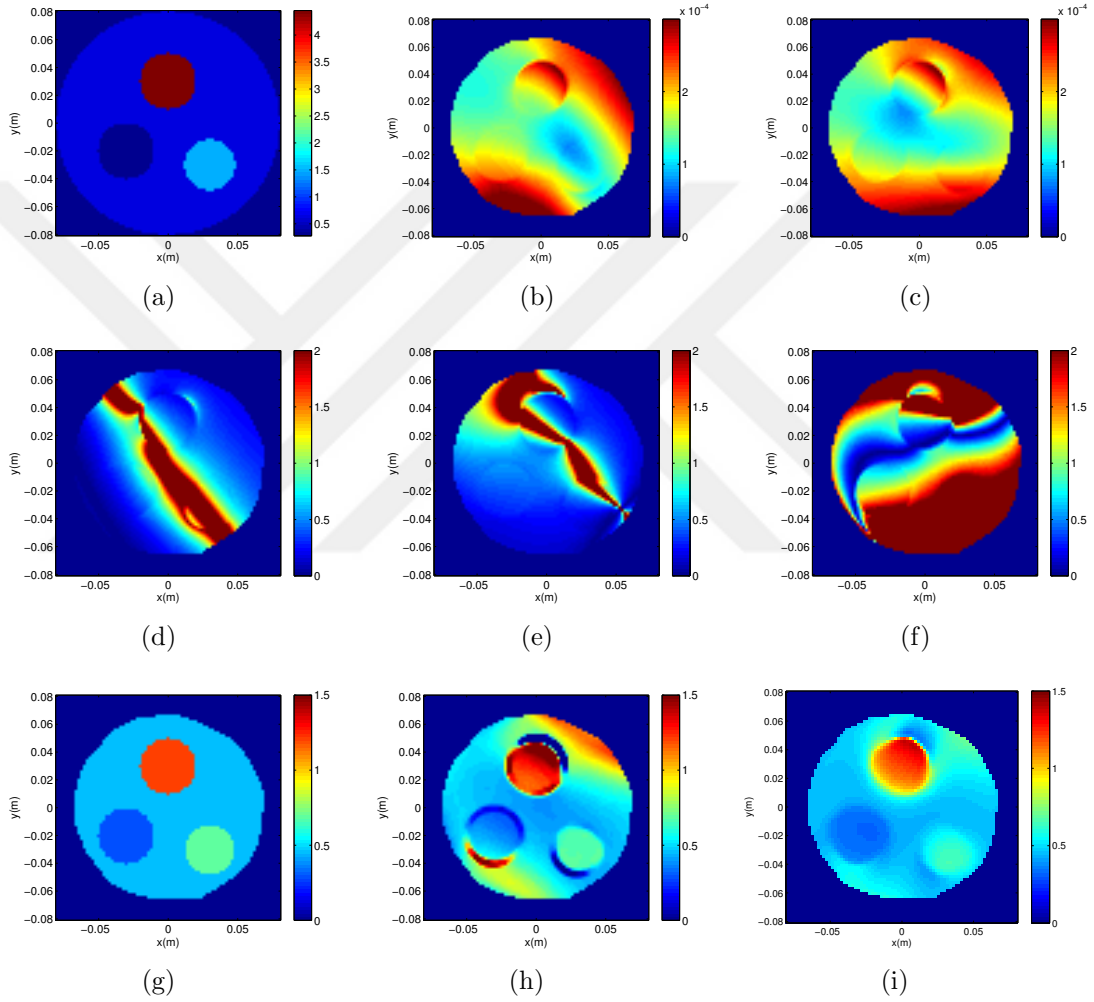

Figure 4.21: Results of the third scenario (when the surface coil is used). (a) $\frac{\sigma^2}{(\omega\epsilon)^2}$, (b) $|\nabla B_1^+|$, (c) $|\nabla B_1^-|$, (d-f) imaginary part of each spatial component (x-, y-, and z-) of the B_z terms are divided by the imaginary part of the corresponding component in the phase terms. (g) Actual conductivity (in S/m) (h) Reconstructed conductivity distribution (in S/m) using conventional method (i) Reconstructed conductivity distribution (in S/m) using proposed method at the central axial slice.

As shown in Figure 4.21 (b) and (c), the second assumption only holds in some part of the phantom when the surface is coil is used. Also, this region is not exactly the same for $|\nabla B_1^+|$ and $|\nabla B_1^-|$. The third assumption is again violated in this case (see Figure 4.21 (d)-(f)), and the results of the conductivity distributions are shown in Figure 4.21 (h) and (i). As can be seen from the conductivity maps, there is an increase in the regions where the second assumption fails. This is the same effect we have observed when the birdcage coil is used. However, in the results of the birdcage coil, the second assumption fails at the entire periphery of the phantom. For the case of the surface coil, on the other hand, there are some regions at the periphery that the second assumption holds. For example, conductivity is well reconstructed in the peripheral region, which is close to the surface coil (see Figure 4.21 (i)).

The other issue is that there is a boundary-artifact like dark region at the boundary of the high conductive compartment in the results of the proposed method. In the surface coil experiments, and also for the more complex objects, there is a possibility that the convection term may be close to zero at the boundary, in which Laplacian term is also unreliable. When this happens, huge variations in the conductivity is allowed in the solutions. To investigate this situation, convection terms are given in Figure 4.22.

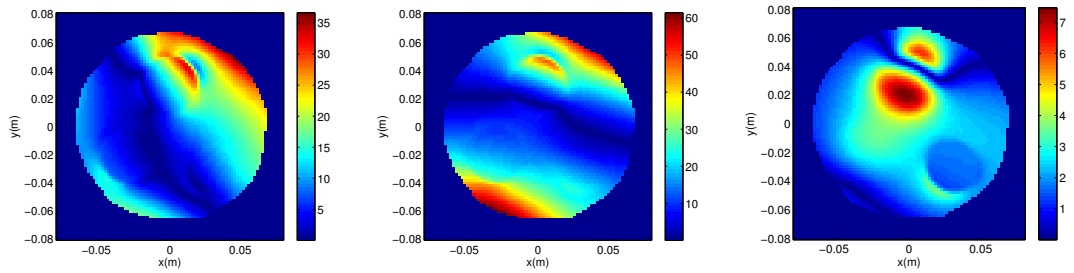

(a) (b) (c)

Figure 4.22: (a) x- component of the convection term ($\frac{\partial \phi^{tr}}{(} inrad/m)\partial x$) (b) y-component of the convection term ($\frac{\partial \phi^{tr}}{\partial y}$) (in rad/m) (c) z- component of the convection term ($\frac{\partial \phi^{tr}}{\partial z}$) (in rad/m).

As can be seen in Figure 4.22, the convection terms at the boundary of the high conductive compartment are close to zero, especially the x- and z- component

of the convection terms. This could be the main problem of that darkening. However, in practice, there will be more than one channel, and the magnetic fields generated by each channel will be different, resulting in a different convective field. Combining each channel data in a logical manner would give better conductivity results. This approach is similar with the one proposed in Chapter 3. To validate this argument, one more case (the third case) was studied in this scenario. In this case, the surface coil was rotated around the phantom, and the rest left unchanged. This can be thought as a second channel, and the electromagnetic fields were computed under these conditions. $|B_1^+|$ and $|B_1^-|$ distributions of the second channel are shown in Figure 4.23.

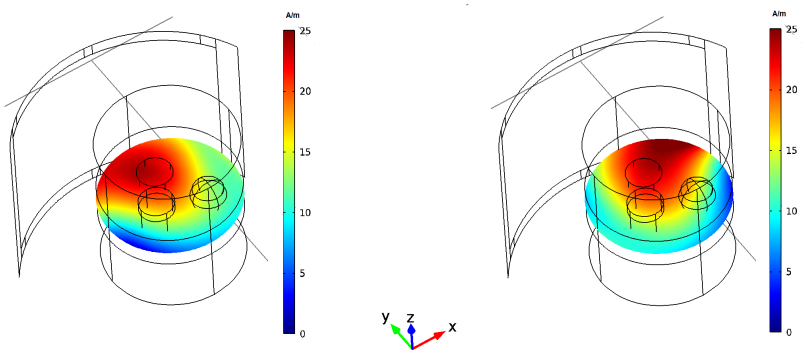

Figure 4.23: (a) $|B_1^+|$ and (b) $|B_1^-|$ distributions for the rotated surface coil. The coil itself is also shown in the plots.

As expected, the field distribution inside the phantom has changed compared to the previous case. The assumption plots and the conductivity results for this case are given in the following Figure 4.24.

It is observed in the results of the rotated surface coil that the place of the region, where the second assumption is valid, and the dark region in the previous case has changed (see Figure 4.24 (b) and (c)). As a result, the conductivity distribution has also changed (see Figure 4.24 (i)). This is a promising result for the application of the proposed method in multi-channel coil configuration systems, and also in high-field systems because it implies that using multi-channel coil systems one can manipulate the magnetic fields to meet the assumptions, especially the second assumption of the proposed method. On the other hand, the total average error in the conductivity results of the proposed method was found

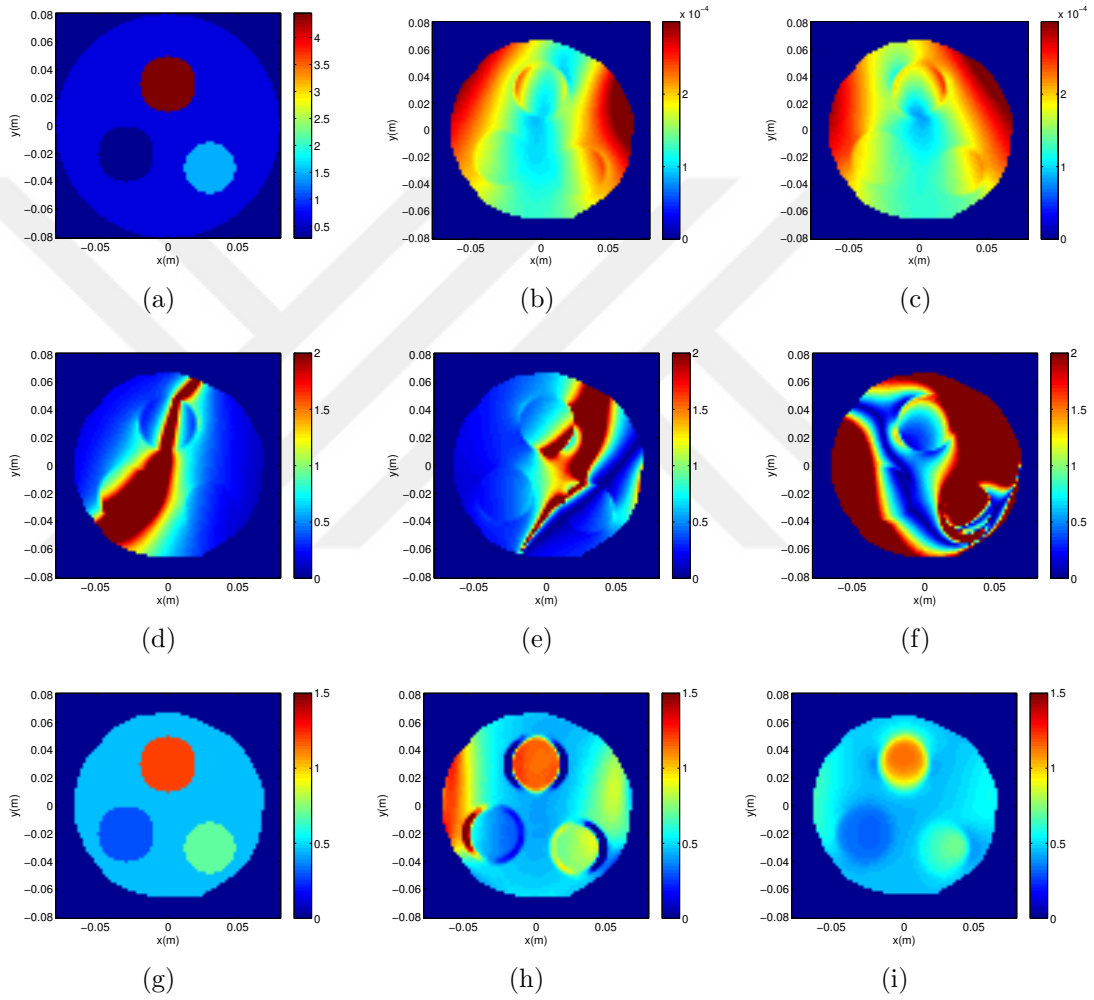

Figure 4.24: Results of the third scenario (when the surface coil is rotated). (a) $\frac{\sigma^2}{(\omega\epsilon)^2}$, (b) $|\nabla B_1^+|$, (c) $|\nabla B_1^-|$, (d-f) imaginary part of each spatial component (x-, y-, and z-) of the B_z terms are divided by the imaginary part of the corresponding component in the phase terms. (g) Actual conductivity (in S/m) (h) Reconstructed conductivity distribution (in S/m) using conventional method (i) Reconstructed conductivity distribution (in S/m) using proposed method at the central axial slice.

to be 14.1% and 13.9% for the second and the third cases, respectively. If the error calculation was made only within the valid region, where the assumptions mostly hold, the error would be 9%. This also encourages the use of multichannel configuration systems to employ the proposed method because even if the total error in the case of surface coil is high compared to the case of birdcage coil, in the valid region the error in the surface coil results is lower than that of birdcage coil. Last, the convective fields for this case are shown in Figure 4.25. As can be predicted, the convective fields also changes compared to the previous case.

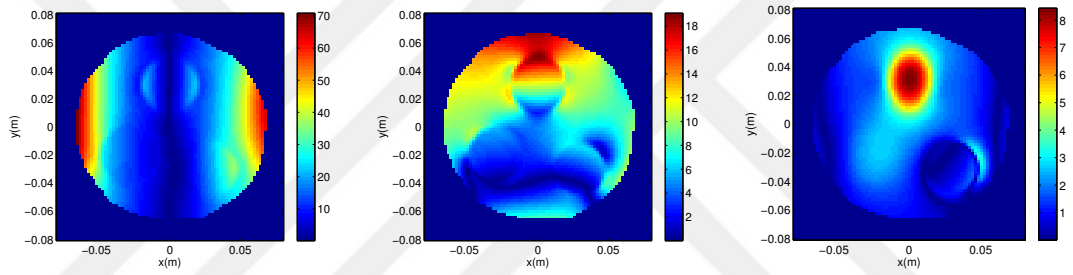

(a) (b) (c)

Figure 4.25: Convective fields for the rotated surface coil case. (a) x- component of the convection term ($\frac{\partial \phi^{tr}}{\partial x}$) (in rad/m) (b) y- component of the convection term ($\frac{\partial \phi^{tr}}{\partial y}$) (in rad/m) (c) z- component of the convection term ($\frac{\partial \phi^{tr}}{\partial z}$) (in rad/m).

To sum up, in this scenario, our aim was to analyze the effect of the third assumption on the conductivity maps but it turns out that we have not observed any remarkable effect of the violation of this assumption as long as the second assumption holds. Besides, it can be deduced that the surface coil can also be used in the application of the proposed method. There is an optimum region, where both the $|\nabla B_1^+|$ and $|\nabla B_1^-|$ is relatively low, for each channel. This region was found as close to the center of the coil in our simulations. This region also corresponds to the most sensitive region of that coil, which is also an important issue for high SNR.

Scenario 4: In the last scenario, we will examine the performance of the proposed method for the human brain model. Although similar simulation was made for $3T$ case in Section 4.3.1, in this scenario $1.5T$ and $7T$ cases will also be investigated. Additionally, the results will be examined at the sagital plane.

The same human model, which was shown in Figure 4.2, was used. For the coil, the same head birdcage coils designed for $1.5T$, $3T$, and $7T$ were employed. The results of all three field strengths for the human brain model are shown in Figure 4.26 - 4.28.

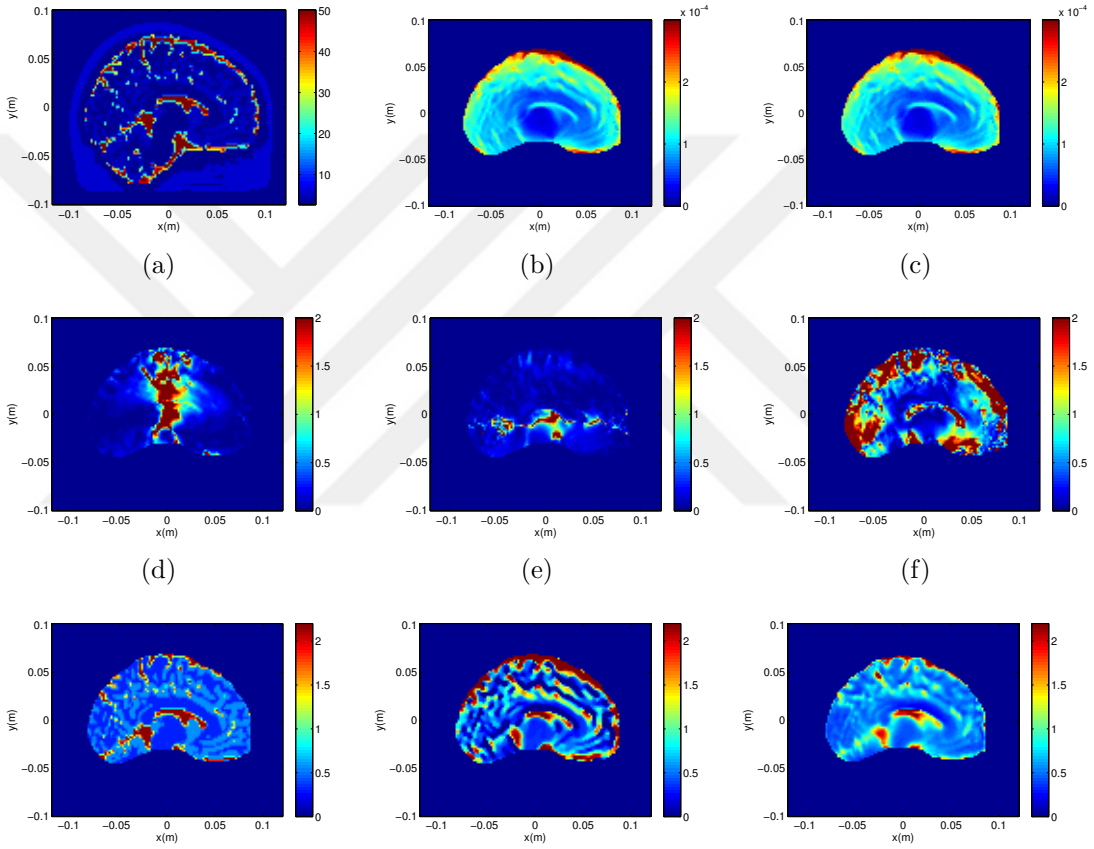

Figure 4.26: Results of the fourth scenario ($1.5T$ case). (a) $\frac{\sigma^2}{(\omega\epsilon)^2}$, (b) $|\nabla B_1^+|$, (c) $|\nabla B_1^-|$, (d-f) imaginary part of each spatial component (x-, y-, and z-) of the B_z terms are divided by the imaginary part of the corresponding component in the phase terms. (g) Actual conductivity (in S/m) (h) Reconstructed conductivity distribution (in S/m) using conventional method (i) Reconstructed conductivity distribution (in S/m) using proposed method at the central axial slice.

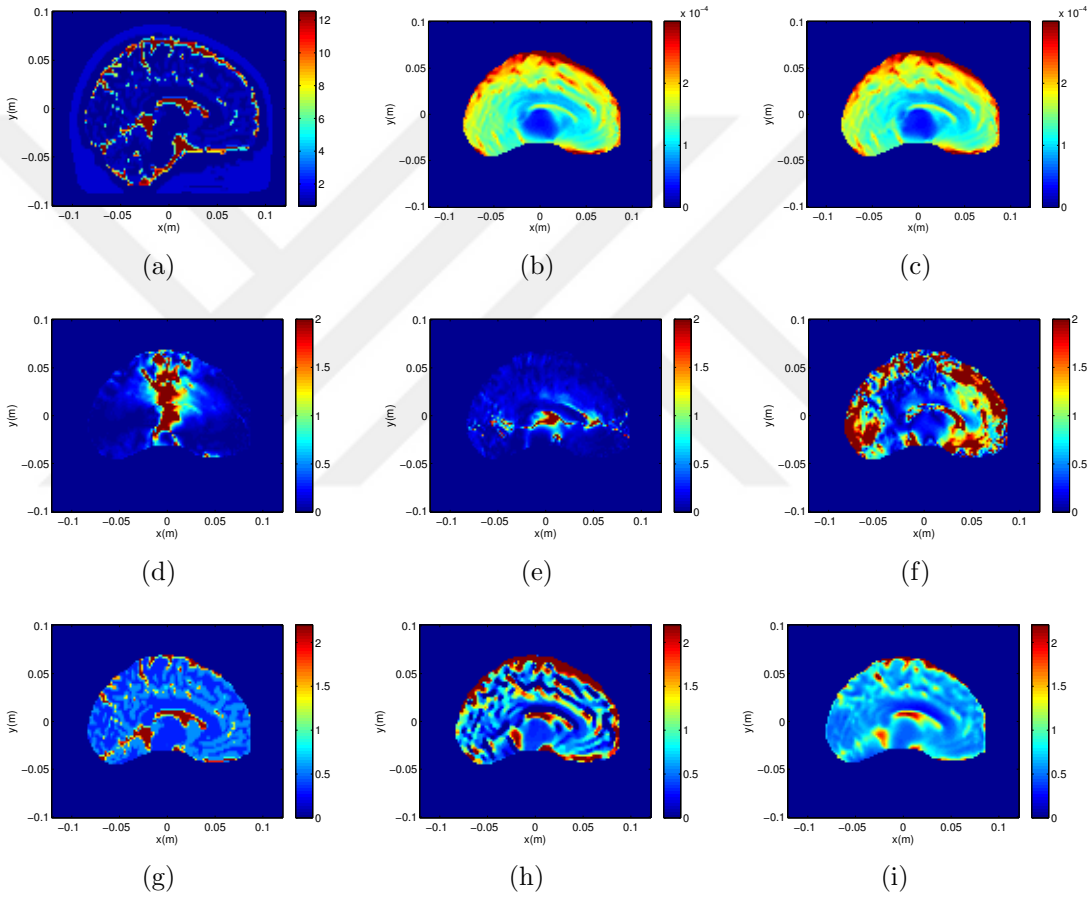

Figure 4.27: Results of the fourth scenario ($3T$ case). (a) $\frac{\sigma^2}{(\omega\epsilon)^2}$, (b) $|\nabla B_1^+|$, (c) $|\nabla B_1^-|$, (d-f) imaginary part of each spatial component (x-, y-, and z-) of the B_z terms are divided by the imaginary part of the corresponding component in the phase terms. (g) Actual conductivity (in S/m) (h) Reconstructed conductivity distribution (in S/m) using conventional method (i) Reconstructed conductivity distribution (in S/m) using proposed method at the central axial slice.

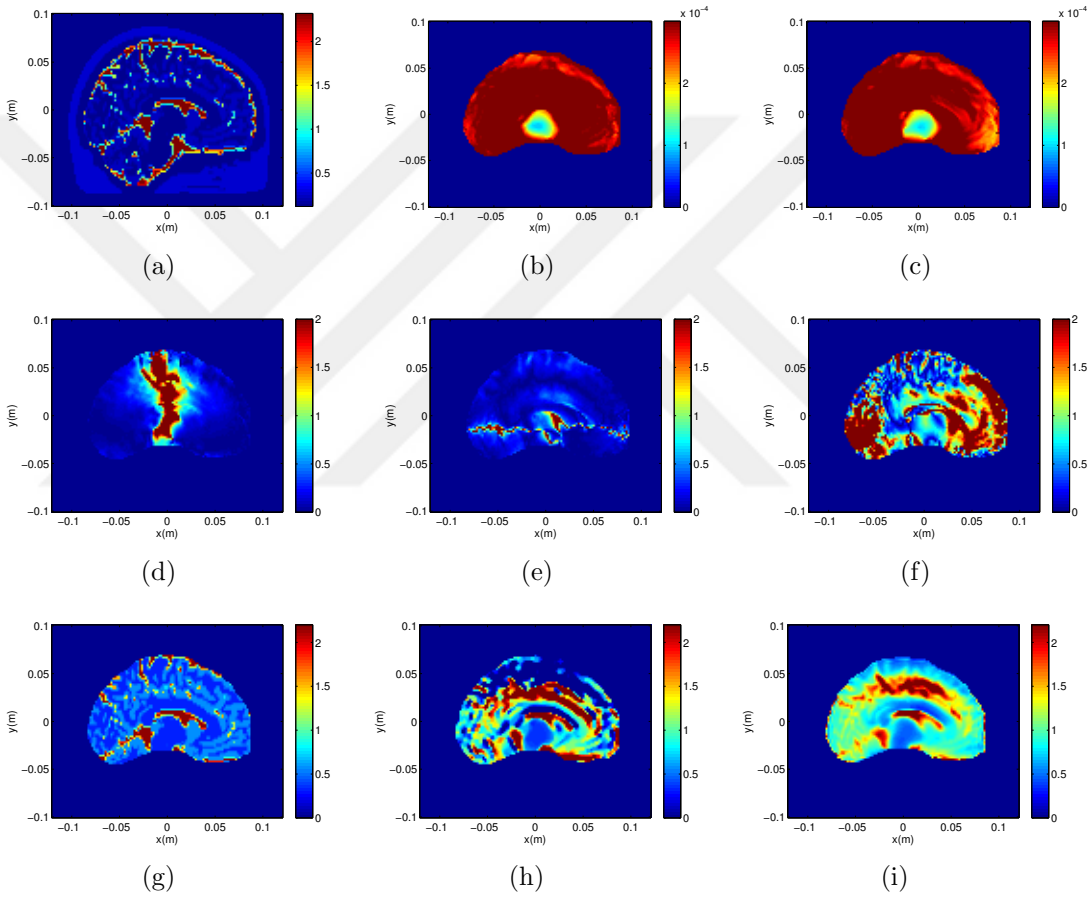

Figure 4.28: Results of the fourth scenario ($7T$ case). (a) $\frac{\sigma^2}{(\omega\epsilon)^2}$, (b) $|\nabla B_1^+|$, (c) $|\nabla B_1^-|$, (d-f) imaginary part of each spatial component (x-, y-, and z-) of the B_z terms are divided by the imaginary part of the corresponding component in the phase terms. (g) Actual conductivity (in S/m) (h) Reconstructed conductivity distribution (in S/m) using conventional method (i) Reconstructed conductivity distribution (in S/m) using proposed method at the central axial slice.

Several conclusions can be made by examining the results of the fourth scenario. One of them is that $1.5T$ and $3T$ are the most suitable field strengths for the proposed method when the birdcage coil is used. Even in $1.5T$, the second assumption starts to fail at the periphery of the brain phantom which causes an increase in the corresponding region of the conductivity images. However, the contrast variations in the conductivity images were kept both in $1.5T$ and $3T$ (see Figure 4.26 (i) and 4.27 (i)). This is an important result for the clinical applications of the proposed method because instead of finding the conductivity quantitatively, contrast variations in the conductivity images could be used for the clinical diagnosis as in the case of susceptibility weighted imaging [79]. Second, for the higher field strengths, e.g. $7T$, multi-channel coil systems should be adapted to the proposed method because the use of birdcage coil will not be sufficient. The results of the third scenario and the previous studies in the literature [78] also encourage the use multi-channel coil systems by showing that it is possible to generate a magnetic field that meets the conditions in the second assumption. Last but not least, the results in this section also show the superiorities of the proposed method over the conventional method in terms of boundary reconstruction, and robustness against assumption violation.

4.4.2 Boundary Condition and Diffusion Term

As previously mentioned, to solve the governing partial differential equation of the proposed method Dirichlet boundary condition (BC) is applied. This BC implies that the conductivity value on the boundary of the ROI is assumed to be known. However, in practice, we do not know the exact conductivity value of the boundary region, and we give an average conductivity value to the boundary of the ROI. Our analysis has shown that the exact value assigned to the boundary is not critical except for a narrow band around the boundary. In other words, even if the boundary condition is taken as very different from the actual value, the solution immediately decays to the desired value within a few pixels. This can be seen in Figure 4.29.

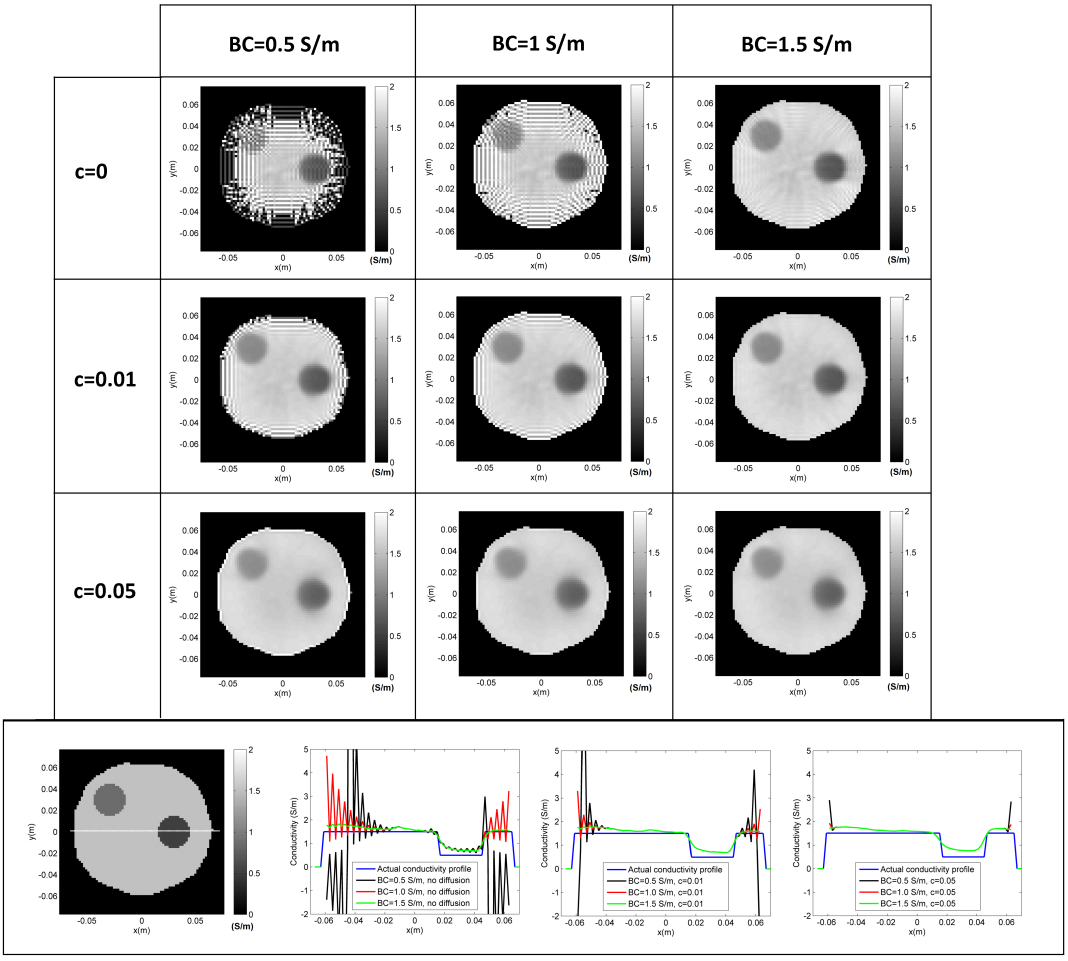

Figure 4.29: Illustration of the oscillatory decay from the given boundary (initial) value to the final value under different diffusion coefficients (c is used for diffusion coefficient) and boundary conditions (BC is for the value of the conductivity assigned at the boundary).

The same simulation phantom (shown in Figure 4.1 (a)) is used for this analysis, and therefore the exact background conductivity value was 1.5 S/m. For the worst case (no diffusion term and wrong boundary assignment (c=0, BC=0.5 S/m)), excessive spurious oscillations were observed in the conductivity map. However, these oscillations decrease as the BC approaches to the exact value of the background conductivity. For c=0.01, these oscillations were significantly reduced. For c=0.05, the effect of wrong BC is confined to a few pixels only. The results are also shown in the profile plots for better visualization in Figure 4.29. It can be deduced from these results that the use of diffusion term prevents the high variations caused by the wrong BC, and provides flexibility in giving BC. Therefore, in practice an average conductivity value can be assigned to the boundary of ROI which will not affect the solutions of the proposed method significantly.

In Figure 4.29, for the exact boundary condition case, spurious oscillations, which occurs due to the pure convection term, can be seen when there is no diffusion. Adding and artificial diffusion term stabilizes the solution by acting as a regularization term.

In the conventional cr-MREPT methods, it has been shown that LCF artifacts occurs in the regions where the magnitude of the convective field is low. A similar artifact can also be observed in the proposed method, when no diffusion term is used. With reference to Eq. 4.12, which does not include a diffusion term, it can be argued that if $\nabla^2\phi^{tr}$ and $\nabla\phi^{tr}$ are close to zero in the same region, huge variations (spot-like artifact) in ρ are allowed in the solutions. To validate this phenomena, reconstruction of human brain simulations were conducted using the proposed method with and without diffusion term. Results are illustrated in Figure 4.30.

It can be seen in Figure 4.30 that if both components of the convective field is close to zero at the transition regions (where the Laplacian term is unreliable), the solution have spot-like artifact, which are shown with the red arrows (see Figure 4.30 (b)). The use of diffusion term (c=0.05 for this case) prevents these high variations in the reconstructions and make the solutions more stable (see Figure 4.30 (c)).

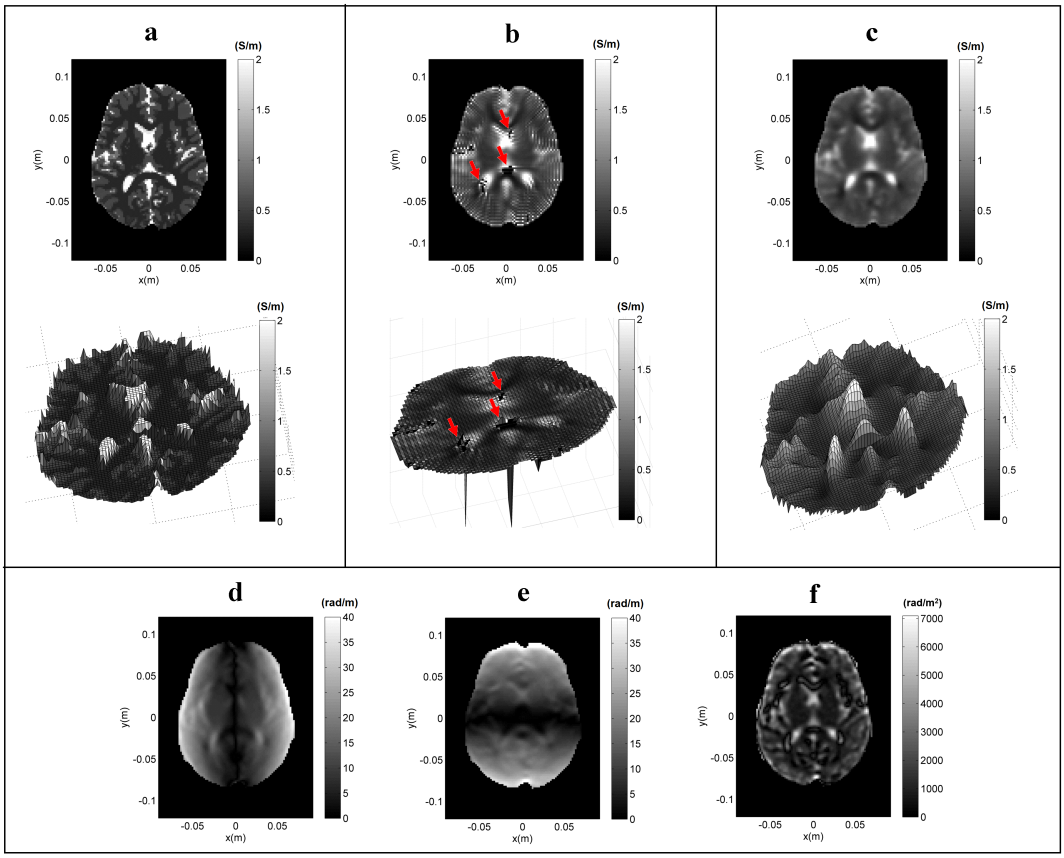

Figure 4.30: Reconstructed conductivity maps of simulated human brain for different diffusion coefficients. (a) 2D and 3D surface plots of the actual conductivity of an axial slice (b) 2D and 3D surface plots of reconstructed conductivity of the same slice for c=0 (c) Same as in (b) for c=0.05 (d) Magnitude of the x-component of the gradient of the transceive phase (e) Magnitude of the y-component of the gradient of the transceive phase (f) Magnitude of the Laplacian of the transceive phase

4.5 Clinical Applicability of the Proposed Method

So far, we have analyzed the limitation of the proposed method in theory. In this section, we aim to explore the clinically applicability of the proposed method. For this purpose, two patients with neurovascular diseases in the subacute phase, i.e. hemorrhagic and ischemic stroke, have been studied with the approval of Bilkent University Institutional Review Board, and the informed consent was filled by the patients. [57].

Case 1: In the first case, a 52-year-old woman with hemorrhage in the right hemisphere, near the lateral ventricle, was scanned seven days after the hemorrhage.

Case 2: In the second case, a 50-year-old man with ischemia in the right cerebellum and the right posterior cerebral artery territory was scanned seven days after the infarction.

Examinations for the conductivity measurement were performed on 3T Siemens Tim Trio MR scanner (Erlangen, Germany) using a quadrature body coil and 12-channel receive only phased array head coil installed in UMRAM. The transceive phase was acquired using 3D balanced SSFP sequence (with the parameters of FA=40 deg, TE/TR=2.32/4.64ms, FOV=200x200x187.2 mm (1.56x1.56x1.56 mm), NEX=5, total scan time:6min) for both cases. Along with these scans, we had also cranial CT, T2-weighted FLAIR images for the first case, and diffusion weighted imaging(DWI)/apparent diffusion coefficient(ADC) images for the second case, which had been gathered for the clinical diagnosis in the first day of stroke in Ankara Ataturk Training and Research Hospital Emergency Department.

Figure 4.31 shows the results of the first case. Figure 4.31 (a) and (b) are the cranial CT and T2-weighted FLAIR images. As can be seen, a hyperdense region

at the high frontal level in the right hemisphere appears in CT image (see Figure 4.31 (a)). This lesion is consistent with the acute phase intra-parenchymal hematoma with penumbral edema. The same lesion also appears in the T2-weighted FLAIR image with more heterogeneous interior (see Figure 4.31 (b)). Figure 4.31 (c) and (d) show the corresponding SSFP magnitude, and the reconstructed conductivity image obtained using proposed method. It has been found that the conductivity of the surrounding edema region increased, whereas the hematoma region itself depicts conductivity values similar to that of brain tissue.

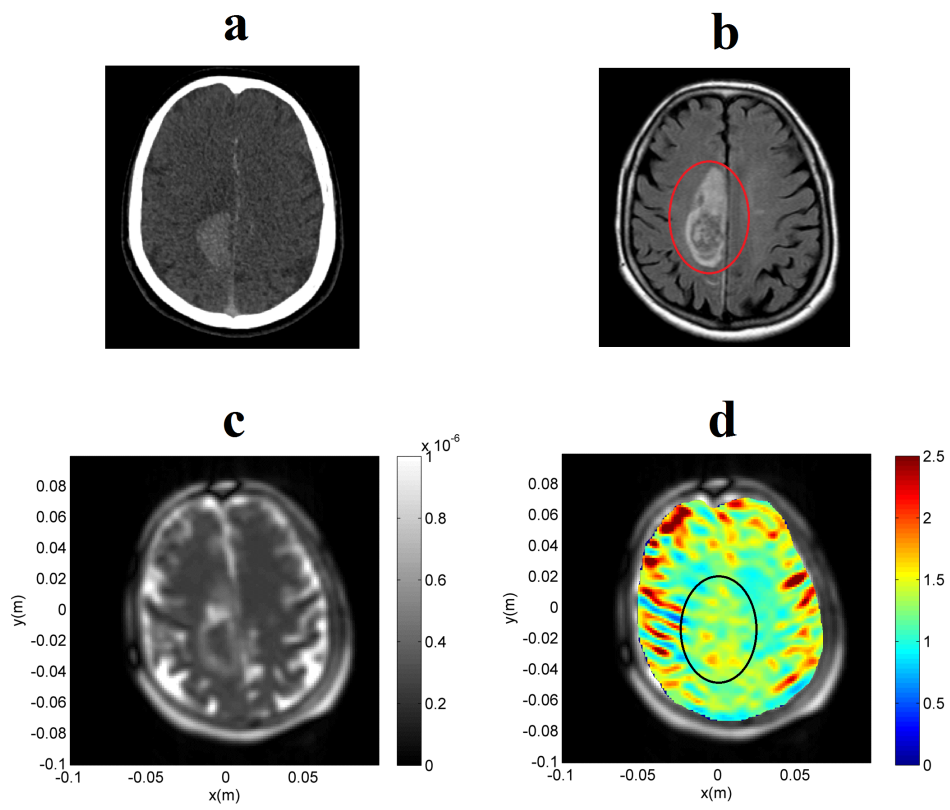

Figure 4.31: Images for the patient with hematoma. (a) CT image (b) T2W/FLAIR image (hematoma and surrounding edema are encircled) (c) Corresponding SSFP magnitude image (d) Corresponding conductivity image (hematoma and surrounding edema are encircled)

Figure 4.32 and Figure 4.33 show the results of the second case, in which the patient has two seperate infarcts, one in the left cerebellum and the other in the occipital lobe. Figure 4.32 (b) and (c) show the constrained diffusion region

in the DWI and ADC images, respectively. This indicates the acute infarction. Conductivity map of the corresponding slice is shown in Figure 4.32 (e). It has been found that the conductivity value increases consistent with the lesion location and heterogeneity.

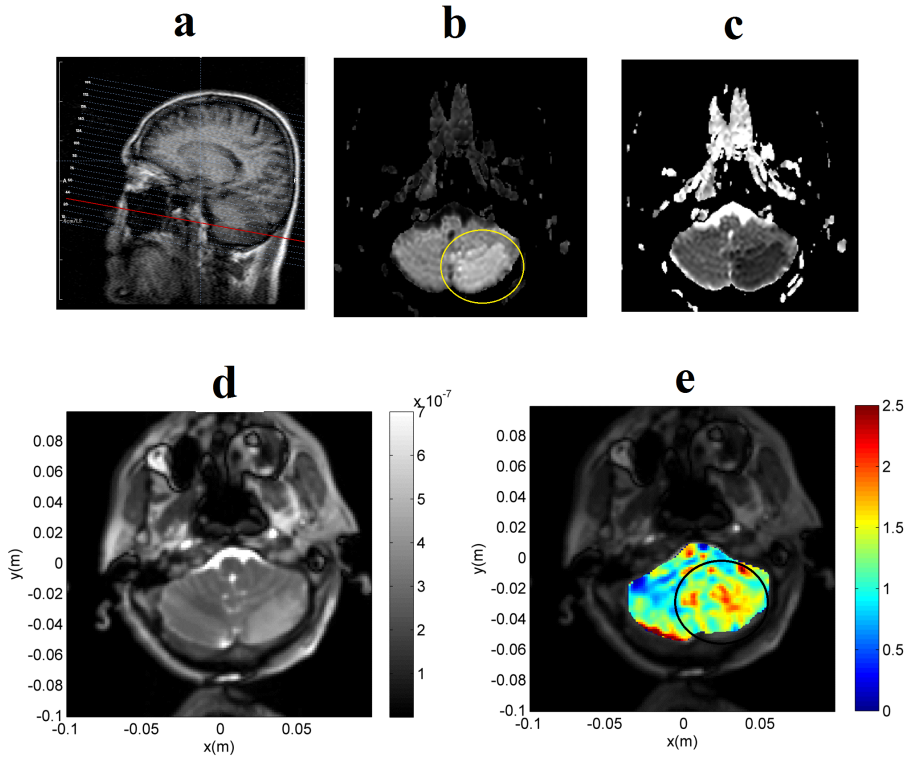

Figure 4.32: Images for the patient with ischemia in the left cerebellum. (a) Selected oblique slice (shown with red line) for parts b-c. (b) DWI image (infarction region is encircled) (c) ADC image (d) corresponding SSFP magnitude image (e) corresponding conductivity image (infarction region is encircled)

Similar findings are also observed in Figure 4.33, which is given for the occipital region. The conductivity value increases consistent with the lesion region (see Figure 4.33 (e)).

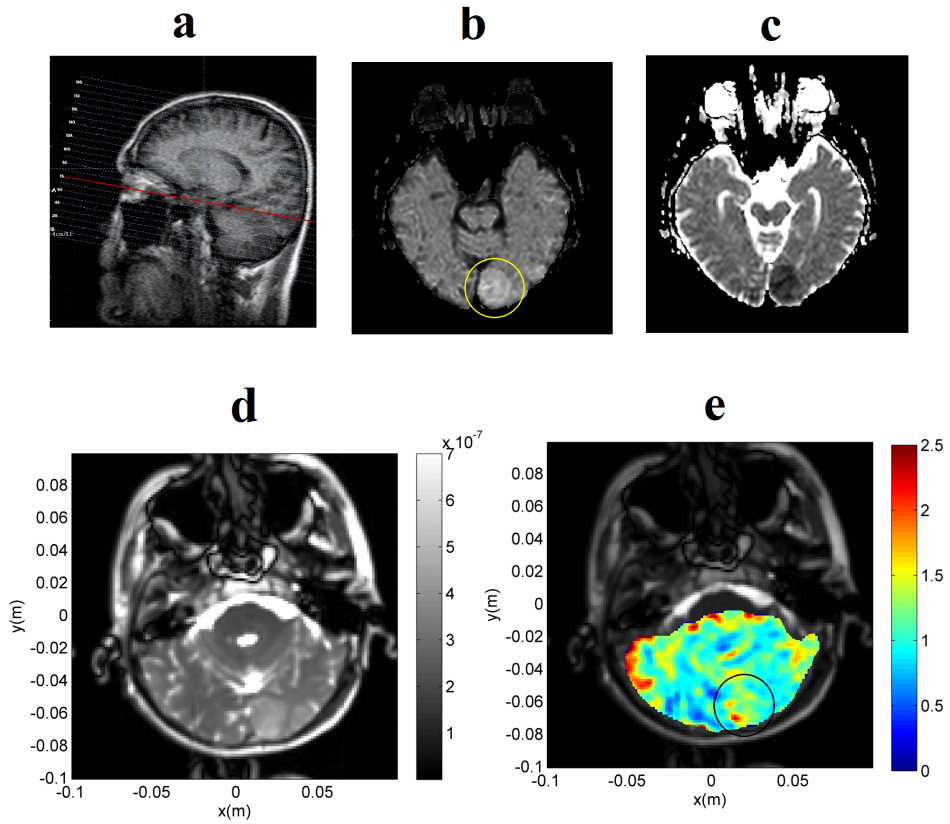

Figure 4.33: Images for the patient with ischemia in the occipital lobe (a) Selected oblique slice (shown with red line) for parts b-c. (b) DWI image (infarction region is encircled) (c) ADC image (d) corresponding SSFP magnitude image (e) corresponding conductivity image (infarction region is encircled)

In conclusion, in the case of subacute ischemic stroke, conductivity was found to be increased in the lesion area. In the case of subacute hematoma, on the other hand, conductivity distribution of the hematoma itself is found to be not significantly different from the brain tissue. Although in acute phase, hemorrhage may cause increased conductivity, in subacute phase this may not be so due to the clot formation. These results indicate promising potential for clinical use of the proposed phase based EPT method.

4.6 E_z based SAR Estimation Procedure

As previously mentioned another application of the proposed method could be the calculation of SAR distribution. Here, E_z based SAR estimation procedure is explained:

Writing the z- component of Ampere's Law ($\nabla \times \mathbf{H} = \gamma \mathbf{E}$) gives

$$\frac{\partial H_y}{\partial x} - \frac{\partial H_x}{\partial y} = \gamma E_z \tag{4.17}$$

Using the Gauss Law ($\nabla \cdot \mathbf{H} = 0$) and the definition of H^+ ($H^+ = \frac{H_x + iH_y}{2}$) Eq. 4.17 can be rewritten as

$$-2i\left(\frac{\partial H^+}{\partial x} - i\frac{\partial H^+}{\partial y} + \frac{1}{2}\frac{\partial H_z}{\partial z}\right) = \gamma E_z \tag{4.18}$$

In Eq. 4.18, $\frac{\partial H_z}{\partial z}$ could be neglected when compared to H^+ terms and the resulting equation will be

$$-2i\left(\frac{\partial H^+}{\partial x} - i\frac{\partial H^+}{\partial y}\right) = \gamma E_z \tag{4.19}$$

To find E_z, following procedure can be used:

- Complex H^+ map can be found using B_1 mapping technique and the TPA based transmit phase estimation.
- γ can be found using the proposed B_1^- based multi-channel cr-MREPT algorithm.
- Then, E_z is simply calculated using the Eq. 4.19.

Using the calculated E_z, SAR can be estimated for the case of $E_z >> Ex, Ey$ using the following equation

$$SAR \sim \sigma |E_z|^2 \tag{4.20}$$

Eq. 4.20 is valid especially at the center of the birdcage coil but the validity of this procedure should be examined for the other coil structures.

4.7 Discussion

In this study, an artifact free electrical conductivity imaging method based solely on the MR transceive phase has been proposed. Different from the previous phase based EPT approach (36,37), a new formulation, which is in the form of a convection reaction diffusion equation, was derived without assuming that the gradient of the conductivity is zero. With the contributions, this method resolves the boundary artifact issue in the conventional phase based EPT and LCF artifact issue in the conventional cr-MREPT methods, and paves the way for fast and reliable reconstruction of the conductivity maps of tissues in clinical applications. The performance of the proposed method has been validated with simulations, experiments, and case studies.

There are two significant advantages of the proposed method. One is the noise reduction ability while solving the governing equation. This comes from the use

of the diffusion term, which acts as a low-pass filter in the solutions without significantly blurring conductivity maps. The noise performance of the proposed method and the conventional method can be compared in Figures 4.3 and 4.4. The second advantage of the proposed method is the ability to reconstruct artifact free electrical conductivity images. Especially, for practical applications, due to the use of strong spatial filters to reduce the noise in the phase data, the boundary artifact in the conventional method, and LCF artifact in cr-MREPT method becomes wider. For complex structures (e.g. brain) this leads to unreliable conductivity maps, which are difficult to interpret for clinical diagnosis.

To derive the governing equation of the proposed method, several assumptions have been made, and they were discussed in detail in Section 4.4. This comprehensive analysis of these assumptions, on which the conventional phase based EPT approach also relies, makes us to better understand the effect of these assumptions on the reconstructed conductivity images. From these analysis, we have concluded that the violation of the second assumption significantly affects the conductivity reconstructions when compared to the other assumptions, especially in the case of using birdcage coil at $7T$. To employ the proposed method at $7T$, multi-channel coil configuration system must be used, in which a uniform $|B_1^{\pm}|$ can be obtained in the region near to the each channel. Then combining each channel data in a logical manner would give better conductivity results at high field strengths. On the other hand, the proposed method can be safely used at $1.5T$ and $3T$ MRI systems, and it has been shown that it provides an interpretable conductivity contrast not only in the results of the simulations but also in the results of the case studies.

The proposed method introduces the use of diffusion term. At a first glance, adding an artificial diffusion term is necessary to prevent spurious oscillations in the solution of the convection-reaction-equation but it turns out that the use of diffusion term has another advantages in addition to the stabilization. One is the low-pass filtering effect which suppress the noise in the MR data without significantly blurring the conductivity images (mentioned in the second paragraph of this section). Another advantage is that it prevents the LCF artifact in the low convective field region by acting as a regularization term. This issue was a

headache for conventional cr-MREPT method [43]. Last but not least, the use of diffusion term allows us to use an average conductivity value for the boundary condition which can be different from the exact conductivity value of that region. For example, in the human brain experiments, we use the conductivity value of 1.5 S/m as the boundary condition for whole brain selection because there are CSF regions adjacent to the periphery of the brain, and they are expected to have high conductivities.

We have also conducted two case studies to investigate the clinical applicability of the proposed method. For this purpose, we have taken two patients with neurovascular diseases, i.e hemorrhagic and ischemic stroke, in the sub-acute phase. The duration of the examination took six minutes for each patient. In the results, we have seen increase in the conductivity of the ischemic region, which can be possible in the sub-acute phase because there will be cell disruptions during this process and these regions will be filled by CSF, which may cause an increase in the conductivity. On the other hand, we have not seen any change in the hemotama region. This can also be possible, because although we expect an increase in the conductivity in the acute phase due to bleeding, in the subacute phase, on the other hand, there may be no increase in the hematoma region due to the clot formation. Our ultimate goal is to find an indication that we can differentiate the hemorrhagic and ischemic stroke in the acute phase using the proposed method but further studies need to be assessed for this purpose.

Chapter 5

CONCLUSION

Among the MR based electrical property imaging techniques MREPT has the potential that it can be used for clinical diagnosis or local specific absorption rate calculation at high field MRI systems. As mentioned in the previous chapters, the distinguishing feature of the MREPT is that the method can be applied in any standard MRI system, and no other hardware is required. Additionally, it reconstructs EPs at Larmor frequency of a MRI system and therefore it provides different pathological information about the tissue at these frequency ranges. Although MREPT attracts the researchers and clinicians due to its simplicity of application, there are several issues in the conventional MREPT methods, which prevents the clinical applicability of the method. In this dissertation, therefore, we have proposed two novel techniques to cope with these issues in the conventional MREPT methods. We have validated our methods with the simulations, experiments and case studies. The contributions of the proposed methods will be summarized with the corresponding publications as follows:

- B_1^- based multichannel cr-MREPT method has been proposed. This method shows the reduction of LCF artifact issue in the conventional cr-MREPT method by employing multi-channel receive coil configuration. Additionally, the method removes the limitation of use of birdcage coil in the

conventional MREPT methods, and enables using standard MRI coil configurations in the EP reconstruction. Furthermore, an approach to find complex B_1^- maps based on the transcieve phase assumption has been developed. The content of this study was published in the International Society for Magnetic Resonance in Medicine (ISMRM) Scientific Meetings, which are stated as below:

  - N Gurler, OF Oran, and YZ Ider, "cr-MREPT using multichannel receive coil", in ISMRM 22th Annual Meeting and Exhibition, p.3247, 2014.
  - N Gurler, OF Oran, and YZ Ider, "Combination of multichannel receive data for local cr-MREPT", in ISMRM 23th Annual Meeting and Exhibition, p.3298, 2015.

- Generalized phase based electrical conductivity imaging method has been proposed. This method solves the boundary artifact issue in the conventional phase based EPT method, and LCF artifact issue in the conventional cr-MREPT method. In the proposed method, electrical conductivity is calculated using only measured MR transcieve phase, therefore it is fast (no B_1 mapping is required), and TPA-free (applicable for any coil configuration). With these contributions, this method removes all the limitations in the conventional MREPT methods, and makes the use of MREPT possible in the clinical application. The content of this study was published in the Magnetic Resonance in Medicine and also in the International Society for Magnetic Resonance in Medicine (ISMRM) Scientific Meetings, which are stated as below:

  - N Gurler and YZ Ider, "Gradient-based electrical conductivity imaging using MR phase". Magn. Reson. Med. early view. doi:10.1002/mrm.26097, 2016.
  - N Gurler and YZ Ider, "Generalized phase based electrical conductivity imaging", in ISMRM 24th Annual Meeting and Exhibition, p.2991, 2016.

- Using the developed generalized phase based electrical conductivity imaging method, initial clinical trials have been conducted. For this purpose, two patients with neurovascular diseases in the subacute phase have been studied with the approval of Bilkent University Institutional Review Board. We have observed that the conductivity increases in the ischemic region in the subacute phase. On the other hand, we have not seen any change in the conductivity of the hematoma region but there is an increases in the edema region which is located at the periphery of the hematoma. The content of this study was published in the International Society for Magnetic Resonance in Medicine (ISMRM) Scientific Meeting, which is stated as below:

  - N Gurler, OF Oran, HD Keklikoglu, and YZ Ider, "Application of generalized phase based electrical conductivity imaging in the subacute stage of hemorrhagic and ischemic strokes". in ISMRM 24th Annual Meeting and Exhibition, p.2994, 2016.

- Last but not least, the designing of human brain model has also been performed with relation to above studies. It is generated from a volumetric segmented MRI images as a 3D model and consists of five brain tissues, i.e. grey matter, white matter, CSF, scalp, and skull. For each tissue, desired conductivity and dielectric permittivity can be assigned. The model is importable to COMSOL Multiphysics, where the EM simulation are performed in this study. The content of the development of this brain model was published in Concepts in Magnetic Resonance Part B, which is stated below:

  - N Gurler and YZ Ider, "Numerical methods and software tools for simulation, design, and resonant mode analysis of radio frequency birdcage coils used in MRI". Concepts Magn. Reson., 45: 1332. doi:10.1002/cmr.b.21279, 2015.

In conclusion, our ambition was to bring the application of MREPT one step further and to make its clinical applicability possible. The methods proposed in this dissertation especially generalized phase based electrical conductivity imaging method has a potential that it can be standardized for this purpose in the specific clinical MRI application, e.g. differentiation of ischemic and hemorrhagic strokes in the acute phase. In order to reach this situation, many case studies need to be conducted using the proposed method in a systematic way.

Bibliography

[1] E. Haacke, R. Brown, M. Thompson, and R. Venkatesan, *Magnetic Resonance Imaging: Physical Principles and Sequence Design*. Wiley, 1999.

[2] C. Gabriel, S. Gabriel, and E. Corthout, "The dielectric properties of biological tissues: I. literature survey," *Physics in Medicine and Biology*, vol. 41, no. 11, p. 2231, 1996.

[3] S. Gabriel, R. W. Lau, and C. Gabriel, "The dielectric properties of biological tissues: Ii. measurements in the frequency range 10 hz to 20 ghz," *Physics in Medicine and Biology*, vol. 41, no. 11, p. 2251, 1996.

[4] S. Gabriel, R. W. Lau, and C. Gabriel, "The dielectric properties of biological tissues: Iii. parametric models for the dielectric spectrum of tissues," *Physics in Medicine and Biology*, vol. 41, no. 11, p. 2271, 1996.

[5] R. Pethig, "Dielectric properties of body tissues," *Clinical Physics and Physiological Measurement*, vol. 8, no. 4A, p. 5, 1987.

[6] O. I. Kwon, M. Chauhan, H. J. Kim, W. C. Jeong, H. Wi, T. I. Oh, and E. J. Woo, "Fast conductivity imaging in magnetic resonance electrical impedance tomography (mreit) for rf ablation monitoring," *International Journal of Hyperthermia*, vol. 30, no. 7, pp. 447–455, 2014.

[7] E. Balidemaj, A. L. H. M. W. van Lier, H. Crezee, A. J. Nederveen, L. J. A. Stalpers, and C. A. T. van den Berg, "Feasibility of electric property tomography of pelvic tumors at 3t," *Magnetic Resonance in Medicine*, vol. 73, no. 4, pp. 1505–1513, 2015.

[8] J. M. Ernst, D. A. Litvack, D. L. Lozano, J. T. Cacioppo, and G. G. Berntson, "Impedance pneumography: Noise as signal in impedance cardiography," *Psychophysiology*, vol. 36, no. 3, pp. 333–338, 1999.

[9] R. Höber, "Eine methode, die elektrische leitfähigkeit im innern von zellen zu messen," *Pflüger's Archiv für die gesamte Physiologie des Menschen und der Tiere*, vol. 133, no. 4, pp. 237–253, 1910.

[10] H. Fricke, "The electric capacity of suspensions with special reference to blood," *The Journal of General Physiology*, vol. 9, no. 2, pp. 137–152, 1925.

[11] D. B. Kell and C. M. Harris, "On the dielectrically observable consequences of the diffusional motions of lipids and proteins in membranes," *European Biophysics Journal*, vol. 12, no. 4, pp. 181–197, 1985.

[12] S. Bone and R. Pethig, "Dielectric studies of protein hydration and hydration-induced flexibility," *Journal of Molecular Biology*, vol. 181, no. 2, pp. 323 – 326, 1985.

[13] S. Chaudhary, R. Mishra, A. Swarup, and J. Thomas, "Dielectric properties of normal and malignant human breast tissues at radiowave and microwave frequencies," *Indian Journal of Biochemistry and Biophysics*, vol. 21, no. 1, pp. 76 – 79, 1984.

[14] A. J. Surowiec, S. S. Stuchly, J. R. Barr, and A. Swarup, "Dielectric properties of breast carcinoma and the surrounding tissues," *IEEE Transactions on Biomedical Engineering*, vol. 35, pp. 257–263, April 1988.

[15] W. T. Joines, Y. Zhang, C. Li, and R. L. Jirtle, "The measured electrical properties of normal and malignant human tissues from 50 to 900 mhz," *Medical Physics*, vol. 21, no. 4, pp. 547–550, 1994.

[16] K. K. Tha, U. Katscher, S. Yamaguchi, S. Terasaka, T. Yamamoto, K. Kudo, and H. Shirato, "Electrical conductivity characteristics of glioma: Noninvasive assessment by mri and its validity," in *ISMRM 24th Annual Meeting and Exhibition*, p. 0724, May 2016.

[17] A. L. van Lier, A. G. van der Kolk, M. Brundel, J. Hendrikse, P. R. Luijten, J. J. Lagendijk, and C. A. van den Berg, "Electrical conductivity in ischemic stroke at 7.0 tesla: A case study," in *ISMRM 20th Annual Meeting and Exhibition*, p. 3484, May 2012.

[18] J. Shin, M. J. Kim, J. Lee, Y. Nam, M.-o. Kim, N. Choi, S. Kim, and D.-H. Kim, "Initial study on in vivo conductivity mapping of breast cancer using mri," *Journal of Magnetic Resonance Imaging*, vol. 42, no. 2, pp. 371–378, 2015.

[19] H. Homann, P. Brnert, H. Eggers, K. Nehrke, O. Dssel, and I. Graesslin, "Toward individualized sar models and in vivo validation," *Magnetic Resonance in Medicine*, vol. 66, no. 6, pp. 1767–1776, 2011.

[20] T. Voigt, H. Homann, U. Katscher, and O. Doessel, "Patient-individual local sar determination: In vivo measurements and numerical validation," *Magnetic Resonance in Medicine*, vol. 68, no. 4, pp. 1117–1126, 2012.

[21] D. C. Barber and B. H. Brown, "Applied potential tomography," *Journal of Physics E: Scientific Instruments*, vol. 17, no. 9, p. 723, 1984.

[22] L. F. Fuks, M. Cheney, D. Isaacson, D. G. Gisser, and J. C. Newell, "Detection and imaging of electric conductivity and permittivity at low frequency," *IEEE Transactions on Biomedical Engineering*, vol. 38, pp. 1106–1110, Nov 1991.

[23] P. M. Edic, G. J. Saulnier, J. C. Newell, and D. Isaacson, "A real-time electrical impedance tomograph," *IEEE Transactions on Biomedical Engineering*, vol. 42, pp. 849–859, Sept 1995.

[24] N. G. Gencer, Y. Z. Ider, and S. J. Williamson, "Electrical impedance tomography: induced-current imaging achieved with a multiple coil system," *IEEE Transactions on Biomedical Engineering*, vol. 43, pp. 139–149, Feb 1996.

[25] M. Cheney, D. Isaacson, and J. C. Newell, "Electrical impedance tomography," *SIAM Review*, vol. 41, no. 1, pp. 85–101, 1999.

[26] H. Griffiths, "Magnetic induction tomography," *Measurement Science and Technology*, vol. 12, no. 8, p. 1126, 2001.

[27] Y. Z. Ider and O. Birgul, "Use of the magnetic field generated by the internal distribution of injected currents for electrical impedance tomography (mr-eit)," *ELEKTRIK*, vol. 6, no. 3, pp. 215–225, 1998.

[28] Y. Z. Ider and S. Onart, "Algebraic reconstruction for 3d magnetic resonanceelectrical impedance tomography (mreit) using one component of magnetic flux density," *Physiological Measurement*, vol. 25, no. 1, p. 281, 2004.

[29] J. K. Seo, J.-R. Yoon, E. J. Woo, and O. Kwon, "Reconstruction of conductivity and current density images using only one component of magnetic field measurements," *IEEE Transactions on Biomedical Engineering*, vol. 50, pp. 1121–1124, Sept 2003.

[30] J. K. Seo, O. Kwon, and E. J. Woo, "Magnetic resonance electrical impedance tomography (mreit): conductivity and current density imaging," *Journal of Physics: Conference Series*, vol. 12, no. 1, p. 140, 2005.

[31] J. K. Seo and E. J. Woo, "Magnetic resonance electrical impedance tomography (mreit)," *SIAM Review*, vol. 53, no. 1, pp. 40–68, 2011.

[32] E. J. Woo and J. K. Seo, "Magnetic resonance electrical impedance tomography (mreit) for high-resolution conductivity imaging," *Physiological Measurement*, vol. 29, no. 10, p. R1, 2008.

[33] H. S. Nam, C. Park, and O. I. Kwon, "Non-iterative conductivity reconstruction algorithm using projected current density in mreit," *Physics in Medicine and Biology*, vol. 53, no. 23, p. 6947, 2008.

[34] G. C. Scott, M. L. G. Joy, R. L. Armstrong, and R. M. Henkelman, "Measurement of nonuniform current density by magnetic resonance," *IEEE Transactions on Medical Imaging*, vol. 10, pp. 362–374, Sep 1991.

[35] O. Kwon, E. J. Woo, J.-R. Yoon, and J. K. Seo, "Magnetic resonance electrical impedance tomography (mreit): simulation study of j-substitution algorithm," *IEEE Transactions on Biomedical Engineering*, vol. 49, pp. 160–167, Feb 2002.

[36] U. Katscher, T. Voigt, C. Findeklee, P. Vernickel, K. Nehrke, and O. Dössel, "Determination of electric conductivity and local SAR via B1 mapping.," *IEEE transactions on medical imaging*, vol. 28, no. 9, pp. 1365–1374, 2009.

[37] E. M. Haacke, L. S. Petropoulos, E. W. Nilges, and D. H. Wu, "Extraction of conductivity and permittivity using magnetic resonance imaging," *Physics in Medicine and Biology*, vol. 36, no. 6, p. 723, 1991.

[38] H. Wen, "Non-invasive quantitative mapping of conductivity and dielectric distributions using the RF wave propagation effects in high field MRI," *Medical Imaging 2003: Physics Of Medical Imaging, Pts 1 And 2*, vol. 5030, pp. 471–477, 2003.

[39] C. H. Cunningham, J. M. Pauly, and K. S. Nayak, "Saturated double-angle method for rapid b1+ mapping," *Magnetic Resonance in Medicine*, vol. 55, no. 6, pp. 1326–1333, 2006.

[40] V. L. Yarnykh, "Actual flip-angle imaging in the pulsed steady state: A method for rapid three-dimensional mapping of the transmitted radiofrequency field," *Magnetic Resonance in Medicine*, vol. 57, no. 1, pp. 192–200, 2007.

[41] L. I. Sacolick, F. Wiesinger, I. Hancu, and M. W. Vogel, "B1 mapping by bloch-siegert shift," *Magnetic Resonance in Medicine*, vol. 63, no. 5, pp. 1315–1322, 2010.

[42] T. Voigt, K. Nehrke, O. Doessel, and U. Katscher, "T1 corrected b1 mapping using multi-tr gradient echo sequences," *Magnetic Resonance in Medicine*, vol. 64, no. 3, pp. 725–733, 2010.

[43] F. S. Hafalir, O. F. Oran, N. Gurler, and Y. Z. Ider, "Convection-reaction equation based magnetic resonance electrical properties tomography (cr-mrept)," *IEEE Transactions on Medical Imaging*, vol. 33, pp. 777–793, March 2014.

[44] J. Liu, X. Zhang, S. Schmitter, P.-F. Van de Moortele, and B. He, "Gradient-based electrical properties tomography (gept): A robust method for mapping electrical properties of biological tissues in vivo using magnetic resonance imaging," *Magnetic Resonance in Medicine*, vol. 74, no. 3, pp. 634–646, 2015.

[45] X. Zhang, P.-F. V. de Moortele, S. Schmitter, and B. He, "Complex b1 mapping and electrical properties imaging of the human brain using a 16-channel transceiver coil at 7t," *Magnetic Resonance in Medicine*, vol. 69, no. 5, pp. 1285–1296, 2013.

[46] E. Balidemaj, C. A. T. van den Berg, J. Trinks, A. L. H. M. W. van Lier, A. J. Nederveen, L. J. A. Stalpers, H. Crezee, and R. F. Remis, "Csi-ept: A contrast source inversion approach for improved mri-based electric properties tomography," *IEEE Transactions on Medical Imaging*, vol. 34, pp. 1788–1796, Sept 2015.

[47] D. K. Sodickson, L. Alon, C. M. Deniz, R. Brown, B. Zhang, G. C. Wiggins, G. Y. Cho, N. B. Eliezer, D. S. Novikov, R. Lattanzi, Q. Duan, L. A. Sodickson, and Y. Zhu, "Local maxwell tomography using transmit-receive coil arrays for contact-free mapping of tissue electrical properties and determination of absolute rf phase," in *ISMRM 20th Annual Meeting and Exhibition*, p. 0387, May 2012.

[48] D. K. Sodickson, L. Alon, C. M. Deniz, N. Ben-Eliezer, M. Cloos, L. A. Sodickson, C. M. Collins, G. C. Wiggins, and D. S. Novikov, "Generalized local maxwell tomography for mapping of electrical property gradients and tensors," in *ISMRM 21th Annual Meeting and Exhibition*, p. 4175, May 2013.

[49] J. P. Marques, D. K. Sodickson, O. Ipek, C. M. Collins, and R. Gruetter, "Single acquisition electrical property mapping based on relative coil sensitivities: A proof-of-concept demonstration," *Magnetic Resonance in Medicine*, vol. 74, no. 1, pp. 185–195, 2015.

[50] T. Voigt, U. Katscher, and O. Doessel, "Quantitative conductivity and permittivity imaging of the human brain using electric properties tomography," *Magnetic Resonance in Medicine*, vol. 66, no. 2, pp. 456–466, 2011.

[51] U. Katscher, D.-H. Kim, and J. K. Seo, "Recent progress and future challenges in MR electric properties tomography.," *Computational and mathematical methods in medicine*, vol. 2013, p. 546562, 2013.

[52] A. L. van Lier, D. O. Brunner, K. P. Pruessmann, D. W. Klomp, P. R. Luijten, J. J. Lagendijk, and C. A. van den Berg, "B1+ phase mapping at 7 t and its application for in vivo electrical conductivity mapping," *Magnetic Resonance in Medicine*, vol. 67, no. 2, pp. 552–561, 2012.

[53] N. Gurler, O. F. Oran, and Y. Z. Ider, "Cr-mrept using multichannel receive coil," in *ISMRM 22th Annual Meeting and Exhibition*, p. 3247, May 2014.

[54] N. Gurler, O. F. Oran, and Y. Z. Ider, "Combination of multichannel receive data for local cr-mrept," in *ISMRM 23th Annual Meeting and Exhibition*, p. 3298, May 2015.

[55] N. Gurler and Y. Z. Ider, "Gradient-based electrical conductivity imaging using mr phase," *Magnetic Resonance in Medicine*, pp. n/a–n/a, 2016.

[56] N. Gurler and Y. Z. Ider, "Generalized phase based electrical conductivity imaging," in *ISMRM 24th Annual Meeting and Exhibition*, p. 2991, May 2016.

[57] N. Gurler, O. F. Oran, H. D. Keklikoglu, and Y. Z. Ider, "Application of generalized phase based electrical conductivity imaging in the subacute stage of hemorrhagic and ischemic strokes," in *ISMRM 24th Annual Meeting and Exhibition*, p. 2994, May 2016.

[58] D. I. Hoult, "The principle of reciprocity in signal strength calculationsa mathematical guide," *Concepts in Magnetic Resonance*, vol. 12, no. 4, pp. 173–187, 2000.

[59] A. L. H. M. W. van Lier, A. Raaijmakers, T. Voigt, J. J. W. Lagendijk, P. R. Luijten, U. Katscher, and C. A. T. van den Berg, "Electrical properties tomography in the human brain at 1.5, 3, and 7t: A comparison study," *Magnetic Resonance in Medicine*, vol. 71, no. 1, pp. 354–363, 2014.

[60] S. K. Lee, S. Bulumulla, and I. Hancu, "Theoretical investigation of random noise-limited signal-to-noise ratio in mr-based electrical properties tomography," *IEEE Transactions on Medical Imaging*, vol. 34, pp. 2220–2232, Nov 2015.

[61] C. Stehning, T. R. Voigt, and U. Katscher, "Real-time conductivity mapping using balanced ssfp and phase-based reconstruction," in *ISMRM 19th Annual Meeting and Exhibition*, p. 2994, May 2011.

[62] F. A. Fernandez and L. Kulas, "A simple finite difference approach using unstructured meshes from fem mesh generators," in *Microwaves, Radar and Wireless Communications, 2004. MIKON-2004. 15th International Conference on*, vol. 2, pp. 585–588 Vol.2, May 2004.

[63] A. Savitzky and M. J. E. Golay, "Smoothing and differentiation of data by simplified least squares procedures.," *Analytical Chemistry*, vol. 36, no. 8, pp. 1627–1639, 1964.

[64] K. Nehrke and P. Brnert, "Dreama novel approach for robust, ultrafast, multislice b1 mapping," *Magnetic Resonance in Medicine*, vol. 68, no. 5, pp. 1517–1526, 2012.

[65] V. John and P. Knobloch, "On spurious oscillations at layers diminishing (sold) methods for convectiondiffusion equations: Part i a review," *Computer Methods in Applied Mechanics and Engineering*, vol. 196, no. 1720, pp. 2197 – 2215, 2007.

[66] V. John and P. Knobloch, "On spurious oscillations at layers diminishing (sold) methods for convectiondiffusion equations: Part {II} analysis for and finite elements," *Computer Methods in Applied Mechanics and Engineering*, vol. 197, no. 2124, pp. 1997 – 2014, 2008.

[67] N. Gurler and Y. Z. Ider, "Numerical methods and software tools for simulation, design, and resonant mode analysis of radio frequency birdcage coils used in mri," *Concepts in Magnetic Resonance Part B: Magnetic Resonance Engineering*, vol. 45, no. 1, pp. 13–32, 2015.

[68] BrainWeb, "Simulated Brain Database." `http://brainweb.bic.mni.mcgill.ca/brainweb/`.

[69] B. Aubert-Broche, A. C. Evans, and L. Collins, "A new improved version of the realistic digital brain phantom," *NeuroImage*, vol. 32, no. 1, pp. 138 – 145, 2006.

[70] Q. Fang and D. A. Boas, "Tetrahedral mesh generation from volumetric binary and grayscale images," in *2009 IEEE International Symposium on Biomedical Imaging: From Nano to Macro*, pp. 1142–1145, June 2009.

[71] G. Scott, M. Joy, R. Armstrong, and R. Henkelman, "Sensitivity of magnetic-resonance current-density imaging," *Journal of Magnetic Resonance (1969)*, vol. 97, no. 2, pp. 235 – 254, 1992.

[72] H. Gudbjartsson and S. Patz, "The rician distribution of noisy mri data," *Magnetic Resonance in Medicine*, vol. 34, no. 6, pp. 910–914, 1995.

[73] A. Stogryn, "Equations for calculating the dielectric constant of saline water (correspondence)," *IEEE Transactions on Microwave Theory and Techniques*, vol. 19, pp. 733–736, Aug 1971.

[74] K. Iizuka, "An agar-agar chamber for study of electromagnetic waves in an inhomogeneous medium," *IEEE Transactions on Antennas and Propagation*, vol. 19, pp. 365–377, May 1971.

[75] K. U, A. H, I. MK, D. K, K. P, and N. G, "Towards the investigation of breast tumor malignancy via electric conductivity measurement," in *ISMRM 21st Annual Meeting and Exhibition*, p. 3372, May 2013.

[76] O. Dietrich, J. G. Raya, S. B. Reeder, M. F. Reiser, and S. O. Schoenberg, "Measurement of signal-to-noise ratios in mr images: Influence of multichannel coils, parallel imaging, and reconstruction filters," *Journal of Magnetic Resonance Imaging*, vol. 26, no. 2, pp. 375–385, 2007.

[77] N. K. Bangerter, B. A. Hargreaves, S. S. Vasanawala, J. M. Pauly, G. E. Gold, and D. G. Nishimura, "Analysis of multiple-acquisition ssfp," *Magnetic Resonance in Medicine*, vol. 51, no. 5, pp. 1038–1047, 2004.

[78] K. U, van Lier AL, van den Berg C, and K. J, "Rf shimming improves phase-based conductivity imaging," in *ISMRM 20th Annual Meeting and Exhibition*, p. 3487, May 2012.

[79] E. M. Haacke, Y. Xu, Y.-C. N. Cheng, and J. R. Reichenbach, "Susceptibility weighted imaging (swi)," *Magnetic Resonance in Medicine*, vol. 52, no. 3, pp. 612–618, 2004.

Appendix A

Derivation of the Central Equation

Writing the imaginary terms in Eq. 4.10 gives

$$\begin{aligned}&\left(\begin{bmatrix}\frac{\partial}{\partial x}\phi^{tr}\\ \frac{\partial}{\partial y}\phi^{tr}\\ \frac{\partial}{\partial z}\phi^{tr}\end{bmatrix}\cdot\begin{bmatrix}\frac{\partial Re\{ln(\gamma)\}}{\partial x}\\ \frac{\partial Re\{ln(\gamma)\}}{\partial y}\\ \frac{\partial Re\{ln(\gamma)\}}{\partial z}\end{bmatrix}\right)+\\ &\left(\begin{bmatrix}\frac{\partial}{\partial y}\left(\phi^{+}-\phi^{-}\right)\\ -\frac{\partial}{\partial x}\left(\phi^{+}-\phi^{-}\right)\\ 0\end{bmatrix}\cdot\begin{bmatrix}\frac{\partial Im\{ln(\gamma)\}}{\partial x}\\ \frac{\partial Im\{ln(\gamma)\}}{\partial y}\\ \frac{\partial Im\{ln(\gamma)\}}{\partial z}\end{bmatrix}\right)-\nabla^{2}\phi^{tr}+2\mu_{0}\sigma=0\end{aligned}\tag{A.1}$$

It has been observed in the simulations (including the human head simulations) that the derivatives of phase difference ($\phi^{+}-\phi^{-}$) are negligibly small compared to the derivatives of transcieve phase (ϕ^{tr}) in the transition regions. For the other regions, which have uniform EPs distributions, these terms are not important because $\nabla ln(\gamma)=0$. Furthermore, the first two terms in Eq. A.1 have been compared, and it has been found that

$\left(\begin{bmatrix} \frac{\partial}{\partial y}\left(\phi^{+}-\phi^{-}\right) \\ -\frac{\partial}{\partial x}\left(\phi^{+}-\phi^{-}\right) \\ 0 \end{bmatrix} \cdot \begin{bmatrix} \frac{\partial Im\{ln(\gamma)\}}{\partial x} \\ \frac{\partial Im\{ln(\gamma)\}}{\partial y} \\ \frac{\partial Im\{ln(\gamma)\}}{\partial z} \end{bmatrix} \right)$ is at least one order of magnitude smaller compared to the term, $\left(\begin{bmatrix} \frac{\partial}{\partial x}\phi^{tr} \\ \frac{\partial}{\partial y}\phi^{tr} \\ \frac{\partial}{\partial z}\phi^{tr} \end{bmatrix} \cdot \begin{bmatrix} \frac{\partial Re\{ln(\gamma)\}}{\partial x} \\ \frac{\partial Re\{ln(\gamma)\}}{\partial y} \\ \frac{\partial Re\{ln(\gamma)\}}{\partial z} \end{bmatrix} \right)$. Neglecting the second term and rewriting Eq. A.1 gives:

$$\begin{bmatrix} \frac{\partial}{\partial x}\phi^{tr} \\ \frac{\partial}{\partial y}\phi^{tr} \\ \frac{\partial}{\partial z}\phi^{tr} \end{bmatrix} \cdot \begin{bmatrix} \frac{\partial Re\{ln(\gamma)\}}{\partial x} \\ \frac{\partial Re\{ln(\gamma)\}}{\partial y} \\ \frac{\partial Re\{ln(\gamma)\}}{\partial y} \end{bmatrix} -\nabla^{2}\phi^{tr}+2\omega\mu_{0}\sigma= 0 \tag{A.2}$$

where

$$Re\left\{ln\left(\gamma\right)\right\} = ln\left(\sqrt{\sigma^{2}+\left(\omega\epsilon\right)^{2}}\right)$$

For $\sigma^{2} >> (\omega\epsilon)^{2}$, the real part of $ln(\gamma)$ could be approximated as $Re\left\{ln\left(\gamma\right)\right\} \approx ln(\sigma)$. Defining $\rho = \frac{1}{\sigma}$ (resistivity) and using the $\nabla ln(\sigma) = -\frac{1}{\rho}\nabla\rho$, Eq. A.2 can be written as follows

$$\left(\nabla\phi^{tr}\cdot\nabla\rho\right)+\nabla^{2}\phi^{tr}\rho-2\omega\mu_{0}= 0 \tag{A.3}$$

which is the central equation of the generalized phase based electrical conductivity imaging approach.